LBNL-51907

ERNEST ORLANDO LAWRENCE BERKELEY NATIONAL LABORATORY

The Reaction and Solvation Dynamics of Organometallic Compounds

Preston T. Snee

Chemical Sciences Division

December 2002

Ph.D. Thesis

REFERENCE COPY
Does Not
Circulate
Library Annex Reference
Lawrence Berkeley National Laboratory

LBNL-51907
Copy 1

DISCLAIMER

This document was prepared as an account of work sponsored by the United States Government. While this document is believed to contain correct information, neither the United States Government nor any agency thereof, nor the Regents of the University of California, nor any of their employees, makes any warranty, express or implied, or assumes any legal responsibility for the accuracy, completeness, or usefulness of any information, apparatus, product, or process disclosed, or represents that its use would not infringe privately owned rights. Reference herein to any specific commercial product, process, or service by its trade name, trademark, manufacturer, or otherwise, does not necessarily constitute or imply its endorsement, recommendation, or favoring by the United States Government or any agency thereof, or the Regents of the University of California. The views and opinions of authors expressed herein do not necessarily state or reflect those of the United States Government or any agency thereof or the Regents of the University of California.

LBNL-51907

The Reaction and Solvation Dynamics of Organometallic Compounds

Preston Todd Snee
Ph.D. Thesis

Department of Chemistry
University of California, Berkeley

and

Chemical Sciences Division
Ernest Orlando Lawrence Berkeley National Laboratory
University of California
Berkeley, CA 94720

December 2002

This work was supported by the Director, Office of Science, Office of Basic Energy Sciences, Chemical Sciences Division, of the U.S. Department of Energy under Contract No. DE-AC03-76SF00098.

The Reaction and Solvation Dynamics of Organometallic Compounds.

By

Preston Todd Snee

B. S. (University of North Carolina, Chapel Hill) 1995

A dissertation submitted in partial satisfaction of the

requirements for the degree of

Doctor of Philosophy

in

Chemistry

in the

GRADUATE DIVISION

of the

UNIVERSITY OF CALIFORNIA, BERKELEY

Committee in charge:

Professor Charles B. Harris, Chair

Professor Roger Falcone

Professor Martin Head–Gordon

Fall 2002

The Reaction and Solvation Dynamics of Organometallic Compounds

Copyright © 2002

by

Preston Todd Snee

The U.S. Department of Energy has the right to use this document
for any purpose whatsoever including the right to reproduce
all or any part thereof.

Abstract

The Reaction and Solvation Dynamics of Organometallic Compounds.

by

Preston Todd Snee

Doctor of Philosophy in Chemistry

University of California, Berkeley

Professor Charles B. Harris, Chair

Ultrafast laser spectroscopy provides a tool by which a chemical reaction may be monitored from the initiation to the formation of the final products. This method allows for the unambiguous determination of the identity of reactive intermediates which may not be observed in traditional mechanistic studies. The barriers and reaction mechanism may also be determined from the kinetic data. Unfortunately, the transient nature of the intermediates observed in ultrafast experiments have lifetimes which are too short for traditional characterization. In these cases, electronic structure theory and molecular dynamics methods may be utilized to study these species.

The findings presented in this thesis are based upon experimental and theoretical results on the reaction and solvation dynamics of transient intermediate species which are important in a variety of organometallic chemical systems. First, the mechanism of several bond activation reactions have been examined using femtosecond UV pump / IR

probe spectroscopy. A special emphasis has been placed on the effect that the organometallic intermediate spin state has on the reaction mechanism. It has been found that triplet species do not coordinate strongly with alkanes or the alkyl group of reactive solvents, which leads to increased reaction rates compared to those observed with similar singlet intermediates. The factors that govern the reactivity of high spin species have also been elucidated. These results are supported by ab initio and Density Functional Theory (DFT) calculations, which qualitatively reproduce and explain the trends in the observed experimental results.

In order to examine the microscopic aspects of solvent / solute interactions, classical as well as mixed quantum classical molecular dynamics simulation programs have been developed. These methods have been used to study the solvation dynamics of organometallic charge transfer complexes as well as excess electrons in frozen glasses, gas clusters and at surface interfaces. These results have shown that excited states of organometallic chromophores which have localized charge densities are preferentially solvated in polar solvents. The study of the dynamics of the excess electron have shown that the solvation dynamics depend on the periodicity of the bath. Using the method of Transition Path Sampling, a general mechanism of ligand rearrangement has been proposed. Overall, these results complement existing experimental results and provide a more detailed picture of solvent / solute interactions that may not be determined from experimental studies.

To my mother and father:

Diane Elizabeth Preston and Thomas Joseph Snee, Sr.

Table of Contents

List of Figures v

List of Tables viii

Acknowledgment x

1. Introduction 1

    1.1 Background 1

    1.2 Experimental Methods 4

    1.3 Theoretical Methods 6

Part I: Molecular Solvation and Bond Activation by Coordinatively Unsaturated Organometallic Intermediates

2. The Fundamentals of Solution Phase Reaction Dynamics: Vibrational Relaxation, Recombination, Barrier Crossing and Rearrangement 9

    2.1 Vibrational Relaxation, Geminate Recombination and Barrier Crossing in One–Electron Oxidative Addition Reactions 10

    2.2 Intermolecular and Intramolecular Rearrangement 18

    2.3 Conclusions 20

3. The Role of High Spin Intermediates in Si–H Activation 22

    3.1 Introduction 22

    3.2 Experimental Results 24

    3.3 The Dynamics of High Spin Intermediates 28

    3.4 DFT and ab initio Calculation Results 31

3.5 Conclusion 35

4. High Spin Dynamics of $Fe(CO)_4$ and CpCo(CO) 37

4.1 Introduction 38

4.2 Experimental Results 39

4.3 Discussion 45

4.4 Quantum Chemical Modeling 50

4.5 Concusion 61

5. The Photochemical Reaction Dynamics of $Fe(CO)_5$ 63

5.1 Introduction 63

5.2 Experimental Results 64

5.3 Discussion 69

5.4 Quantum Chemical Modeling 72

5.5 Conclusion 80

6. Ultrafast UV Pump/IR Probe Studies of C–H Activation In Linear, Cyclic and Aryl Hydrocarbons 81

6.1 Introduction 81

6.2 Experimental Results 83

6.3 Discussion 89

6.4 Conclusion 96

Part II: Theoretical Studies of Solvation Dynamics

7. The Solvation Dynamics of Excited States of $[Ru(bpy)_3]^{2+}$ Studied by Computer Simulation 98

7.1 Introduction 98

7.2 Methods and Results 100

7.3 Discussion 112

7.4 Conclusion 119

8. Mixed Quantum / Classical Dynamics Simulations of Excess Electrons in Low Temperature Matrices, in Gas Clusters and at a Surface Interface 121

8.1 Introduction 122

8.3 The Split Operator Method 124

8.4 Simulation Details 127

8.5 Results 132

8.6 Discussion 144

8.7 Conclusion 149

9. Transition Path Sampling of Rearrangement Reactions 150

9.1 Introduction 150

9.2 Transition Path Sampling 153

9.3 Results and Discussion 155

9.4 Conclusions 160

References 161

Appendix 175

List of Figures

Figure 1.1 The 30 Hz femtosecond laser system..... 2

Figure 2.1 The time resolved spectra and kinetics of $Re_2(CO)_{10}$..... 11

Figure 2.2 The vibrational relaxation of $CpW(CO)_3$ and $CpRh(CO)_2$..... 13

Figure 2.3 The transient difference spectra of $[CpW(CO)_3]_2$ 15

Figure 2.4 The transient difference spectra of $[CpW(CO)_3]_2$ in CCl_4..... 16

Figure 3.1 The ultrafast spectra and kinetics of $CpV(CO)_4$ in heptane solution..... 25

Figure 3.2 The ultrafast spectra and kinetics of $CpV(CO)_4$ in triethylsilane..... 27

Figure 3.3 The DFT structures of species observed in the $CpV(CO)_4$ study..... 32

Figure 4.1 The spectra of $CpCo(CO)_2$ and $Fe(CO)_5$ in heptane..... 40

Figure 4.2 The spectra and kinetics of $CpCo(CO)_2$ in triethylsilane..... 41

Figure 4.3 The spectra and kinetics of $CpRh(CO)_2$ in triethylsilane..... 43

Figure 4.4 The spectra and kinetics of $Fe(CO)_5$ in triethylsilane..... 44

Figure 4.5 The DFT geometries of species observed in the $CpCo(CO)_2$ study..... 51

Figure 4.6 The DFT geometries of species observed in the $Fe(CO)_5$ study..... 52

Figure 4.7 The metal–Si potential energy surfaces for singlet and triplet organometallic species with SiH_3CH_3..... 59

Figure 5.1 The ultrafast spectra of $Fe(CO)_5$ in tert–butyl alcohol..... 65

Figure 5.2 The ultrafast kinetics of $Fe(CO)_4$ in various alcohol solutions..... 66

Figure 5.3 The spectra and kinetics of $Fe(CO)_5$ in triethylphosphine solution..... 68

Figure 5.4 The DFT optimized geometries of several of the species observed in the $Fe(CO)_5$ study..... 73

Figure 5.5 The potential energy surfaces of singlet and triplet $Fe(CO)_4$ with various ligands 75

Figure 6.1 Transient kinetics of η^3–Tp*Rh(CO)(H)(R) in alkanes 84

Figure 6.2 Transient difference spectra of η^3–Tp*$Rh(CO)_2$ in benzene 85

Figure 6.3 Nanosecond difference spectra of η^3–Tp*$Rh(CO)_2$ in benzene 86

Figure 6.4 Ultrafast kinetics of η^2–Tp*Rh(CO)(solvent) and η^3–Tp*Rh(CO)(H)(R) in d_6–benzene 87

Figure 6.5 Transient difference spectrum of η^2–Bp*$Rh(CO)_2$ in d_6–benzene 88

Figure 6.6 Transient difference spectra of $CpRh(CO)_2$ in alkanes 89

Figure 6.7 Geometries of η^2–Tp*Rh(CO)(CH_4) and η^2–Tp*Rh(CO)(C_6H_6) 90

Figure 7.1 The equilibrium solvent response for the ground state and excited state models of $[Ru(bpy)_3]^{2+}$ 101

Figure 7.2 The equilibrium solvent response for the ground state with and without a single PF_6^- counterion 102

Figure 7.3 The Hartree–Fock geometry of $[Ru(bpy)_3]^{2+}$ at the ground state 104

Figure 7.4 The calculated and observed UV/Vis spectra of $[Ru(bpy)_3]^{2+}$ 107

Figure 8.1 The potential energy surfaces and optimal structures of methanol at various positions on a platinum cluster 131

Figure 8.2 The radial distribution functions of room temperature methanol with the solvated electron 134

Figure 8.3 The solvation dynamics of an excess electron in room temperature methanol 135

Figure 8.4 The RDF of low temperature methanol with the solvated electron 136

Figure 8.5 The solvation dynamics of an excess electron in low temperature glassy methanol 137

Figure 8.6 Various properties of the electron and bath in the low temperature charge injection simulations 137

Figure 8.7 The radial distribution functions and z–dependent distributions of methanol with the solvated interfacial electron 139

Figure 8.8 The equilibrium solvation dynamics of an excess interfacial electron in low temperature methanol bath 140

Figure 8.9 The probability distribution of an excess interfacial electron in a methanol bath 140

Figure 8.10 The radial distribution functions of frozen gas phase methanol cluster with the solvated electron 141

Figure 8.11 The equilibrium and non–equilibrium solvation dynamics of an excess electron in low temperature methanol gas cluster 142

Figure 8.12 Various properties of the electron and methanol gas cluster in the low temperature charge injection simulations 142

Figure 9.1 The optimized structure of $CrCO_5$ and methanol 151

Figure 9.2 The radial distribution functions for methanol and $Cr(CO)_5$. Inset shows the O – Cr distribution for the first and second solvent shells 153

Figure 9.3 The Cr–O distance for the nearest and next nearest methanol solvent molecules 156

Figure 9.4 The flow of energy in the ligand exchange reaction 159

List of Tables

Table 4.1 The optimized geometric parameters for the iron and cobalt organometallic systems 54

Table 4.2 The binding strengths of various organometallic fragment species with CO, C_2H_3 and SiH_3CH_3 model ligands 56

Table 4.3 The energetic splitting between singlet and triplet states at various levels of theory 57

Table 4.4 Summary of the observed vibrational frequencies, DFT result, and literature references 58

Table 4.5 The results of the DFT potential energy curve calculations 60

Table 5.1 The timescales of formation of the OH–solvated singlet intermediate for the photochemical reaction of $Fe(CO)_5$ and $Cr(CO)_6$ in various alcohols 67

Table 5.2 The binding strengths of various organometallic species with CO, MeOH, and $P(CH_3)_3$ 77

Table 5.3 The energetic splitting between singlet and triplet states at various levels of theory 77

Table 5.4 The results of the DFT potential energy curve calculations 79

Table 7.1 The Lennard–Jones and partial charges of the acetonitrile solvent and $[Ru(bpy)_3]^{2+}$ solute 101

Table 7.2 The optimized geometric parameters of the ground and lowest singlet and triplet excited states of $[Ru(bpy)_3]^{2+}$ 105

Table 7.3 The UV/VIS spectra of $[Ru(bpy)_3]^{2+}$ at the ground state geometry 106

Table 7.4 The spin allowed spectra of the first degenerate excited singlet and triplet states at their individual optimized geometries..... 106

Table 7.5 The solvation free energy differences between various excited states at their Frank–Condon and optimized geometries..... 109

Table 8.1 The simulation parameters used for the solvent and solvent / electron potential..... 128

Table 8.2 The Pt(100) / methanol potential parameters..... 132

Table 8.3 The average properties of the solvated electron in the various simulations reported..... 143

Table 9.1 The Lennard–Jones and electrostatic simulation parameters used for the methanol solvent and $Cr(CO)_5$ solute..... 151

Table 9.2 The Morse parameters for the $Cr(CO)_5$ / methanol potential..... 152

Acknowledgment

I am indebted to many people during my stay at the Department of Chemistry at U. C. Berkeley. First, I would like to thank Professor Charles B. Harris for providing the environment in which these studies were conducted as well as showing me how a university research group is managed. Also, our administrative assistant Vijaya Narasimhan has kept the group research on track with her crafty knowledge of the day to day runnings of the business office. I am especially indebted to my undergraduate advisor, Prof. Edward T. Samulski at the University of North Carolina. Prof. Samulski showed me that I shouldn't be afraid of seemingly impossible tasks and the role that an advisor has in the education of undergraduate and graduate students.

The senior members of the group, including Steve Bromberg, Matt Asplund, Nien–hue Ge, Jason McNeill, Ken Kotz and Haw Yang helped me to understand various practical aspects of experimental science as well as the 'ins and outs' of life in the Department. I would especially like to thank Prof. Haw Yang, whom was my primary mentor during my first two years at Berkeley. Haw taught me how to run experiments, administrate a computer network, and the theoretical techniques that I would rely upon during my years in graduate school. One year after my arrival at Berkeley Christine K. Payne joined the project, whom has been my primary collaborator in all the experimental work presented in this thesis. Sheryl D. Mebane joined for a brief period during which she was able to assist me with some synthetic chemistry which was instrumental for the work presented in Chapter 5. Later Libby Garrard, Jennifer Shanoski and Jason Van Zanten joined, and with their arrival I can leave knowing that the project will be in good hands. The other members of the group include Simon Liu, Andre Miller, Paul

Szymanski, Abbas Rizvi, Nicole Winter, Ilya Bezel, Matt Strader, Aram Yang and Sean Garrett–Roe have been especially helpful. I also appreciate Sean's efforts at keeping me honest in our work simulating solvated electrons, the results of which are presented in Chapter 8.

Outside of the lab I have many more people to thank for helping me understand subjects other than the field of ultrafast photochemistry. I would like to thank Harry Gomez, Jason Robinson, Nick Pivonka and Aaron Mann for showing me how vacuum technology works as well as explaining to me the issues important in gas phase spectroscopy. I will especially remember Harry Gomez's skill with a hand drill and the assorted items that Jason and I found inside of a diffusion pump. Bob Havlin and Tanya Mazur have educated me about the finer details of solid state NMR spectroscopy as well as provided a backyard for our kiddie pool. I would also like to thank Bob Havlin, Tanya Mazur, Richard and Christina Schaller, Harry Gomez and Glenda Donato for our many trips to Las Vegas and Tahoe. Keith McCrea, Jenny and Seth Bush, Alexandra Hoops, Richard Wong and Kolya Paech will also have a special place in my memories, depending on the events of the evening. I would also like to thank my family for support while I have been away in the wilds of northern California.

The work included in this dissertation could not have been possible without the financial support of the National Science Foundation and specialized equipment supported by the U. S. Department of Energy.

Chapter 1

Introduction and Methods

The majority of chemistry that is important to human endeavors occurs in the condensed phase. As such, elucidating the nature of solvent / solute interactions is essential to understand the role of the solvent in the outcome of a chemical reaction. The subject of this thesis is to develop a clear picture of how solvent dynamics influence reactions such as photochemical C–H and Si–H bond activation by coodinatively unsaturated organometallic species. In addition to the study of these bond activation reactions, simulations of the solvation dynamics of various systems has also been performed. The methods employed in this research include both experimental and theoretical techniques, the methods of which are summarized in this chapter.

Section 1.1 Background

Organometallic chemistry is a very diverse field that contains many examples of the fundamental processes that are of interest in the chemical sciences. Due to the ability of transition metals to exist in multiple oxidation states, metal containing complexes may undergo oxidative addition reactions in which new ligands are added to the coordination sphere at the metal center. Examples of oxidative addition reactions include photochemical C–H, Si–H, and C–Cl bond activation. Early work in our group has shown that the dynamics of these bond activation reactions may be studied using femtosecond UV pump / IR probe spectroscopy.[1–3] The UV pump pulse is used to generate a reactive coordinatively unsaturated metal intermediate, the dynamics of which are monitored in the IR. The metal complexes are chosen so that they contain at least one carbonyl (CO) ligand, which serves as a probe chromophore. Due to the metal to

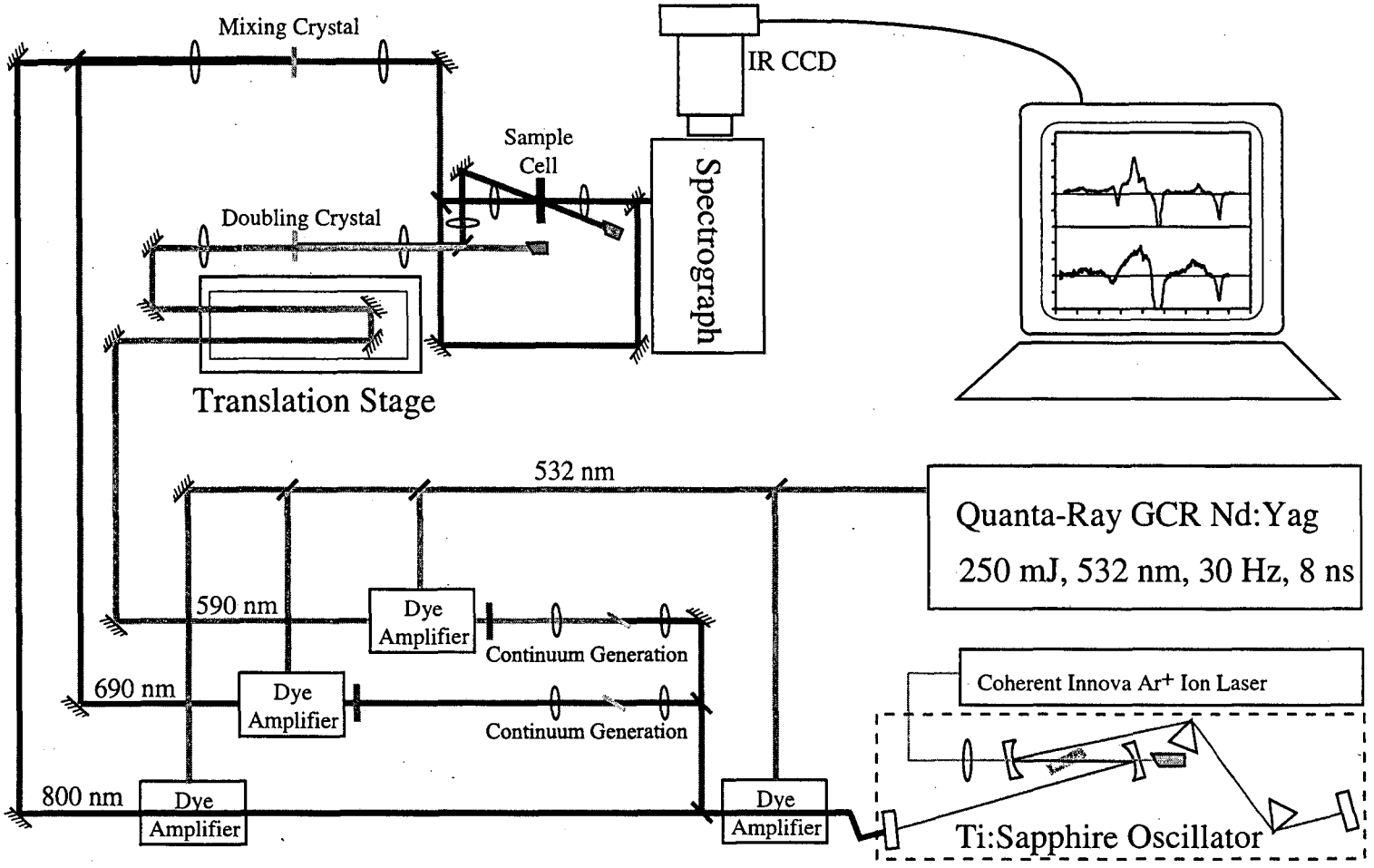

Figure 1.1. The 30 Hz femtosecond UV pump IR probe laser system.

CO back donation, the loss (gain) of electron density of the metal results in blue (red) shifting of the observed CO stretch frequency. Consequently, the dynamics at the metal center may be elucidated by monitoring the IR spectral region of a CO chromophore.

Early work in our group has shown that solvent dynamics plays an important role in the mechanism of bond activation reactions. Upon the photochemical formation of a coordinatively unsaturated organometallic intermediate, a solvent molecule may occupy the empty coordination site at the metal center becoming what has been described as a "token ligand".[4] In the case of long chain alcohols or silane solvents, the unsaturated species may be solvated by the alkyl group or form the product by binding to the strongly interacting O–H or Si–H bond. The weakly bound alkyl solvated species must rearrange to form the product on a much longer timescale, which has been shown to occur via a dissociative, stochastic mechanism.

In the study of Si–H activation in triethylsilane, it was found that the spin state of the metal affects the interaction with the solvent. The spin dependent solute / solvent interactions was first observed in an earlier study of Si–H bond activation by $CpMn(CO)_3$, which forms coordinatively unsaturated singlet $^1CpMn(CO)_2$ and triplet $^3CpMn(CO)_2$ intermediates upon UV photolysis.[3] The high spin species was observed to react as a faster rate with the Si–H bond due to the lack of strong interactions with the alkyl group of the triethylsilane solvent. However, the strong interactions of the low spin $^1CpMn(CO)_2$ with the ethyl moiety of triethylsilane hinders the reactivity with the Si–H bond. In the case of C–Cl activation by radical organometallic intermediates, the lack of strong solvent / solute interaction leads to the observation of a variety of phenomena such as secondary geminate recombination and intramolecular isomerization.[3,5] In order to extend these studies, bond activation has been examined

in systems in which the solute / solvent interaction is weak due to the high spin state of the transient intermediate. The experimental results are augmented with quantum chemical calculations which qualitatively reproduce the trends in the experimental data. The results have shown that the rate at which high spin species react is determined by the coupling of the spin states and the classical potential energy barriers.

While these studies have revealed the importance of solvent dynamics in a variety of chemical processes, solvent / solute interactions are best studied using molecular dynamics (MD) simulation methods. These theoretical techniques provide a unique way to evaluate the specific molecular interactions between a solute and a solvent as well as the time dependence of these interactions. These methods have been applied to a variety of chemical systems important to electron transfer processes, such as the solvation dynamics of the excited states of $[Ru(bpy)_3]^{2+}$ and the excess electron. These results have qualitatively reproduced the trends seen in the experimental results and provide more detailed information as to the nature of solvent interaction with systems of localized and delocalized charge distributions. A general mechanism of intramolecular rearrangement has also been addressed in Transition Path Sampling simulations.

Section 1.2 Experimental Methods

The technique used in our experimental chemical bond activation research is femtosecond UV pump IR probe spectroscopy. A diagram of this system is provided in Figure 1.1. At the heart of the instrument is a home build Ti–Sapphire oscillator pumped by all lines of a Coherent Innova Ar^+ ion laser. This system is capable of producing ~100 fs pulses centered at 800 nm. The 80 MHz pulse train is then amplified in a series of Bethune dye cell amplifiers which are pumped by the doubled output of a 30Hz Quanta Ray GCR–4 Nd(YAG) laser.[6] The initial output of the oscillator is

amplified in two dye cells and is then compressed in a prism–pair. This amplified light is then split into three beams. One beam is amplified at 800 nm through a single cell. The remaining two beams are focused into sapphire windows to generate while light continuum. The output of the while light continuum generator is amplified by a single dye cell amplifier and is then passed through a 10 nm band gap filter for spectral selectivity. One beam is selected for 690 nm in order to generate IR and the other for 590 nm or 650 nm in order to generate the pump beam. Both laser pulses are then further amplifier in two more dye cell amplifier cells, although the pump beam is prism–pair compressed before amplification in the last cell.

The IR probe pulse centered around 2000 cm^{-1} is generated by difference frequency mixing the 800 and 690 nm light in a $LiIO_3$ crystal. The IR probe is then split into a signal and reference in order to calculate the absorption spectrum. The UV pump pulse is produced by doubling the 590 or 650 nm beam and is delayed electronically on a Klinger variable translation stage. The pump and probe beams are spatially overlapped using an iris inside of our sample cell. The detector consists of an engineer grade MCT 256×256 array detector which is coupled to a spectrograph, allowing for the detection of a ~70 cm^{-1} spectrum per laser pulse. The time resolution of this system as determined by cross correlation in a silicon wafer and is typically ~300 fs. A diagram of this system is presented in Fig. 1.1. Unfortunately, the renovation of the laboratories in Hildebrand Hall forced the removal of this system in September 2000, which has been replaced with a solid–state amplifier based UV pump / IR probe laser apparatus built largely on the efforts of Christine Payne.

Over the past four years our group has developed synthetic chemistry capabilities. Several of the studies presented in the present work were performed on

compounds which are not commercially available. The addition of a glove box and the development of a synthetic laboratory was vital for performing synthesis of highly reactive organometallic compounds and preparing air sensitive samples for analysis. Typically, samples were continuously pumped through an airtight Harrick observation cell throughout the photochemical experiment. Sample concentrations are usually on the order of ~10 mM for which for most compounds corresponded to an UV absorption of 1 OD.

Section 1.3 Theoretical Methods

In the course of our research it became apparent that a method was needed to characterize the transient intermediates observed in our studies, as these species have intrinsic lifetimes that prevent conventional characterization. In this vein, our group turned to ab initio and Density Functional Theory (DFT) methods in order to calculate the electronic structure (and thus many of the physical properties) of these intermediates. For the most part, the Jaguar program was used for DFT calculations,[7] and the GAMESS or Gaussian '98 packages were used to obtain ab inito results.[8,9] During our work the general observation has been made that DFT results are often much more accurate that Hartree–Fock or MP2 ab initio calculations for transient coordinatively unsaturated organometallic intermediates. The DFT calculations are often in agreement with high level ab initio CASSCF and pt2–CASSCF results as well. Combined with 4 Intel Pentium dual processor based PCs running Linux, the theoretical capability of our laboratory is enough to tackle very large systems of interest. The supercomputer facilities at the Lawrence Berkeley National Laboratory have been utilized as well.

In general, our group has developed a methodology which has proven to be effective in order to understand some of the trends observed in our data. As many of our

systems of interest are inorganic or organometallic compounds, the geometries are optimized using DFT with the B3LYP functional.[10,11] These geometries were used for all subsequent DFT or ab initio analysis. Unfortunately, coordinatively unsaturated organometallic intermediates often have nearby high spin states which are almost degenerate with the one of interest, which makes low level Hartree–Fock and MP2 analysis unreliable. In those cases pt2–CASSCF calculations were performed using the GAMESS package, using a d–orbital based active space. Details of the pt2–CASSCF calculations are provided in Chapter 3 in Sec. 3.4. The counterpoise method is used to calculate binding energies without the use of a geometry relaxation correction. As MP2 likely overbinds molecular species of interest, binding energy calculations are best done using DFT.

In order to describe the minute details of solvent dynamics which may not be resolved using our experimental techniques, molecular dynamics simulation programs have been developed. Molecular Dynamics is based on integration of classical Newtonian equations of motion for an ensemble of solvent / solute molecules using an empirically derived potential energy surface.[12] The potential energy surface is typically derived from a Lennard–Jones and Coulombic pair potential. The advantage of the reduction of the number of degrees of freedom and quantum mechanical effects allows for tractable simulations to be performed on solvent / solute systems. Quantum effects may be incorporated to a limited extent through mixed quantum / classical simulations. The results based upon these simulations are presented of Part II of this thesis.

Part I: Molecular Solvation and Bond Activation by Coordinatively Unsaturated Organometallic Intermediates

Solvation dynamics has been the subject of intense study in the chemical sciences. While it is typical to view the solvent as an electrostatic continuum which perturbs the solute molecule, the meaning of solvation changes drastically for a coordinatively unsaturated organometallic species. A coordinatively unsaturated intermediate has an open binding site at the metal center that a solvent molecule may occupy. In these circumstances, the solvent is best viewed as a molecular species that has specific interactions with the solute molecule.

In the course of our bond activation studies, our group has developed a comprehensive understanding of solvent interactions with a coordinatively unsaturated metal center. Part I of this thesis reviews the experimental work and conclusions of our group over the past several years concerning such issues as molecular solvation of singlet and triplet intermediates, token ligand rearrangement and barrier crossing in bond activation reactions. The influence of geminate recombination and vibrational relaxation are also discussed. Part II explores our theoretical work on solvation dynamics of coordinatively saturated species such as $[Ru(bpy_3)]^{2+}$ and the excess electron. These studies test linear response theory and explore the solvent response in systems with low dimensional periodicity. The sum total of the work in this thesis provides a through picture of both molecular and collective solvation dynamics.

Chapter 2

The Fundamentals of Solution Phase Reaction Dynamics: Vibrational Relaxation, Recombination, Barrier Crossing and Rearrangement

There are several fundamental photochemical events that govern the outcome of a chemical reaction in solution. These include vibrational relaxation, geminate recombination, non–equilibrium barrier crossing, and intermolecular and intramolecular rearrangement. Over the past four years, our group has examined several of these phenomena in the progress of our bond activation research. These studies have clarified many of the aspects of ultrafast chemical dynamics from the initiation of the reaction to the termination and will be summarized below.

This chapter is outlined as follows. In sec 2.1, the importance of vibrational relaxation, geminate recombination, and non–equilibrium barrier crossing are discussed using data from our previous study of C–Cl bond activation by the transient radical species $Re(CO)_5$ and $CpW(CO)_3$. In sec. 2.2, the results of our studies on the mechanism of Si–H and C–H activation by low spin transient organometallic intermediates are given. These results exemplify the importance of intramolecular and intermolecular rearrangement in bond activation reactions as well as provide important background information necessary for understanding the results discussed remaining chapters in Part I.

2.1 Vibrational Relaxation, Geminate Recombination and Barrier Crossing in One–Electron Oxidative Addition Reactions

For a one–electron oxidative addition reaction, only a single chemical group is transferred to the transition metal center.[13] This type of chemistry is often studied in atom abstraction reactions that proceed via radical or electron transfer catalysis mechanisms. A model system that has been used to investigate this type of reaction is the halogen atom abstraction by 17–electron organometallic transient complexes. These organometallic intermediates are typically generated by homolytic photolysis of binuclear metal complexes such as $M_2(CO)_{10}$ (M = Mn, Re) and $[CpM(CO)_3]_2$ (M=Cr, Mo, W).

The photochemical reaction dynamics of $Re(CO)_5$ and $CpW(CO)_3$ in nonreactive heptane and acetonitrile solution and in reactive chlorinated $CH_xCl_{(4-x)}$ (x=0–3) solvents have been studied on a picosecond to microsecond timescale in the IR.[3,5] The purpose of these investigations was to quantify whether atom abstraction reactions proceed via 16–e^- charge transfer complexes, weakly solvated 17–e^- species, or 19–e^- intermediates. Shown in Figure 2.1 are the ultrafast spectra of $Re_2(CO)_{10}$ taken in heptane and CCl_4 solution. The 17–e^- $Re(CO)_5$ radical appears at a similar (1990 cm^{-1}) position in both solvents, indicating that the 17–e^- character of the $Re(CO)_5$ intermediate is not significantly perturbed in the coordinating CCl_4 solvent. Other than the product peaks at 1982 cm^{-1} and 2045 cm^{-1}, there are no other absorptions in CCl_4 that would imply the formation of a new species in the reaction. Consequently, the intermediate in the atom abstraction of $Re(CO)_5$ in CCl_4 is most likely best thought of as a weakly bound 17–e^-

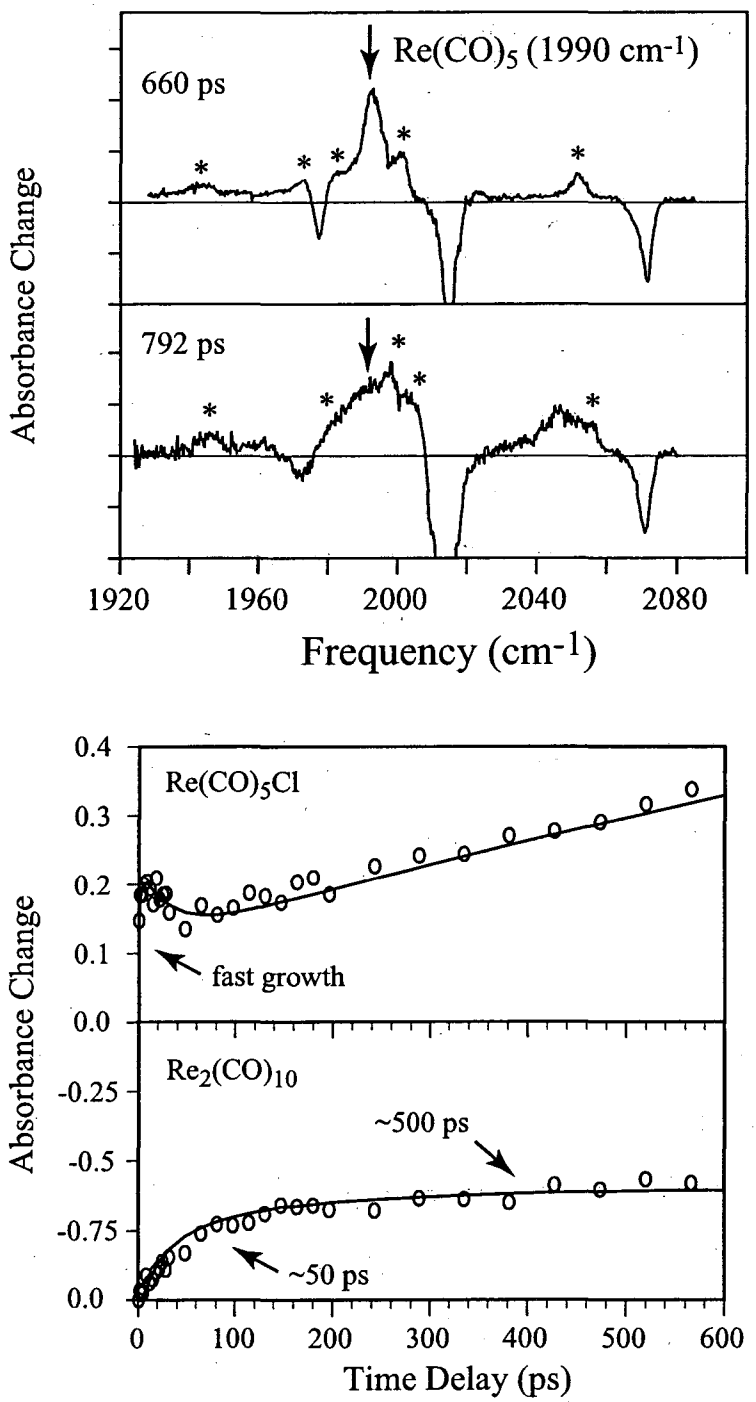

Figure 2.1 The time resolved spectra and kinetics of $Re_2(CO)_{10}$ in hexane and CCl_4. The asterisk in the spectra of panel A indicate the formation of $Re_2(CO)_9$, a non–reactive intermediate.

complex. A similar conclusion was reached in the $[CpW(CO)_3]_2$ study as discussed below. While the results of these studies clarified the nature of the transition state of these reactions, they also exemplify the general importance of vibrational relaxation, non–equilibrium barrier crossing and geminate recombination in solution phase reaction dynamics. Each of these processes may be discussed in the context of our C–Cl atom abstraction results.

Early time vibrational relaxation is an inherent process in photochemistry. This is the result of the fact that a 295 nm UV photon imparts ~100 kcal/mol energy into a molecule upon absorption. If the absorbing species quickly relaxes to a lower lying electronic excited or ground state as is often the case with organometallic compounds, that energy must be partitioned into the vibrational modes of the absorbing species. The excess energy is ultimately dissipated into the solvent bath as the molecule vibrationally relaxes.

The fact that a molecule is highly vibrationally excited manifests itself in the infrared spectra of transient intermediates.[14–16] Shown in Figure 2.2 are the time resolved IR spectra of the $CpW(CO)_3$ photoproduct formed upon 295 nm photolysis of $[CpW(CO)_3]_2$. The product peak at 1995 cm^{-1} is observed to narrow and slightly blueshift over time, indicative of vibrational relaxation of the nascent photoproduct. The inset shows the IR spectra of vibrationally excited $CpRh(CO)_2$ which has two distinct hot bands that decay within 200 ps. These spectra show that during these early times it is often difficult to distinguish nearby absorbances and to derive accurate kinetic information. As a result, we are not able to deconvolve such fast processes as solvation and geminate recombination from vibrational relaxation.

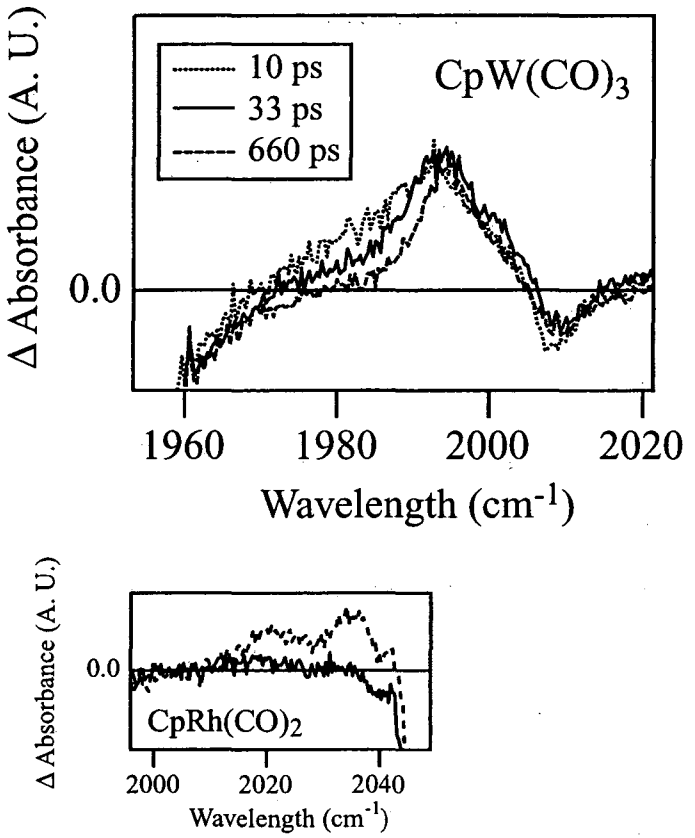

Figure 2.2 The spectral signature of vibrational relaxation of $CpW(CO)_3$ in acetonitrile and $CpRh(CO)_2$ in pentane.

The fact that a reactive photoprocuct is initially formed in highly excited vibrational states has further consequences. In the C–Cl bond activation reaction by $Re(CO)_5$, there exists an anomalously fast 2–3 ps growth component of the $Re(CO)_5Cl$ product as shown in Figure 2.1, panel B. This process has been attributed to a fast barrier crossing due to the large amount of excess energy imparted to the system following photolysis. Considering that the Re–Re bond strength is known to be ~50 kcal/mol,[17] and a single UV 295 nm photon has ~100 kcal/mol, there exist an excess of 50 kcal/mol energy that must be divided into intermolecular modes of the two $Re(CO)_5$ photoproducts. This large amount of excess energy may allow for a fast non–

equilibrium barrier crossing in a reactive media until the $Re(CO)_5$ and surrounding solvent molecules relax into equilibrium. This effect is not trivial as it is estimated that ~10% of the total product is formed via this non–equilibrium barrier crossing. The results are also general as similar observations have been made in the $[CpW(CO)_3]_2$ study.

The atom abstraction by $Re_2(CO)_{10}$ study also reveals the importance of geminate recombination. Shown in Figure 2.1 on pg. 11 are the ultrafast kinetics of the parent $Re_2(CO)_{10}$ bleach. The parent bleach appears to have biphasic recovery components of 50 ps and 500 ps as labeled in the figure. While the faster component is likely due to vibrational relaxation of hot parent molecules, the second recovery timescale is too long to be accounted for by vibrational cooling. As this recovery represents regeneration of the parent compound from the stable $Re(CO)_5$ photoproducts, the parent molecule must be reforming from the process of secondary geminate recombination.

Geminate recombination can been divided into three categories: primary, secondary, and tertiary. In primary geminate recombination, the geminal pair produced from photolysis of a parent species recombines within the solvent cage. While this has been previously thought to be a diffusive, stochastic process, early work in our lab has shown that primary geminate recombination occurs via single collisions within the solvent cage. The natural timescale for this process is on the order of a few hundred femtoseconds. In tertiary geminate recombination, the photoproducts escape the solvent shell and later recombine with the intermediates originating from other parent species. Tertiary geminate recombination is necessarily a diffusive process which occurs on a microsecond timescale.

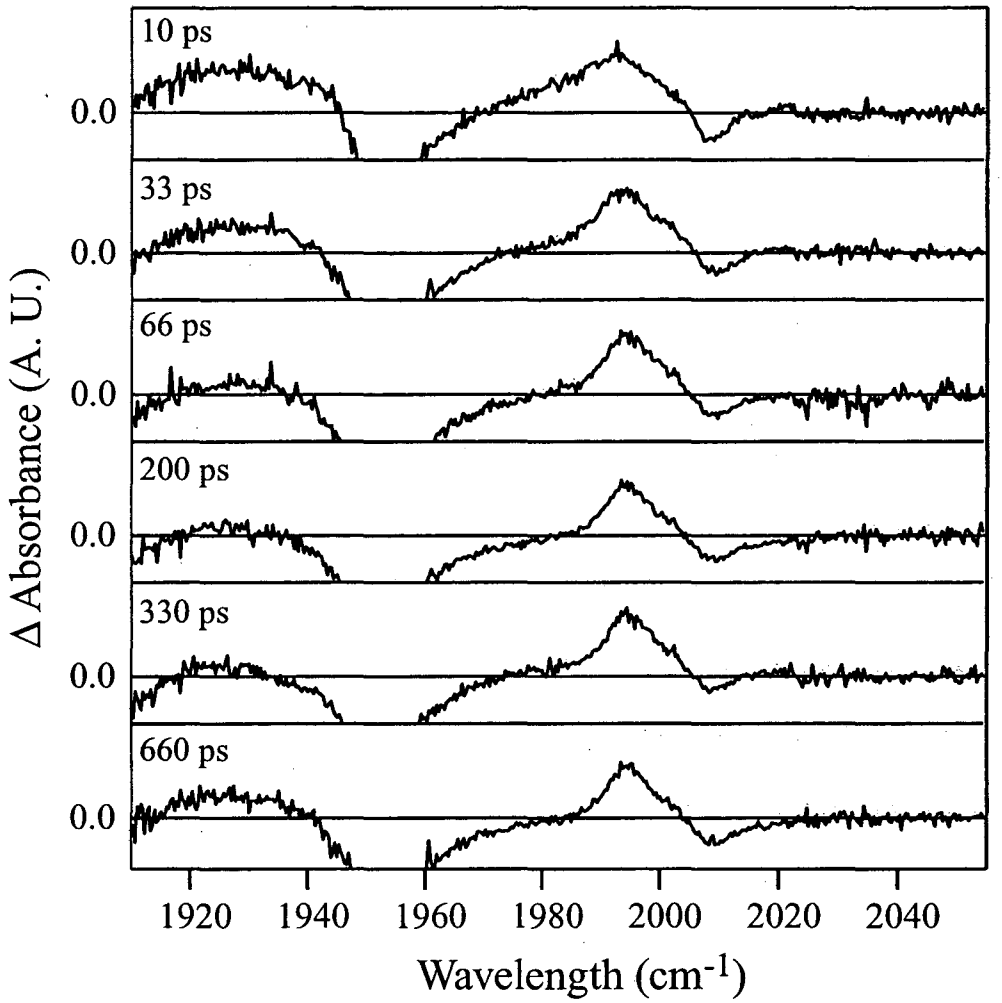

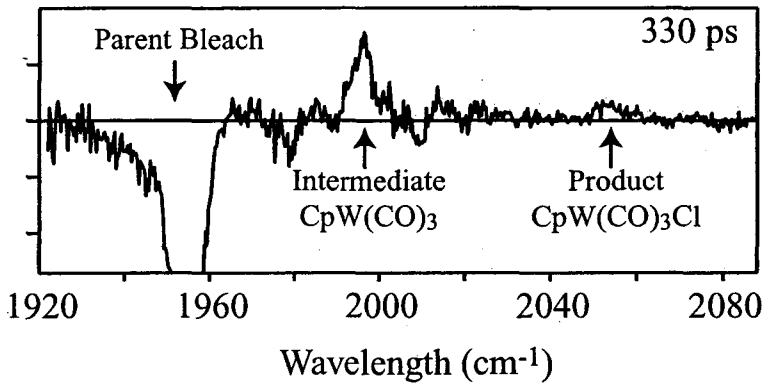

Figure 2.3 The transient difference spectra of $[CpW(CO)_3]_2$ in acetonitrile and in CCl_4.

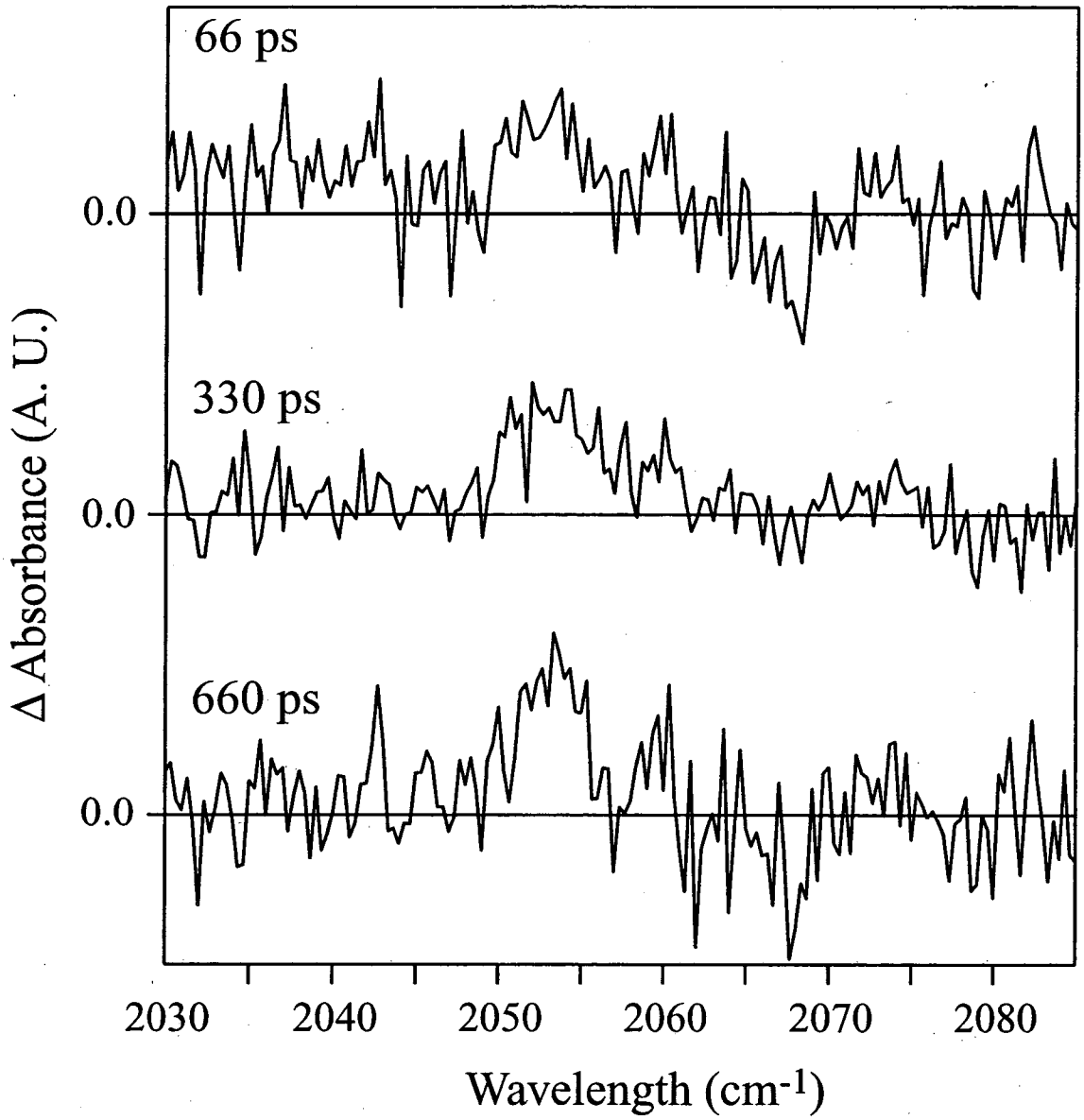

Figure 2.4 The transient difference spectra of $[CpW(CO)_3]_2$ in CCl_4 in the product region. The peak at 2053 cm^{-1} is from $CpW(CO)_2Cl$ formed from fast non–equilibrium barrier crossing.

In secondary geminate recombination the geminal pair has escaped the solvent cage, yet recombines with its original partner along an intermediate timescale. Given the fact that

the anomalous 500 ps recovery component of the parent recombination can not be attributed to vibrational relaxation, this process is most likely due to secondary geminate recombination. As the experimental results have shown that the 17–e^- intermediate $Re(CO)_5$ has weak interactions with both heptane and CCl_4 solvents, the solvent does not bind strongly to the metal center and thus can not block the recombination of the geminal pair. These results are also supported using ab initio and Density Functional Theory (DFT) calculations, which predict binding energies of less than 1 kcal/mol for CH_4 or CCl_4 with $Re(CO)_5$.[5]

As most of the conclusions discussed above were drawn from the $Re_2(CO)_{10}$ data, the C–Cl atom abstraction reaction of $[CpW(CO)_3]_2$ was studied in order to test the generality of these phenomena. The ultrafast difference spectra from the UV photolysis of $[CpW(CO)_3]_2$ in acetonitrile and CCl_4 are shown in Figure 2.3 on pages 15 and 16. In acetonitrile, parent bleaches are observed at 2010 and 1955 cm^{-1} along with product peaks at 1995 cm^{-1} and several broad, overlapped peaks centered at 1930 cm^{-1}. The 1995 cm^{-1} peak can be attributed to the 17–e^- $CpW(CO)_3$ product based upon previous flash photolysis experiments.[18] The peaks centered around 1930 cm^{-1} are likely due to absorptions from the high energy single CO–loss photoproduct $Cp_2W_2(CO)_5$. The radical intermediate absorption appears at the same position in both acetonitrile and CCl_4. As observed in the $Re(CO)_5$ studies, this indicates that the atom abstraction reaction proceeds through a 17–e^- radical intermediate that does not have strong interactions with the solvent environment.

Shown in Figure 2.4 are the difference absorption spectra of $[CpW(CO)_3]_2$ in CCl_4 in the bond activated product region at 2053 cm^{-1}. Unfortunately, it is difficult to clearly observe a product peak due to the low quantum yield, however there does appear

to be some indication of product growth within 66 ps. This product peak grows only slightly in the 330 ps spectrum and in the 660 ps spectrum. Overall the product population does not appear to increase significantly on the ultrafast timescale which is consistent with the fact that the reaction rate of C–Cl abstraction by $CpW(CO)_3$ is slower than for $Re(CO)_5$. The fact that the product appears at early times and does not have any appreciable growth can only be accounted for by a fast non–equilibrium formation of the product by vibrationally excited intermediates, otherwise the product's absorptivity would be expected to have doubled between the 330 ps to 660 ps spectra.

The results of these studies have clarified many of the details of organometallic reaction dynamics. First, the importance of non–equilibrium barrier crossing has been elucidated. It was found that the excess energy imparted to a solute allows a significant portion of the transient intermediates to cross to the product surface within 2–3 ps. Such processes as secondary geminate recombination have been observed for transient intermediates which have weak interactions with the solvent. These observations may be generalized to other chemical systems based upon the $[CpW(CO)_3]_2$ data.

2.2 Intermolecular and Intramolecular Rearrangement

A. Intermolecular Rearrangement. A major issue that our group has addressed over the past four years has been intramolecular rearrangement by coordinatively unsaturated organometallic intermediates. The importance of intramolecular rearrangements was clarified during our previous studies of Si–H activation in triethylsilane (Et_3SiH, Et = C_2H_5), in which it was found that dissociative rearrangement of a weak σ–bounded ethyl moiety of the solvent with a coordinatively unsaturated

organometallic intermediate was the rate limiting step towards formation of the final bond activated product.[2,19] Previous ultrafast visible wavelength studies suggested that this type of ligand rearrangement is the result of an intramolecular "chain walk" mechanism, in which an unsaturated metal center changes its coordination to a bound solvent molecule by hopping along the backbone of the alkyl carbon chain.[20–24] In order to clarify this issue, the ultrafast rearrangement timescales in the Si–H activation reactions of $M(CO)_6$ (M=Cr, Mo, W) and $CpCr(CO)_3$ ($Cp=C_5H_5$) in a series of substituted silanes were measured using UV pump IR probe spectroscopy.[25]

The results of our study have confirmed that ligand rearrangement is a dissociative stochastic process. The rearrangement timescale among a series of coordinatively unsaturated organometallic species was found scale with the known binding enthalpies of the alkyl solvated complex, which is consistent with a dissociative mechanism. These results will be used to contrast the results observed for high spin intermediate species which do not have strong interactions with alkanes or the alkyl moiety of a solvent molecule. Recent simulations, however have shown this to be the limiting form of a general mechanism proposed in Chapter 9.

B. Intramolecular Rearrangement. Our previous results on C–H bond activation by η^3–Tp*Rh$(CO)_2$ elucidated the importance of intramolecular rearrangement in organometallic chemistry.[1,26] The findings may be summarized as follows.

Dissociative (Low Spin) Mechanism

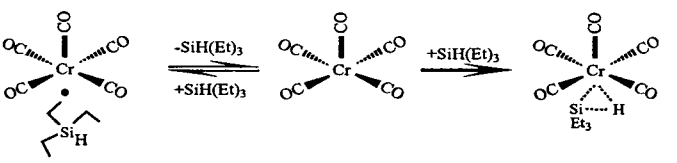

Scheme 2.1. The dissociative mechanism of ligand rearrangement following photochemical CO loss of $Cr(CO)_6$ in triethylsilane.

Upon UV photolysis, the parent

compound η^3–Tp*Rh(CO)$_2$ loses one CO ligand and becomes quickly solvated in alkane solution. This photoproduct decays within 200 ps to form a dechelated η^2–Tp*Rh(CO)(alkane) intermediate. Within 200 ns in cyclohexane, a C–H bond is likely activated and the loss of electron density at the metal center is the driving force for the pyrazolyl arm to reattach itself back to the metal center, forming the product η^3–Tp*Rh(CO)(H)(R). These results are important as they show that the dynamics of the ligand is also a significant factor in bond activation. Consequently, both intermolecular and intramolecular rearrangements are important dynamical processes which influence the chemical reaction dynamics in liquids. The effect of the hydrocarbon structure on the activation process is the subject of Chapter 6.

Section 2.3 Conclusions

The themes of intermolecular and intramolecular rearrangements, geminate recombination, non–equilibrium barrier crossing, and vibrational relaxation are common elements in all of the photochemical bond activation research that our group as conducted over the past several years. Due to the inherent nature of photochemistry, the initially formed products are in highly excited vibrational states. As a result, the spectra of these new intermediates are altered and difficult to interpret until these species have vibrationally relaxed. This process occurs on a typical timescale of a few tens of picoseconds. The excess energy of the transient intermediates may channel into a reaction coordinate and thus result in the fast formation of products. Geminate recombination also manifests itself at early times. Due to lack of strong solute / solvent interactions, secondary geminate recombination has been observed for the radical species Re(CO)$_5$ formed upon UV photolysis of Re$_2$(CO)$_{10}$. In the process of chemical bond

activation, the role of ligand dynamics has been elucidated in the case of C–H activation by Tp*Rh$(CO)_2$. The rearrangement of "token" ligands has also been shown to be the rate determining factor in our previous Si–H activation studies.

Chapter 3

The Role of High Spin Intermediates in Si–H Activation

3.1 Introduction

The photochemical oxidative addition of a Si–H bond to certain transition–metal complexes has been the focus of many research efforts since its initial discovery by Jetz and Graham in 1971.[27] This type of bond–activation reaction is critical in hydrosilation processes and provides a comparison to C–H bond activation by other organometallic complexes.[28,29] Our group was the first to elucidate the mechanism of the Si–H bond activation reaction of the Group 7, d^6 organometallic compounds η^5–$CpM(CO)_3$ (M = Mn, Re; Cp = C_5H_5) in triethylsilane through direct observation.[2,19] The findings of this study were novel due to the fact that multiple photoproducts were observed in the $CpMn(CO)_3$ spectra. One of the two primary photoproducts was identified as singlet $CpMn(CO)_2$. As discussed in sec. 2.3 of Chapter 2, this singlet intermediate may be initially solvated via the ethyl moiety of triethylsilane, forming an alkyl adduct which later rearranges to the final bond activated product via a dissociative, stochastic mechanism. Solvation of the singlet species via the Si–H bond leads directly to the product. Another unidentified intermediate, which was also a direct photoproduct of the parent $CpMn(CO)_3$, reacted on a much faster timescale with triethylsilane. While it was initially suggested that the identity of this species is a ring slipped 14–e^- η^3–$CpMn(CO)_2$ intermediate, the use of theoretical calculations suggest that a high spin

unsolvated 16–e$^-$ η^5–CpMn(CO)$_2$ complex is a more likely assignment. However, as examples of the reactivity of coordinatively unsaturated high spin organometallic compounds are rare, the generality of these conclusions could not be resolved.

In our subsequent investigation of the Si–H activation reaction by the d^4 organometallic compound η^5–CpV(CO)$_4$,[30] our group made an unexpected discovery. As shown in Figure 3.1 on pg 25, the difference spectra resulting from the photolysis of η^5–CpV(CO)$_4$ in heptane solution shows absorptions due to solvated singlet η^5–CpV(CO)$_3$(heptane) at 1895 cm^{-1} and 1990 cm^{-1} as well as a new intermediate at 2020 cm^{-1}. While this new intermediate absorption appears relatively constant to 660 ps, this species is very reactive in triethylsilane solution. In light of the previous η^5–CpMn(CO)$_3$ study, the most likely explanation of the identity of this intermediate is a single CO loss high spin η^5–CpV(CO)$_3$ photoproduct. This assignment is also supported by theoretical results.

The purpose of the CpV(CO)$_4$ study was to extend the study of Si–H activation of silanes to Group 5 organometallic compounds. In previous studies Rest et al. have proposed that a coordinatively unsaturated, single CO loss product 16–e$^-$ CpV(CO)$_3$ species and ring slipped η^3–CpV(CO)$_4$ is formed upon UV irradiation of CpV(CO)$_4$ in low temperature matrices.[31,32] In the presence of Et$_3$SiH these intermediates are known to from the arrested oxidative addition product CpV(CO)$_3$(η^2–HSiEt$_3$).[33] There have been no studies, however, of the early time dynamics of the reaction mechanism due to the extremely fast reaction rates. As will be shown below, the exact nature of the early time transient intermediates is elucidated in these studies.

3.2 Experimental Results

A. Photolysis of $CpV(CO)_4$ in heptane. The photolysis of $CpV(CO)_4$ in heptane was studied in order to provide a basis for comparison to the triethylsilane data. Shown in Figure 3.1 are the fs–IR difference spectra of $CpV(CO)_4$ in neat heptane following excitation at 295 nm. There are three broad and red–shifted peaks appearing in the spectra at 10 ps that quickly sharpen and blueshift at later times, indicative of vibrational cooling the nascent photoproducts.[14–16] Based on previous matrix isolation and room temperature experimental results,[33] the peaks at 1895 and 1990 cm^{-1} are attributed to singlet η^5–$CpV(CO)_3$(heptane) as denoted in the figure. The third peak at 2020 cm^{-1} is another intermediate formed directly from the photolysis of $CpV(CO)_4$, which will later be shown to be a triplet $CpV(CO)_3$ intermediate. Also shown in Figure 3.1 are the kinetic traces of all the intermediate species observed in this study. The intermediate absorbing at 2020 cm^{-1} shows a fast 6.3 ± 1.9 ps rise followed by a bi–exponential decay of 50 ± 10 ps and a much longer time component (>>1 ns), which can not be accurately determined within the limitations of our spectrometer. The fast rise is attributed to the vibrational cooling of the hot photoproduct, while the 50 ps decay components appear to represent conversion of this species to the solvated singlet $CpV(CO)_3$(heptane). It can be seen that the singlet tricarbonyl displays a bi–exponential formation with time constants of 6.6 ± 5.7 and 39.3 ± 3.3 ps, respectively. The fast time component is attributed to vibrational cooling while the longer growth time mirrors the slight decay of the unknown intermediate, suggesting that the two are kinetically coupled.

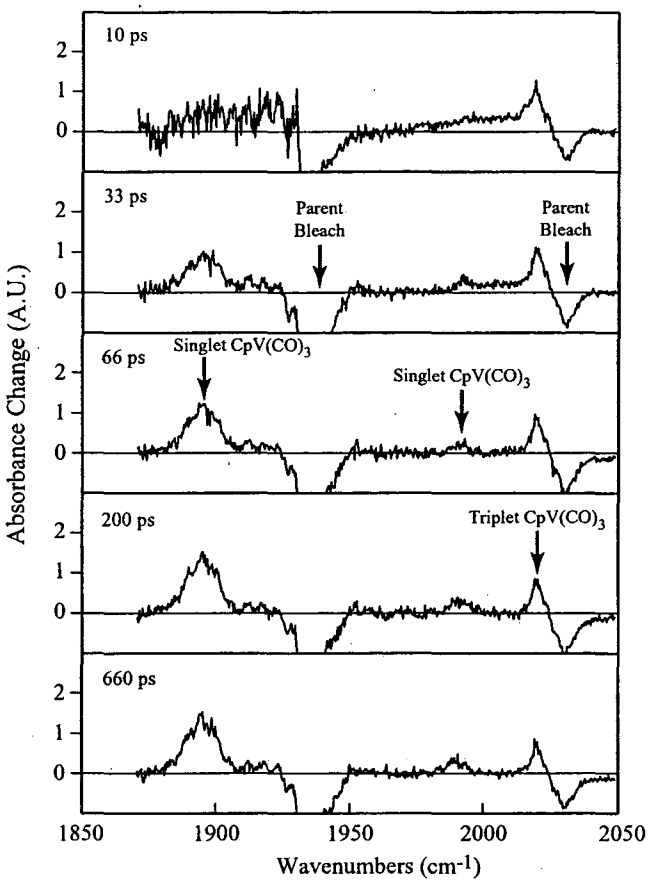

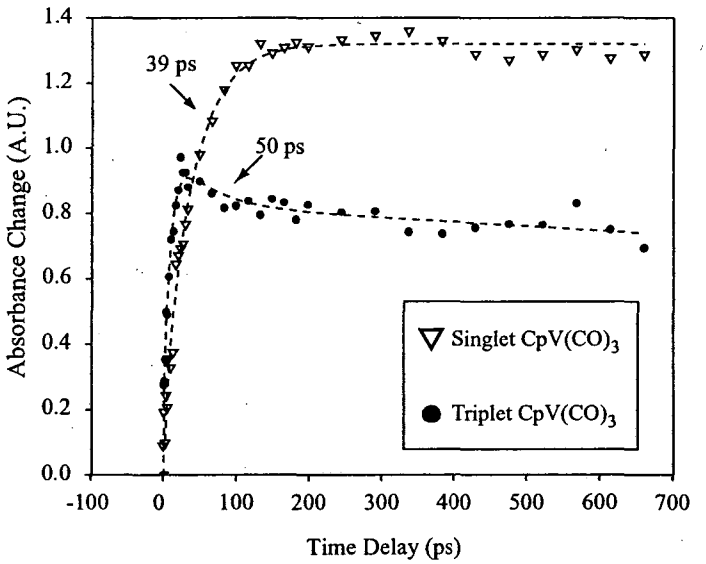

Figure 3.1 The ultrafast spectra and kinetics of $CpV(CO)_4$ in heptane solution.

The presence of three intermediate peaks in the transient spectra must be accounted for by the formation of at least two photoproducts, as the expected tricarbonyl with local C_{3v} symmetry will have only two CO absorption peaks. While the bands at 1990 and 1895 cm^{-1} have already been assigned as the singlet η^5–$CpV(CO)_3$ photoproduct, two possible candidates for the transient intermediate observed at 2020 cm^{-1} may be proposed: a ring–slipped η^3–$CpV(CO)_4$,[29,30] or triplet η^5–$CpV(CO)_3$. Evidence points toward the identity of the unknown photoproduct to be a triplet tricarbonyl. There are precedents for 16–e^- organometallics having triplet ground states,[34–37] the geometry and force constants of which may differ from that of the singlet state to allow different ligand vibrational frequencies.[38,39] Further, the assignment of this intermediate as a ring slipped is not consistent with the fact that the decay of the intermediate is concomitant with the rise of the solvated singlet η^5–$CpV(CO)_3$(alkane) in heptane solution as well as η^5–$CpV(CO)_3(HSiEt_3)$ in triethylsilane solution, unless solvation of η^3–$CpV(CO)_4$ is accompanied with ring closure and CO loss in a complicated concerted process. Given the large (~50 kcal/mol) bond strengths of metal–CO bonds, this possibility is highly unlikely. The assignment of a triplet state intermediate is supported by theoretical calculations, as discussed below.

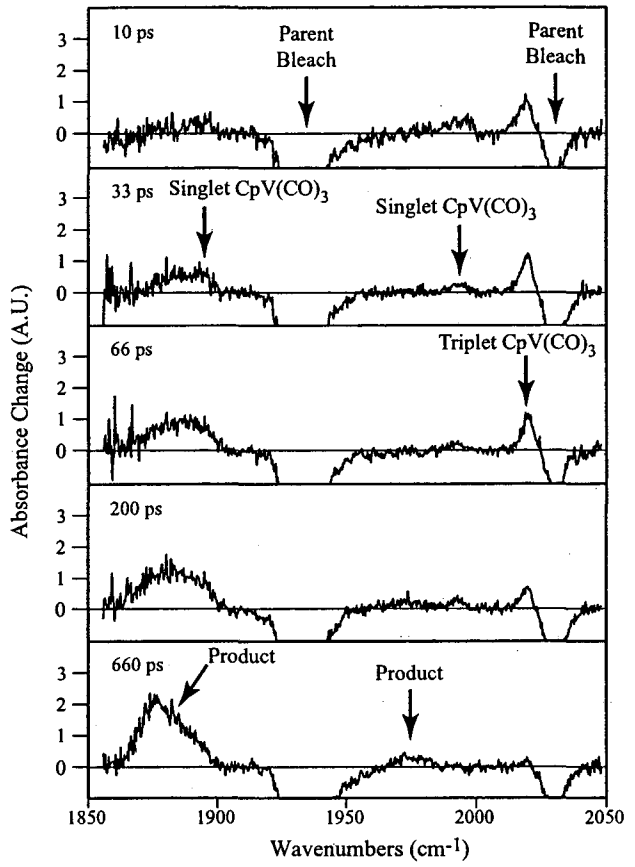

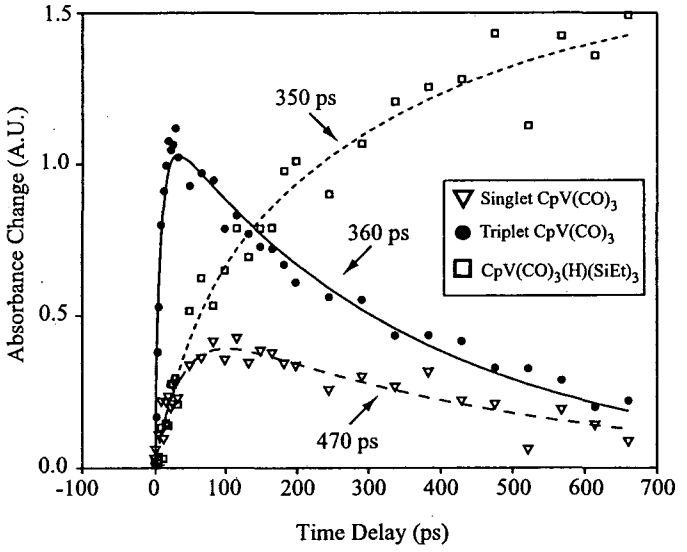

Figure 3.2 The ultrafast spectra and kinetics of $CpV(CO)_4$ in triethylsilane solution.

B. Activation of the Silicon–hydrogen Bond of Et_3SiH by $CpV(CO)_4$. Shown in Figure 3.2 on page 27 are the fs–IR spectra of $CpV(CO)_4$ in neat Et_3SiH following excitation at 295 nm. The peaks at 1876 and 1973 cm^{-1} are assigned to the product η^5–$CpV(CO)_3$ (η^2–$HSiEt_3$), and based on the heptane results the peaks at 1895 cm^{-1} and 1990 cm^{-1} are attributed to singlet $CpV(CO)_3$ solvated by the ethyl moiety of triethylsilane. The band appearing at 2020 cm^{-1} is attributed to the triplet tricarbonyl species as observed in the alkane results. Also shown in Figure 3.2 are the kinetic traces of all the intermediate species as well as the product following 295–nm excitation. The kinetics of the triplet recorded at 2020 cm^{-1} exhibit a fast 8.8 ± 0.3 ps rise followed by a 360 ± 10 ps decay. The ethyl solvated singlet displays a similar kinetic behavior as the triplet species, with a rise time of 36 ± 6 ps followed by a 465 ± 75 ps decay. The product band of the product at 1876 cm^{-1} displays a bi–exponential rise of 55 ± 6 ps and 350 ± 140 ps. Clearly, the decay of both the high and low spin intermediates is correlated to the formation of the final product. Since the timescale for the total intersystem crossing of the triplet to the singlet species in a non–reactive alkane media is much greater than 1 ns, it is unlikely that the decay of the triplet intermediate in triethylsilane can be attributed to spin crossover to the ethyl solvates singlet.

3.3 The Dynamics of High Spin Intermediates.

In our previous study it was found that η^5–$CpM(CO)_3$ (M = Mn, Re) formed coordinately unsaturated 16–e^- dicarbonyl species via CO loss upon photolysis. The dynamics of the singlet species are best summarized from the Re data. For singlet $CpRe(CO)_2$, the reaction coordinate is divided into two distinct channels by the initial

solvation: formation of an ethyl moiety via solvation of the ethyl group and activation of the Si–H bond via Si–H solvation. The ethyl moiety decayed into the final bond–activated product via a dissociative mechanism on a microsecond timescale. The Mn complex mechanism was found to be partitioned between singlet and triplet pathways. While the singlet $CpMn(CO)_2$ species reacted via the same mechanism as singlet $CpRe(CO)_2$, an unsolvated triplet $CpMn(CO)_2$ species was also formed which decays to the singlet ethyl solvate and of the final product in a concerted spin crossover / solvation process. The $CpV(CO)_4$ results provide a basis for comparison to the previous data, especially concerning the reactivity of the triplet state.

After UV excitation in neat triethylsilane, the parent molecule η^5–$CpV(CO)_4$ quickly loses one CO ligand to produce two tricarbonyl species. Based upon the similarities to the ultrafast spectra in heptane, the intermediates are assigned as a singlet ethyl solvated species and a triplet unsolvated tricarbonyl. Both of these species decay on a picosecond timescale to form the final product, although the triplet species is the overall more reactive of the two intermediates. There are a few important differences in the dynamics of the photogenerated intermediates in different solvents. First of all, there exists an increase in triplet / singlet population ratio in triethylsilane compared to in heptane as shown in Figures 3.1 and 3.2. This is suggestive of either a fast depletion of the singlet species at early times in triethylsilane or that there is a change in the branching ratio between triplet and singlet formation in the different solvents. Unfortunately, it is difficult to differentiate between these two possibilities as the early time dynamics of this system are clouded by vibrational relaxation.

In the context of the unknown intermediate being a triplet state η^5–$CpV(CO)_3$, we next discuss the interaction of the triplet species and the solvent. It has been

suggested theoretically that transition metals in their triplet state interact only weakly with alkane solvents.[39] Previous femtoseconds UV pump IR probe experiments with $CpCo(CO)_2$ have shown disparate lifetimes for the triplet intermediate CpCo(CO) intermediate in non reactive alkane and strong coupling solvents. Our own experimental results on this system as well as coordinatively unsaturated triplet $Fe(CO)_4$ strongly suggest that high spin intermediates have weak interactions with alkanes. This finding is strongly supported by theoretical results and is the subject of Chapter 4 and Chapter 5. Hence strongly interacting solvent molecules need to be considered in describing the reaction coordinate for spin–crossover and solvent exchange. As the triplet species quickly decays to product in triethylsilane, it would appear that a triplet transition metal complex is preferentially solvated by the more strongly coupling sites of a solvent molecule. Based on the arguments above, our data suggest that the triplet species, which is long lived in a nonreactive alkane solvent, is quickly depleted directly via a concerted spin crossover / solvation through the Si–H bond of the solvent molecule.

The solvation and reaction dynamics of the singlet species is very different from that of the triplet. The nascent singlet η^5–$CpV(CO)_3$ is initially solvated via the ethyl moiety of Et_3SiH, most likely due to steric hindrance and statistical favor of the ethyl groups over the Si–H bond. This alkyl solvated adduct then rearranges to form the product on a timescale of ~470 ps. The mechanism of this rearrangement has been the subject of through research, as described in Ch.2. Based upon a battery of experiments, it was found that the ligand rearrangement of the Group 6 pentacarbonyls occurs via a dissociative mechanism as summarized in Scheme 2.1 on page 19. Unfortunately, it is not clear whether a dissociative mechanism is applicable to the $CpV(CO)_3$ system. The ligand rearrangement of $CpV(CO)_3$ in triethylsilane is complete on the ultrafast

timescale, which is several orders of magnitude faster than what was observed for the d^6 Re and Mn intermediates. This is true despite the greater steric hindrance of the vanadium tricarbonyl species. The large increase in the rate of ligand rearrangement may be a consequence of a weaker metal–heptane interaction which facilitates dissociation, however we are unable to rule out other mechanisms such as chain–walk for this particular rearrangement.

Overall, it was found that the mechanism of Si–H photochemical activation by the d^4 $CpV(CO)_4$ species is very similar to what had been observed for $CpMn(CO)_3$. The reaction is divided into parallel pathways involving high and low spin coordinatively unsaturated intermediates. The high spin species has weak interactions with the solvent yet forms the final product via a concerted Si–H solvation / intersystem crossing mechanism. The low spin species is solvated by the alkyl moiety of triethylsilane, which later rearranges to form the final product on the ultrafast timescale.

3.4 DFT and *ab initio* Calculation Results

While the experimental results provide a clear picture of the reactive mechanism of these species, the conclusions are augmented from theoretical calculations. These results provide further insight into the nature of the transient species that cannot be characterized using conventional methods and may explain trends seen in the experimental results. Specifically, the assignment of the unknown intermediate as triplet $CpV(CO)_3$ and the calculation of the singlet $CpV(CO)_3$(heptane) binding energies support the proposed mechanism discussed above.

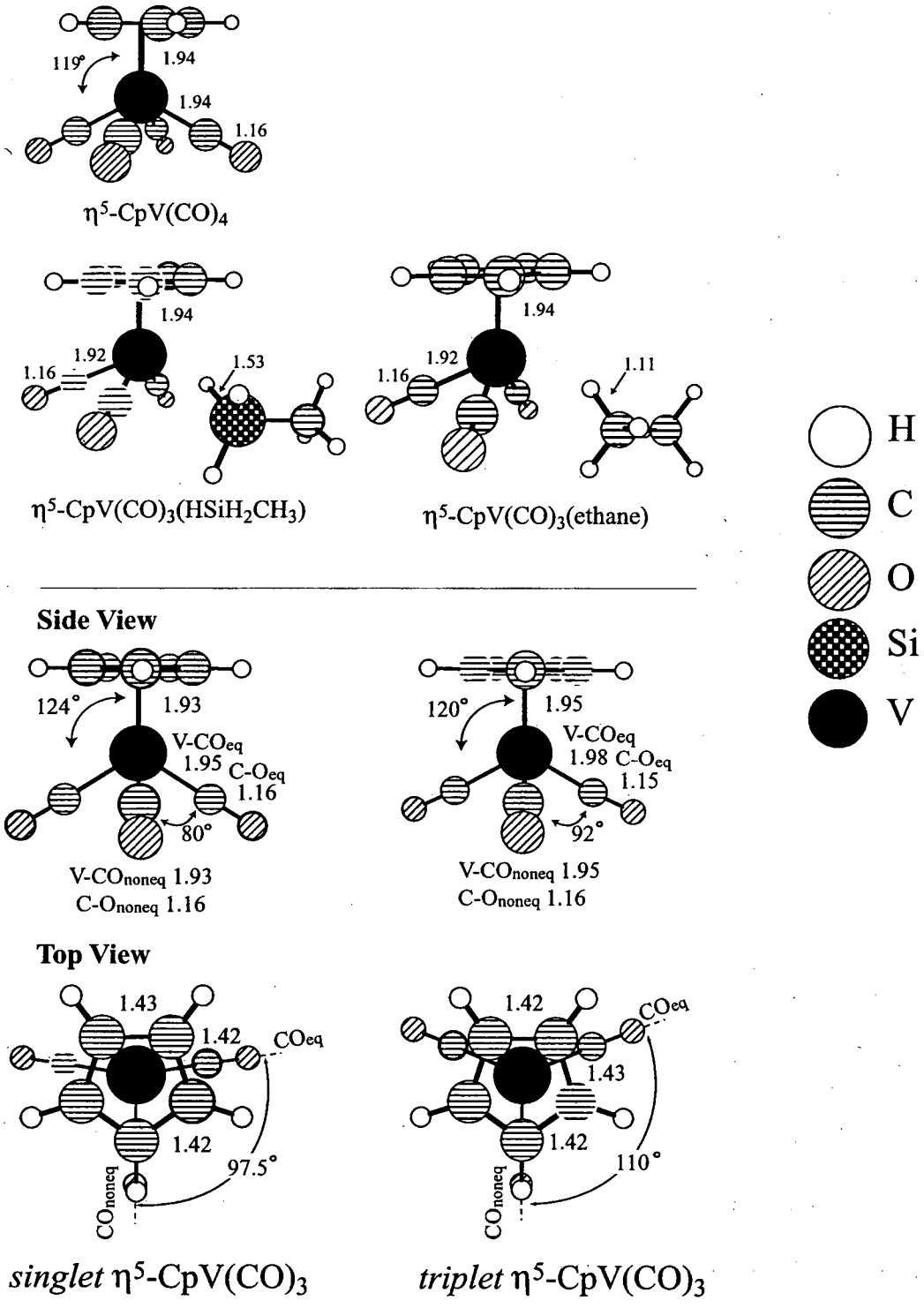

Figure 3.3 The DFT structures of various species observed in the $CpV(CO)_4$ study.

We first turn to the identity of the intermediate which absorbs at 2020 cm^{-1}. Shown in Figure 3.3 are the geometries for the 16–e^- species η^5–$CpV(CO)_3$ in its singlet and triplet states calculated at the 6–31G**/B3LYP level of theory.[10,11,40–42] All calculations were performed with the Jaguar package.[7] Despite the overall similarity of the singlet and triplet species, one notices a difference in the OC–M–CO angle. For example, the angle between the OC_{eq}–M–CO_{non-eq} bonds increases from 80° in the singlet to 92° in the triplet state. Projected into the plane of the cyclopentadienyl ring, the triplet species has the carbonyl ligands arranged in a more trigonal fashion, while the singlet state is less symmetric. In addition, the V–Cp and M–CO distances are longer in the triplet species than in the singlet and the equivalent CO bond lengths are shorter in the triplet compared to the singlet. Such a decrease in the metal–CO interaction in the triplet state has also been observed in calculations of CpM(CO) (M = Co, Rh, and Ir),[43] as well as our own calculation of $CpM(CO)_2$ (M = Mn and Re)[2]. Despite repeated attempts we were unable to converge a structure for a ring slipped η^3–$CpV(CO)_4$ intermediate.

A comparison relative energies of the singlet and the triplet η^5–$CpV(CO)_3$ provides an interesting example of the use of theoretical calculations in the assignment of unknown species. While the DFT results predict a lower energy for the triplet η^5–$CpV(CO)_3$ state relative to that of the singlet (ΔE = 3.10 kcal/mol), the ab initio results were very inconsistent. To the Hartree–Fock level of theory, the triplet is the lower energy species, in contrast to the MP2 results that predict a singlet ground state. These results are to be expected when dealing with near degenerate spin states, which is common for transition metal complexes that have a high density of states. This type of

degeneracy causes an effect known as "spin contamination", which means that the calculated wavefunction contains contributions from higher spin states and will consequently have too large a value of $<S^2>$. The use of Moller–Plesset theory is thus incorrect as it is not a degenerate perturbation theory. The only method currently available which properly describes these cases is CASSCF. This type of calculation represents a complete solution to the Schrodinger equation in a limited active space and is known to include the effects of static (low frequency) correlation effects. Quasi–degenerate perturbation theory calculations may also be performed on the CASSCF wavefunction to include the effects of dynamic correlation.[44] The lanl2dz basis set was used for the pt2–CASSCF calculations which had an active space of 10 occupied and unoccupied d–type orbitals.[42,45–47] These results agree with the DFT results predicting a ground triplet state for $CpV(CO)_3$. Finally, numerical CO stretching frequencies at DFT level were calculated for the singlet η^5–$CpV(CO)_3$(methane) [2025 and 2090 cm^{-1}] and for the triplet η^5–$CpV(CO)_3$ [2039 and 2113 cm^{-1}] as well as the parent η^5–$CpV(CO)_4$ [2044 and 2115 cm^{-1}] fit the trends seen in the data. Overall, these results show that a high spin species $CpV(CO)_3$ is the most likely candidate for the unknown intermediate.

Theoretical calculations can also elucidate the nature of the singlet intermediate as well as the products. Shown in Figure 3.3 are the geometries of the parent molecule η^5–$CpV(CO)_4$, the singlet tricarbonyl metal solvated by an ethane molecule η^5–$CpV(CO)_3$(ethane), and the final product η^5–$CpV(CO_3H)(SiH_2CH_3)$ optimized at the DFT/B3LYP level of theory. The metal–Cp and metal–CO distances for the parent molecule agree reasonably well with the gas phase experimental values,[48] except for

the slightly overestimated C–O bond lengths. For the ethane tricarbonyl complex in Figure 3.3, the ethane molecule interacts with the metal center via one of its C–H bonds via an η^2 interaction. The bond length for the coupling C–H bond is 1.11 Å, which is slightly extended by +0.02 Å compared to 1.09 Å for the C–H bond of free ethane from the same level of theory. This suggests that the vanadium metal center interacts weakly with a C–H bond which supports the notion that the alkyl solvated intermediate dissociatively rearranges to form the final product in triethylsilane. Finally, the Si–H bond distance in the final product demonstrates the extent of the Si–H bond activation. The calculated Si–H bond length for the metal complex is 1.53 Å compared with the monomer silane Si–H bond length of 1.49 Å for a net increase in 0.04 Å in the product species. This observation is in agreement with the known fact that the final Si–H solvated species is in an arrested oxidative addition state.

Overall, theoretical calculations of this nature help us to gain insight as to the nature of the reactants, intermediates and products. The identity of unknown intermediates may be supported by the results of these methods which helps us to devise a comprehensive reaction mechanism.

Section 3.5 Conclusion

The results of this study confirmed our earlier conclusions concerning the dynamics of coordinatively unsaturated organometallic species. Triplet $CpV(CO)_3$ was found to react as a faster rate than the singlet counterpart, although the difference in reactivity was less disparate than what had been observed in the $CpMn(CO)_3$ study. Theoretical calculations were found to be invaluable in characterizing the transient intermediates as well as the parent and product compounds.

The observation of a second transient unsaturated triplet species prompted our group to study and characterize more of these intermediates. Based upon previous studies, it was likely that triplet intermediates would be formed from the photolysis of $CpCo(CO)_2$ and $Fe(CO)_5$. Our group's efforts in characterizing these species, as well as triplet intermediates in general, is the subject of the next two chapters.

Chapter 4

High Spin Dynamics of $Fe(CO)_4$ and CpCo(CO)

The observations of previously unknown high spin intermediates formed upon the photolysis of $CpMn(CO)_3$ and $CpV(CO)_4$ represent a significant step in the understanding of triplet coordinatively unsaturated species. The observation that high spin intermediates react in triethylsilane at faster rates than corresponding singlet intermediates is interesting considering the general notion high spin species are less reactive. This unusual observation has been proposed to be a result of the strong coordination of alkanes with singlet species, forming long lived alkyl solvates which represents a local minimum in the potential energy surface. High spin species do not coordinate with alkanes and are thus free to react with the Si–H bond along a much shorter timescale.

The results of these previous studies have left several questions unanswered. For one, all of the conclusions were drawn upon the observations of only two transition metal systems in which even the assignments of the high spin intermediates were questioned. Further, the factors that govern the rate at which the high spin species reacts were not elucidated due to the lack of more examples of high spin reactivity. The generality of the proposed mechanism was also not well established. In order to address these issues, our group has studied the photochemistry of $Fe(CO)_5$, $CpCo(CO)_2$ and $CpRh(CO)_2$ in nonreactive alkane and in triethylsilane solutions.[49] These studies, in conjunction with previous results and theoretical ab inito and DFT calculations, have elucidated the factors that govern high spin reactivity.

This chapter is outlined as follows. The background information of the photochemistry of $Fe(CO)_5$, $CpCo(CO)_2$ and $CpRh(CO)_2$ are given in section 4.1. The experimental results are shown in section 4.2 and an interpretation is given in section 4.3. The results of the ab initio and DFT calculations, which are invaluable to the understanding of the reactivity of these species, are discussed in section 4.4.

Section 4.1 Introduction

The photochemistry of $CpCo(CO)_2$ has been extensively studied by several groups.[34,50,51] Using theoretical calculations, Siegbahn et. al. have shown that the known single CO loss photoproduct CpCo(CO) has a triplet electronic ground state.[52] This result is consistent with the experimental observations of Bengali et. al., which indicate that triplet CpCo(CO) does not coordinate strongly with alkanes and is thus incapable of activating C–H bonds.[32] These results contrast to the photochemical properties of the isoelectronic compound $CpRh(CO)_2$, which is known to bind strongly with alkanes as well as activate CH bonds.[53] These observations indicate that the photoproduct CpRh(CO) has a singlet ground state. The likelihood of observing and characterizing the reaction dynamics of a triplet CpCo(CO) intermediate makes this system an ideal example to study in order to develop an understanding of high spin species. The photochemistry of $CpCo(CO)_2$ has been characterized in triethylsilane and compared to the results for the isoelectronic compound $CpRh(CO)_2$. The difference in the rate of reaction between the singlet and triplet intermediates of these species highlights the effect of spin state on reactivity.

The photochemical reaction dynamics of $Fe(CO)_5$ has also been the subject of through study in the literature.[54–58] It has been established that both singlet and triplet $Fe(CO)_4$ are formed upon photolysis of $Fe(CO)_5$ in the gas phase and in matrix

isolation studies; likewise Burkey and Nayak have shown that triplet $Fe(CO)_4$ is formed in room temperature alkane / phosphine solution.[59,60] While other authors have suggested that the unusual reaction dynamics observed by Burkey and Nayak are due in part to singlet $Fe(CO)_4$, [61] we have found no evidence of singlet $Fe(CO)_4$ formation in room temperature solution on the ultrafast timescale. Consequently, the photochemistry of $Fe(CO)_5$ is important as an example of triplet reactivity. Given the large amount of attention in the literature that is devoted to photochemical studies of $Fe(CO)_5$, it is odd that our study represent the first ultrafast examination of this species in solution. Fortunately, our results have clarified many of the issues associated with the photochemistry of $Fe(CO)_5$ which are further explored in Chapter 5.

Section 4.2 Experimental Results

A. Photolysis of $CpCo(CO)_2$, $Fe(CO)_5$ and $CpMn(CO)_3$ in alkane solution. The photolysis of $CpCo(CO)_2$, $Fe(CO)_5$ and $CpMn(CO)_3$ in alkane solution has been studied. These results are used in the discussion section to compare the reactivity of singlet and triplet species in alkane and triethylsilane solution.

Upon 325 nm photolysis of $CpCo(CO)_2$ in heptane solution, a single monocarbonyl peak appears at 1990 cm^{-1} on a timescale of 12 ± 2 ps and remains constant to 660 ps. The time resolved spectra are given in Figure 4.1 on page 40. Also shown in Figure 4.1 are the difference spectra of $Fe(CO)_5$ in heptane following 295 nm

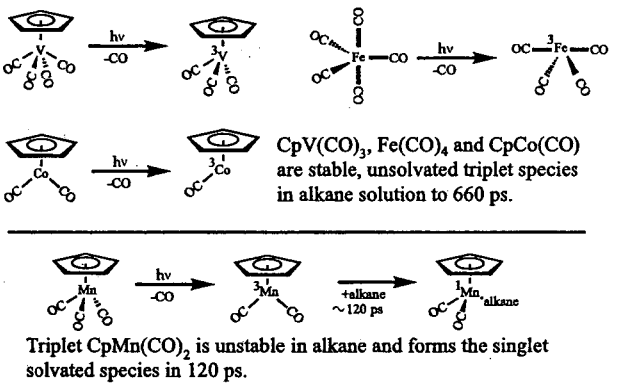

Scheme 4.1. The dynamics of high spin intermediates in alkane solution.

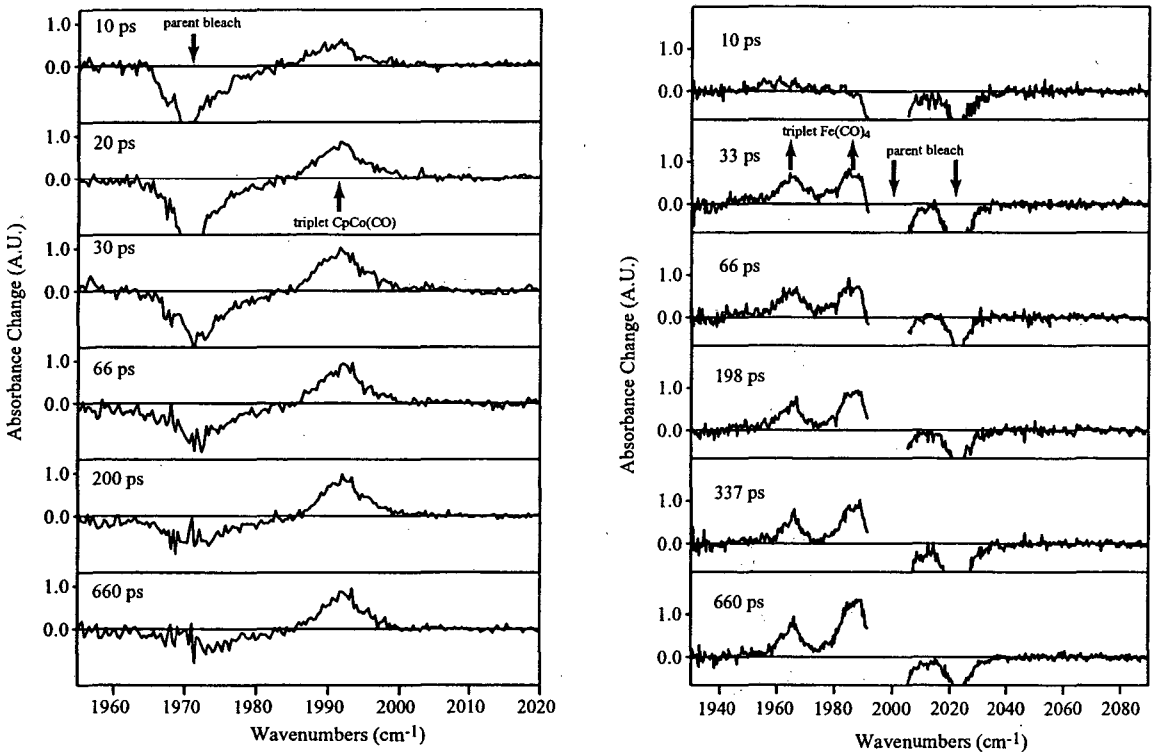

Figure 4.1 The difference spectra of $CpCo(CO)_2$ (left) and $Fe(CO)_5$ (right) in heptane following UV photolysis.

photolysis. Instantaneous parent bleaches and the 26 ± 12 ps formation of a new photoproduct absorbing at 1965 cm^{-1} and what appear to be two overlapped bands centered at 1987 cm^{-1} are observed. This photoproduct appears to be stable to 660 ps. The rise times of these iron and cobalt species may be attributed to vibrational relaxation of the initially hot photoproduct due to the slight broadening and blue shifting of the absorption peak at early times.[14–16] The assignments of these photogenerated intermediates are given in the discussion.

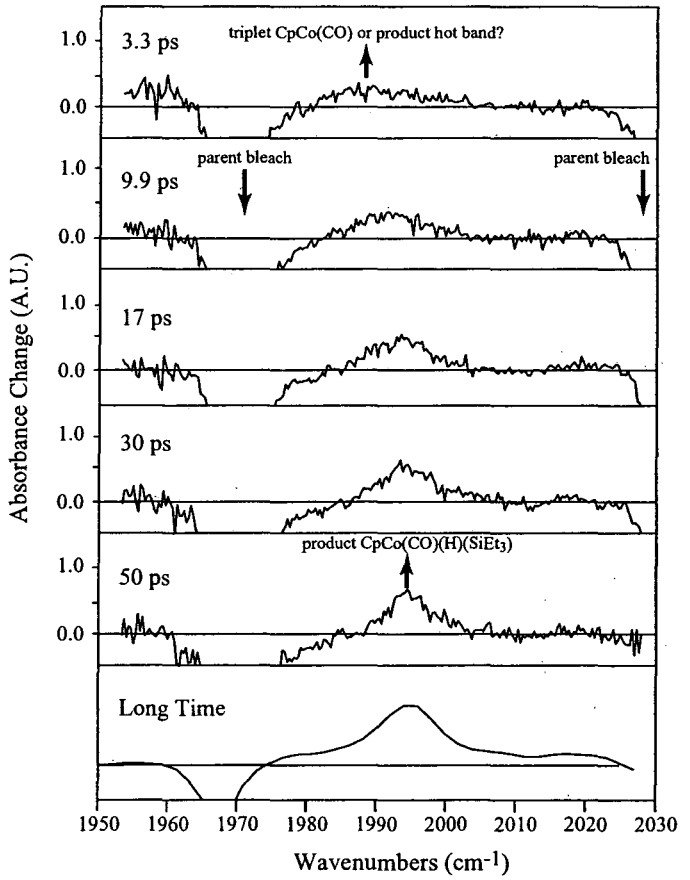

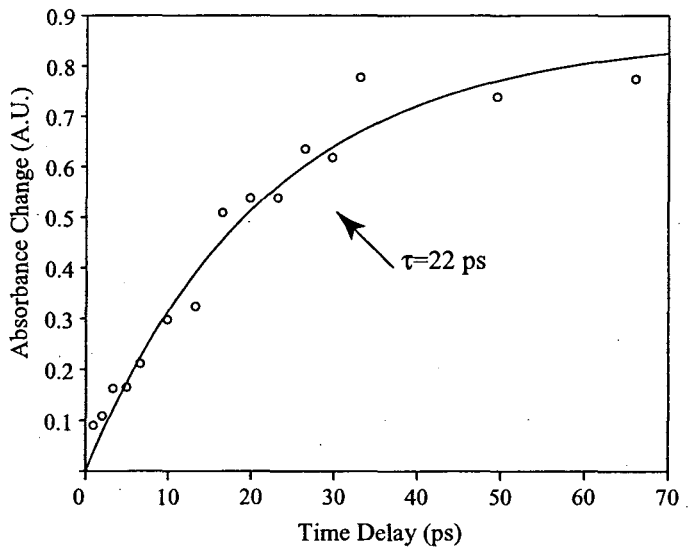

Figure 4.2 The difference spectra and kinetics of $CpCo(CO)_2$ following photolysis in triethylsilane.

The dynamics of photogenerated singlet and triplet $CpMn(CO)_2$ in n–pentane had been studied during the earlier triethylsilane studies, however the results were not reported.[2] Following excitation at 295 nm, it was found that the triplet species is unstable in n–pentane and decays with a time constant of τ=119 ± 5 ps. The loss of the triplet intermediate results in the formation of the singlet alkane solvated species as shown in Scheme 4.1. The published value of the decay of the triplet species in triethylsilane (τ=105 ps) is very similar.[2]

B. Activation of the Silicon–hydrogen Bond of Et_3SiH by $CpCo(CO)_2$, $CpRh(CO)_2$, and $Fe(CO)_5$. The activation of the Si–H bond by $CpCo(CO)_2$, $CpRh(CO)_2$, and $Fe(CO)_5$ in triethylsilane has been studied. The results are summarized in Scheme 4.2 and are discussed individually below.

Shown in Fig. 4.2 are the fs–IR spectra of $CpCo(CO)_2$ in neat Et_3SiH following excitation at 325 nm. At early times the photoproduct peak at 1990 cm^{-1} appears 5 cm^{-1} red shifted with respect to that of the Si–H bond activated product at 1995 cm^{-1}. The 1990 cm^{-1} peak appears to completely decay while the Si–H bond activated product peak at 1995 cm^{-1} exhibits a rise time of 22 ± 5 ps, as shown in Fig. 4.2. It is difficult to determine whether these dynamics are due to cooling of the Si–H bond activated product or the reaction of the nascent photoproduct with the solvent

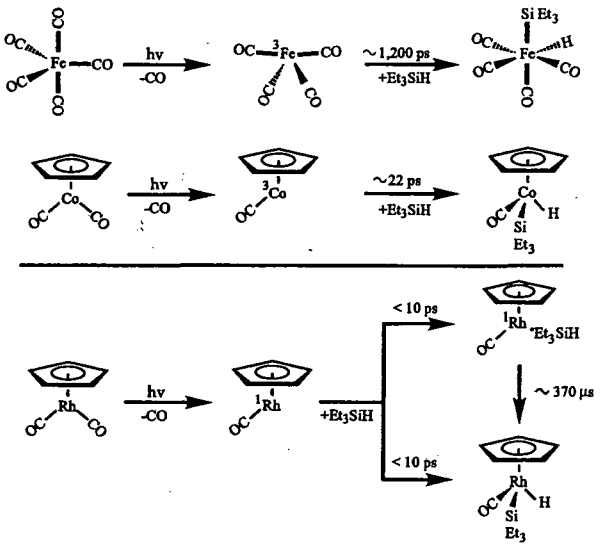

Scheme 4.2. The dynamics of high spin intermediates in triethylsilane solution.

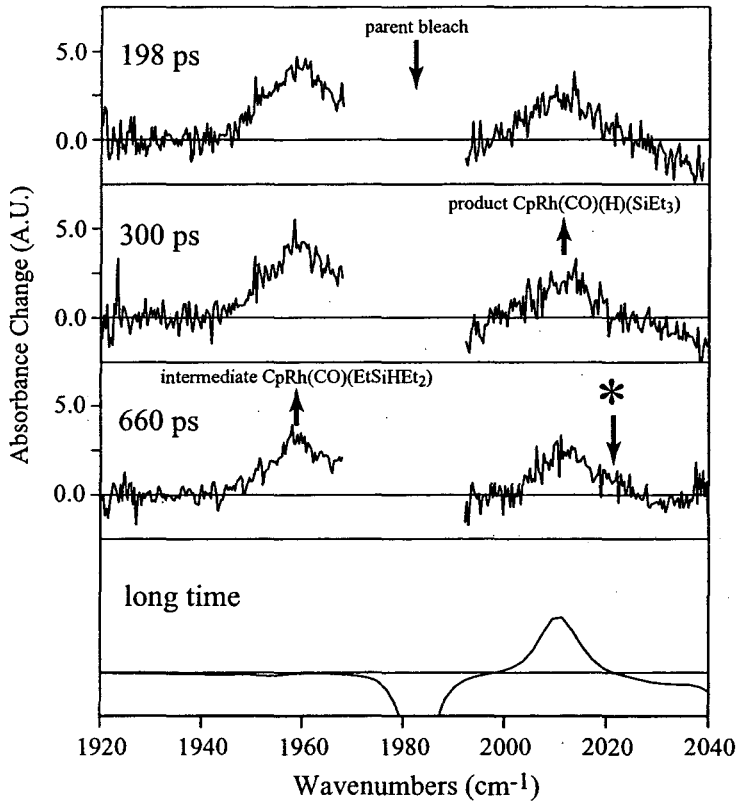

Figure 4.3 The difference spectra and kinetics of $CpRh(CO)_2$ following photolysis in triethylsilane. The possible C–H activated species absorbing at 2020 cm^{-1} is labeled.

(*vide infra*). The long time spectrum of the bond activated product $CpCo(CO)(H)(SiEt_3)$ is shown in the last panel in Fig. 4.2. The similarity of this long time spectrum with the 50 ps spectrum indicates that the formation of this product occurs on the ultrafast timescale.

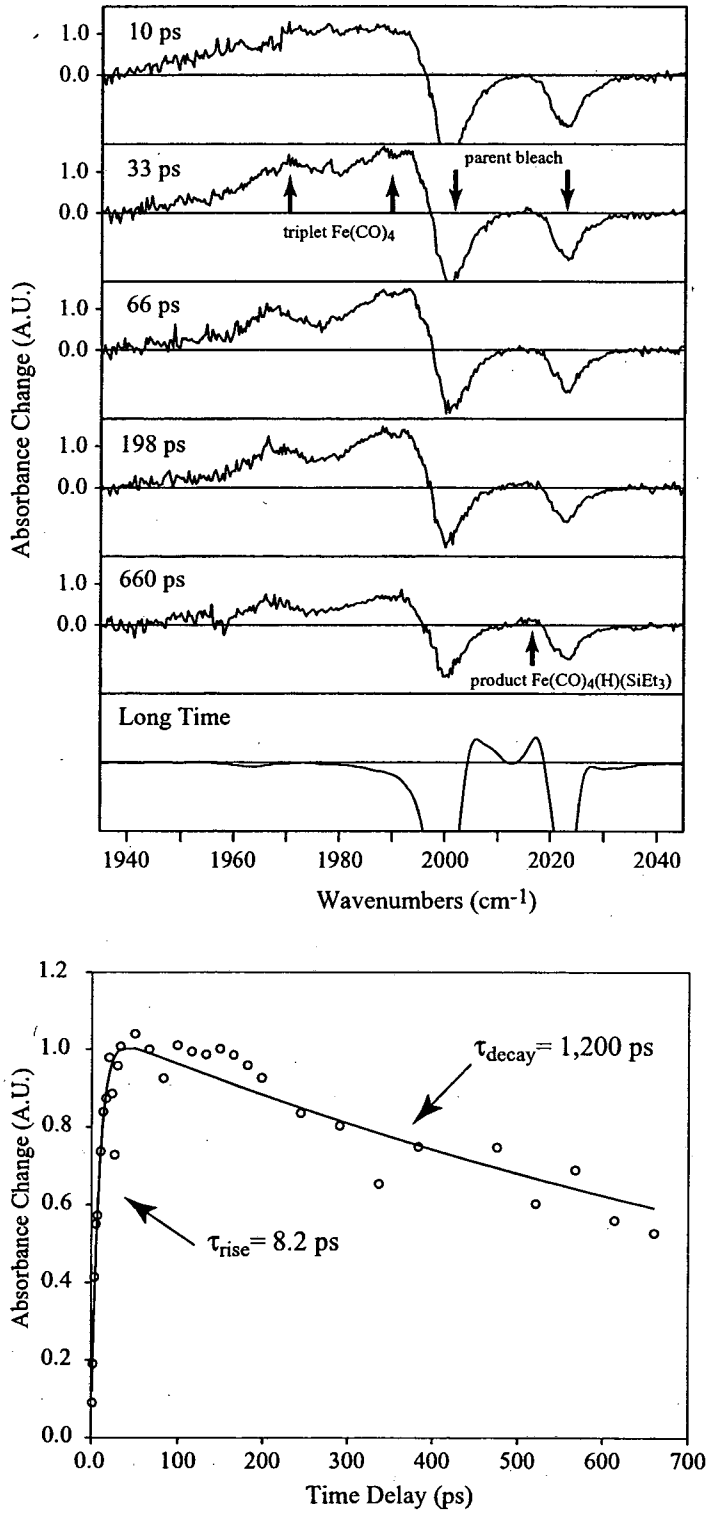

Figure 4.4 The difference spectra and kinetics of $Fe(CO)_5$ following photolysis in triethylsilane.

In order to develop a greater understanding of the reactivity of these photogenerated species, the $CpCo(CO)_2$ results are compared to studies of isoelectronic $CpRh(CO)_2$ in triethylsilane. In Fig. 4.3 are the fs–IR difference spectra of $CpRh(CO)_2$ in triethylsilane following excitation at 295nm. At 10 ps a photoproduct peak at 1960 cm^{-1} and Si–H activated product band at 2011 cm^{-1} are overlapped with hot bands from the parent, however the dynamics of this system appear relatively static from 200 to 660 ps. The long time spectrum of the bond activated product $CpRh(CO)(H)(SiEt_3)$ is shown in the last panel in Fig. 4.3; note the absence of the ethyl–solvated intermediate species peak at 1960 cm^{-1}.

The ultrafast spectra from the 295 nm photolysis of $Fe(CO)_5$ in triethylsilane solution are presented in Fig. 4.4. After excitation, a single new photoproduct absorbing at 1967 cm^{-1} and what appear to be two highly overlapped bands centered around 1990 cm^{-1} is formed. The kinetic trace of this species exhibits a rise time of 8 ± 1 ps and then decays on a 1,200 ± 200 ps timescale. The cooling of the initially hot photoproduct is responsible for the rise while the decay of this species and the formation of a small peak at 2016 cm^{-1} is most likely due the formation of the Si–H bond activated product. The spectra of the bond activated product $Fe(CO)_4(H)(SiEt_3)$ is shown in the last (long time) spectrum in Fig. 4.4.

Section 4.3 Discussion

The experimental and theoretical results of the present and past investigations establish that the solution phase dynamics upon photolysis of $CpCo(CO)_2$ and $Fe(CO)_5$ are due to the exclusive formation of triplet intermediates. In triethylsilane, these triplet intermediates form the Si–H bond activated product on the ultrafast timescale while the photogenerated singlet CpRh(CO) species' reactivity is overall much slower. A change

in the Si–H bond activation mechanism between the triplet and singlet is responsible for these observations.

A. Liquid Phase Photolysis of $CpCo(CO)_2$, $Fe(CO)_5$, $CpMn(CO)_3$. The Dynamics of Triplet Intermediates. The ultrafast photochemistry of CpCo(CO) in alkane solution was studied by Dougherty et. al.[62] Our results are consistent with their report; an intermediate peak appears at 1990 cm^{-1} and does not decay within 660 ps, the maximum pump–probe time delay of our experimental apparatus. This intermediate is most likely triplet CpCo(CO), as the trends seen in the DFT frequency analyses presented in Table 4.4 support the spectral assignment and the DFT and pt2–casscf results predict large triplet–singlet energy splittings favoring the triplet ground state. As Bengali et. al. showed, this species does not interact with alkanes, which is also consistent with the formation of a triplet intermediate.[34]

While this species is stable in heptane, triplet CpCo(CO) is overall the most reactive of all (triplet or singlet) species under study in triethylsilane. In triethylsilane, a peak at 1990 cm^{-1} appears at early times and decays with the concomitant formation of a new product peak at 1995 cm^{-1} in 22 ps. Compared to the long time spectrum in Fig. 4.2, the 1995 cm^{-1} peak is due to the bond activated product $CpCo(CO)(H)(SiEt_3)$. It is unclear whether the decay of peak at 1990 cm^{-1} is due to cooling of a bond activated product hot band or the reaction of the triplet species with the triethylsilane solvent, however the 1990 cm^{-1} peak is most likely the nascent triplet species as this peak position coincides with the triplet photoproduct in heptane. Regardless, the reactivity of triplet CpCo(CO) in triethylsilane is very fast with the Si–H bond activated product appearing at a rate of $k > 4.5 \times 10^{10}\ s^{-1}$. A similar fast reactivity was also observed by Dougherty

et. al. for CpCo(CO) in 1–hexene.[62] These results are summarized in Schemes 4.1 and 4.2.

In dry heptane, the photochemistry of $Fe(CO)_5$ appears very similar to that of $CpCo(CO)_2$. Instantaneous parent bleaches are accompanied by the formation of a single new photoproduct absorbing at 1965 cm^{-1} and overlapping bands centered at 1987 cm^{-1}, which does not decay within the maximum pump–probe time delay of 660 ps. This photoproduct is most likely triplet $Fe(CO)_4$ as the DFT and ab initio calculations predict a triplet ground state and the experimental photoproduct frequencies are similar to those of the triplet species seen in matrix experiments.[63,64] The $Fe(CO)_4$ intermediate has been shown to have weak interactions with alkanes,[65] which is also consistent with the formation of a triplet species. Consequently, triplet $Fe(CO)_4$ is the only intermediate formed under the experimental conditions. In triethylsilane, the same triplet photoproduct appears at 1967 and 1990 cm^{-1}. The reaction timescale in neat triethylsilane is approximately 1,200 ± 200 ps, based upon the decay kinetics of the initially formed triplet species and the coincident formation of the Si–H activated product. The $Fe(CO)_4$ reaction rate of $k=8.3\times 10^8\ s^{-1}$ with triethylsilane is the slowest of the triplet species under investigation. These results are also summarized in Schemes 4.1 and 4.2.

The formation and the decay of the photoproducts of $CpMn(CO)_3$ in alkane solution were studied in order to compare the results to the triethylsilane studies. In contrast to the long–time stability of the triplet intermediates of $CpV(CO)_3$, $Fe(CO)_4$ and CpCo(CO) in alkane solution, the triplet kinetics of $CpMn(CO)_2$ show a 119 ps decay with a corresponding increase in the singlet alkyl–solvate. The difference is likely due to the large spin–orbit coupling of $CpMn(CO)_3$, the relatively low triplet / singlet energy

gap as well as the calculated stabilizing interaction enthalpy of the singlet manganese alkyl solvate compared to the other species. These results and conclusions are presented in more detail in Section. 4.4.

The results for these triplet species may be summarized as follows. Upon photolysis of $CpCo(CO)_2$ and $Fe(CO)_5$ in solution, a single carbonyl is lost and the photoproducts are in the unsolvated ground triplet state. These species are stable in alkane solution yet react in triethylsilane solution on the ultrafast timescale. These results are similar to the previous results for triplet $CpV(CO)_3$ and $CpMn(CO)_2$, although triplet $CpMn(CO)_2$ is unstable in alkane as well as in triethylsilane solution.

B. Liquid Phase Photolysis $CpRh(CO)_2$. The Dynamics of a Singlet Intermediate. The situation is very different for the photochemistry of $CpRh(CO)_2$. It has been established that CpRh(CO) has a singlet ground state,[43,66] and that singlet organometallic species have greater interactions with alkanes than triplet species.[32,43,67–69] In triethylsilane solution, previous results have shown that singlet intermediates may coordinate to the ethyl moiety of triethylsilane, which form long lived intermediates.[2,25,30] This ethyl solvate does not form the final Si–H bond activated product until this complex has dissociated.[25]

As seen in Fig. 4.3, the dynamics of the photoproduct CpRh(CO) absorbing at 1960 cm^{-1} and 2011 cm^{-1} appear to remain relatively constant from 200 ps to 660 ps. The species at 1960 cm^{-1} can be assigned to the triethylsilane ethyl solvated moiety of singlet CpRh(CO), and the 2011 cm^{-1} peak corresponds to the Si–H bond activated product as seen in the long time spectrum of Fig. 4.6. The timescale for the final formation of the Si–H activated product is very long as the overall first order bond activation rate was extrapolated to be $k=2.7 \times 10^3\ s^{-1}$ in the concentration dependent

study of Belt et. al.[53] From the slight peak that appears at 2020 cm^{-1} and the small decay in the ethyl solvated peak in the ultrafast spectrum, there exists a possibility that a C–H bond of the ethyl moiety is being activated. This possibility was confirmed in our experiments with $CpRh(CO)_2$ in pentane and hexane, the results of which are presented in Chapter 6. This also explains why the overall reaction of CpRh(CO) with triethylsilane is very slow compared to similar organometallic species. Unfortunately, the low signal due to the 25% quantum yield of $CpRh(CO)_2$ makes a detailed kinetic analysis of the initial formation of the Si–H activated product impractical with the present femtosecond apparatus.

These experimental results can be summarized as follows. The monocarbonyl photoproduct of $CpRh(CO)_2$ in triethylsilane is a singlet, forming a ethyl moiety solvated species and the Si–H bond activated product via initial solvation with the ethyl group or Si–H bond within 10 ps. The ethyl solvated singlet activates a C–H bond, forming a long lived intermediate which rearranges to the the final bond activated product on a timescale several orders of magnitude longer than for $Fe(CO)_4$ and CpCo(CO) triplet species. These results are similar to our previous studies of triplet / singlet $CpV(CO)_3$ and $CpMn(CO)_2$ in triethylsilane, in which it was shown that the triplet species decays faster than the ethyl–solvated singlet to form the final bond activated product.

C. The Reaction Mechanisms. In triethylsilane solution, coordinatively unsaturated singlet intermediates may form the Si–H bond activated product via Si–H solvation on the ultrafast timescale, however the singlet species also becomes trapped in an ethyl moiety solvated state. The singlet ethyl–solvate does not form the final bond activated product until the ethyl–solvated organometallic has dissociated.[25] As the experimental and theoretical results have established that triplet coordinatively

unsaturated intermediates do not interact with alkanes, they do not coordinate with the ethyl moiety of triethylsilane and are thus free to form the final Si–H bond–activated product along a much faster timescale. The same argument was put forth by Poliakoff in comparing the reactivity of $^3Fe(CO)_4$ versus $^1Cr(CO)_5$ towards various ligands,[54] and by Siegbahn to explain the differences observed in the reactivity of CpRh(CO) and CpCo(CO) with CO in alkane solution.[43] As previously proposed, the triplet reactivity can be attributed to a solvation / spin crossover by the strong coupling site of the reactant.[2,30]

While the overall mechanism of triplet coordinatively unsaturated intermediates has been elucidated in these experiments, the factors that govern the rate at which these species react can not be determined from the experimental results alone. The next section describes our efforts using theoretical models to predict triplet state reactivity. Overall the results have shown that a combination of spin–orbit coupling strengths and classical barrier heights are the governing factors in high spin reaction dynamics.

Section 4.4 Quantum Chemical Modeling.

A. Methods. In order to compare single point energies consistently, all calculations were carried out using DFT optimized geometries. The hybrid B3LYP functional was used for the DFT calculations with the Jaguar package.[7,10,11] This functional has been shown to give very good results for transition metal complexes.[70,71] The basis set consisted of the 6–31G** basis functions for H, C, O and Si,[40,41] and the Los Alamos Effective Core Potential (ECP) for V, Mn, Fe, Co and Rh with the outermost core orbitals included in the valence description.[42] All

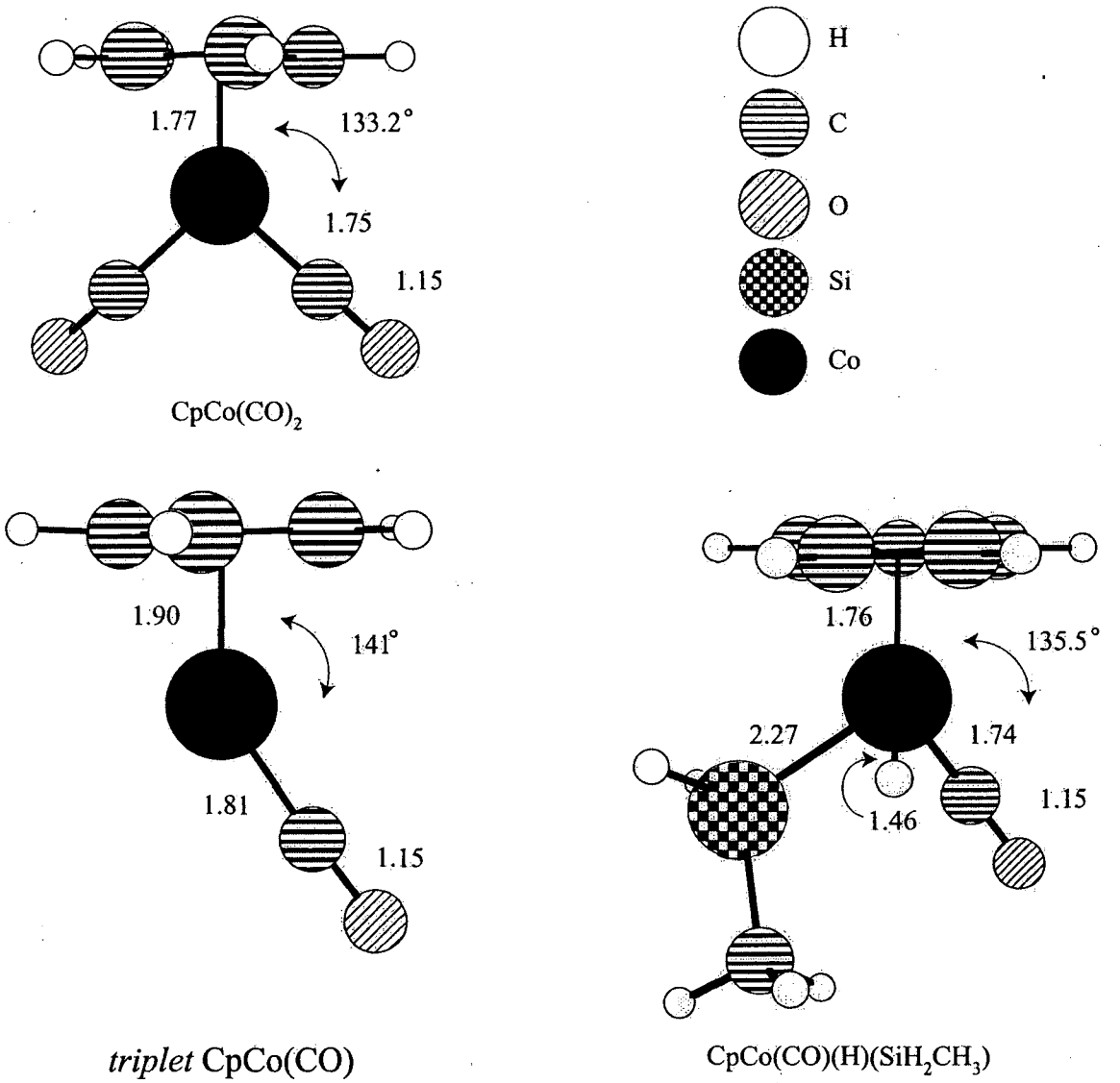

Figure 4.5. The DFT geometries for the parent, product and intermediate species observed in the $CpCo(CO)_2$ study.

geometry optimizations were followed by a frequency analysis to make certain that the optimized geometries were at a minimum.

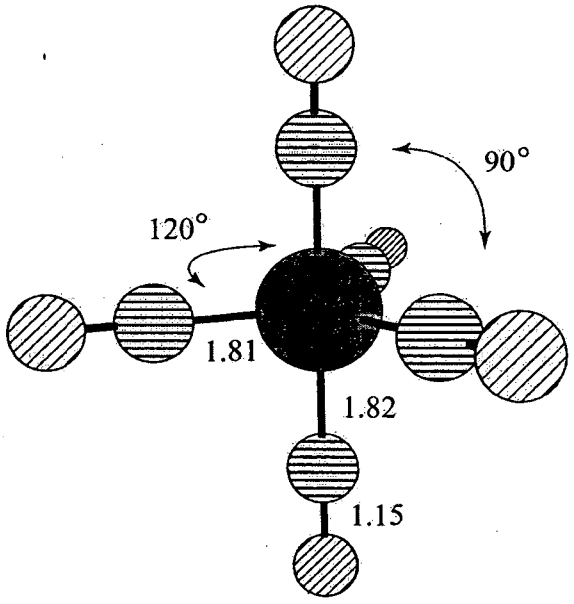

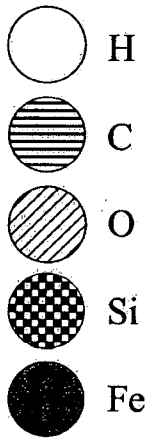

$Fe(CO)_5$

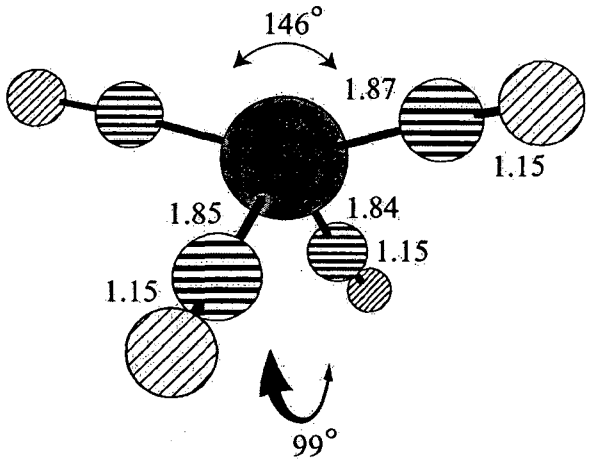

triplet $Fe(CO)_4$

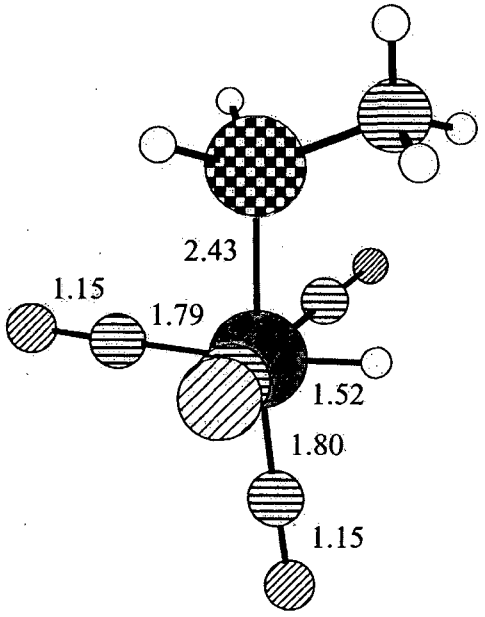

$Fe(CO)_4(H)(SiH_2CH_3)$

Figure 4.6. The DFT geometries for the parent, product and intermediate species observed in the $Fe(CO)_5$ study.

In order to determine the ground spin state of all the intermediate species under study, second order perturbation theory calculations of the complete active space multiconfigurational self–consistent field wavefunction (pt2–mcscf) were performed for the singlet and triplet species. These *ab initio* calculations were carried out using the GAMESS–US package,[9,44] using the lanl2dz basis set.[42,45–47] The active space of the casscf calculations consisted of 10 occupied and unoccupied d–type orbitals while the perturbative calculations excluded only the core electrons. The coupling (spin–orbit) strength was calculated at the ground state triplet geometry using the method of corresponding orbitals.[72] As it is computationally unfeasible to calculate the full Breit–Pauli spin–orbit Hamiltonian for the optimized mcscf wavefunction, the two electron component of the operator is removed and an approximate metal charge (Z_{eff}) is used. The Z_{eff} at the metal center described by Koseki et. al. was used to calculate the spin–orbit coupling, again using the lanl2dz basis set.[73]

For computational efficiency, the neat alkane (or ethyl moiety of triethylsilane) interaction and Si–H interaction with the singlet / triplet organometallic complexes was modeled using C_2H_6 or SiH_3CH_3, respectively. The binding strengths of the singlet species were also calculated at the MP2 level of theory using the counterpoise method to account for basis set superposition error including DFT / B3LYP zero point energy corrections.[74,75]

In order to describe the trends seen in the reactivity of the triplet species $CpV(CO)_3$, $Fe(CO)_4$, and CpCo(CO) in triethylsilane, the DFT potential energy curves for these organometallic species with SiH_3CH_3 were calculated by fixing the metal–Si bond lengths (R) of the organometallic complexes and subsequently optimizing the remaining geometric parameters. This was done for both singlet and triplet

compound	Cp–M	M–CO	C–O	M–H	M–Si (C)	Si–H	α[c]
$Fe(CO)_5$		1.81, 1.82 [1.81, 1.83][a]	1.15, 1.15 [1.15,1.15][a]				120°, 90°
$^1Fe(CO)_4$		1.78,1.81	1.15				157°, 131°
$^3Fe(CO)_4$		1.84, 1.86	1.15				146°, 99° [147°, 120°][d]
$Fe(CO)_4(H)(SiH_2CH_3)$		1.79, 1.80	1.15	1.52	2.43	2.77	98°, 99°
$CpCo(CO)_2$	1.77	1.75 [1.68][b]	1.15 [1.19][b]				95° [98°][b]
$^1CpCo(CO)$	1.75	1.75	1.16				138°
$^3CpCo(CO)$	1.90	1.81	1.15				141°
$CpCo(CO)(H)(SiH_2CH_3)$	1.76	1.74	1.15	1.46	2.27	2.25	136°

a. Numbers in brackets are experimental values from ref. 82. Parameters for the equatorial CO are given first.
b. Numbers in brackets are experimental values from ref. 83.
c. The (CO)–M–(CO) angle. For CpCo(CO)X species, the (CO)–Co–(Cp center) bond angle.
d. From ref. 21, Ar matrix results.

Table 4.1. The optimized geometric parameters for the iron and cobalt organometallic systems. All lengths are in Å and angles are in degrees.

organometallic fragments at various values of R near the singlet–triplet crossing region. This type of analysis builds an approximate potential energy surface for the bond activation reaction as a function of the metal–Si distance, although the actual activation coordinate is more complex due to the high dimensionality of the dynamics.

B. Geometry optimizations. The geometries of the parent molecules $CpCo(CO)_2$ and $Fe(CO)_5$, the intermediate triplet species, and the final model Si–H activated products are shown in Fig. 4.5 and Fig. 4.6. The relevant geometric parameters

are summarized in Table 4.1. The M–CO distances are longer and the CO bond lengths are shorter in the triplet species compared to the singlet, which is a general trend seen in several previous calculations. Triplet $Fe(CO)_4$ has C_{2v} symmetry, as confirmed in matrix isolation experiments.[54,63] The theoretical results predict CO–M–CO bond angles of 146° and 99°, which are in fair agreement with the previous experimental results of 147° and 120° of triplet $Fe(CO)_4$ in Ar matrix. The $Fe(CO)_4$ results are also in good agreement with previous gas–phase theoretical calculations.[76,77] The calculated singlet and triplet CpCo(CO) geometries are also very similar to those of Siegbahn.[43] The large increase of the Si–H distances (~0.76 Å for $CpCo(CO)(H)(SiH_2CH_3)$ and ~1.28 Å for $Fe(CO)_4(H)(SiH_2CH_3)$) in the bond activated products' optimized geometry indicate that the Si–H bond is almost totally broken in these species.

C. Energy calculations. While the absolute thermochemical errors of this theoretical model are on the order of ~5 kcal/mol,[71] all the computational results are presented as relative energies, which represent a more meaningful quantity in comparative situations. The calculated singlet metal–ligand interaction energies are listed in Table 4.2. All binding energies have been calculated at the MP2 level of theory using the DFT geometries. The calculated binding energies of ethane qualitatively demonstrate the stability of the singlet metal–alkane interaction and allow for a comparison between the different organometallics. The calculated binding strengths for various other ligands are also presented.

The results of the DFT and pt2–casscf calculations for the singlet and the triplet species are shown in Table 4.3. The DFT and pt2–casscf results predict a lower energy for the triplet state relative to that of the singlet for $CpV(CO)_3$, $CpMn(CO)_2$, $Fe(CO)_4$ and CpCo(CO). While the pt2–casscf calculation predicts a slightly more stable triplet

Fragment	Ligand	ΔE (kcal/mol)
$CpV(CO)_3$	CO	42.1[a]
$CpMn(CO)_2$		64.6
$Fe(CO)_4$		67.3 (ax), 52.2 (eq)
CpCo(CO)		60.8
CpRh(CO)		51.0
$CpV(CO)_3$	C_2H_6	3.55[a]
$CpMn(CO)_2$		7.71
$Fe(CO)_4$		6.93
CpCo(CO)		12.3
CpRh(CO)		9.18[b]
$CpV(CO)_3$	SiH_2CH_3	16.0
$CpMn(CO)_2$		54.2
$Fe(CO)_4$		90.9
CpCo(CO)		115
CpRh(CO)		162

a. From ref. 28.
b. The non–activated complex.

Table 4.2. The binding strengths of various organometallic fragment species with CO, C_2H_3 and SiH_3CH_3 model ligands. All energies are in kcal/mol.

CpRh(CO), DFT calculation shows that singlet CpRh(CO) is energetically more favorable. Experimental evidence, such as the C–H bond activation ability of CpRh(CO), also suggests that this species has a singlet ground state.

In order to understand the reactivity of these triplet species, the metal–Si coordinate potential energy curves were calculated at the DFT level of theory. The results are shown in Fig. 4.7 and are summarized in Table 4.5. The triplet / singlet $Fe(CO)_4$ and $CpV(CO)_3$ crossover points occur at metal–Si distances of 3.85 and 4.34 Å, respectively. The iron complex crossover is 1.73 kcal/mol above the (unsolvated) triplet

(ground state)–organometallic	ΔE^a (DFT) kcal/mol	ΔE^a (pt2–casscf) kcal/mol	vert.–ΔE^b (pt2–casscf) kcal/mol
(triplet)–$CpV(CO)_3$	3.10[c]	22.3	28.4
(triplet)–$CpMn(CO)_2$	4.69	10.4	27.5
(triplet)–$Fe(CO)_4$	5.43	6.29	19.5
(triplet)–CpCo(CO)	25.9	20.5	23.3
(singlet)–CpRh(CO)	−0.38	3.11	4.49

a. Calculated as E(ground spin state)–E(excited spin state).
b. The ΔE between the ground and excited spin state at the ground state geometry.
c. From ref. 2.

Table 4.3. The energetic splitting between singlet and triplet states at various levels of theory.

ground state while the vanadium barrier is 1.56 kcal/mol. The CpCo(CO) / model silane calculation results show that this triplet species has a slight attractive interaction with the model silane solvent. The −0.71 kcal/mol well of this interaction occurs at a metal–Si distance of 3.2 Å. The singlet / triplet crossover occurs at a metal–Si distance at 2.5 Å at 0.73 kcal/mol above the (unsolvated) triplet ground state. Spin–orbit coupling (SOC) calculations at the ground state triplet geometry were also performed using the optimized multiconfigurational wavefunction and are summarized in Table 4.5. Overall, the coupling constant is much greater for the vanadium, manganese and cobalt complexes than that of the iron system.

D. Understanding the Trends of Triplet Reactivity. It has been shown that the iron, cobalt and vanadium organometallic complexes form stable triplet intermediates in alkane yet decay on the ultrafast timescale in triethylsilane. The trend of the reactivity in triethylsilane from Table 4.5 is CpCo(CO) > $CpV(CO)_3$ > $Fe(CO)_4$. These experimental

complex	Observed frequency (cm^{-1})	DFT frequency[a] (cm^{-1})	Reference
$Fe(CO)_5$	2023, 2000 heptane	2124, 2100	2024, 2004 C_6D_6 [78]
$^3Fe(CO)_4$	1987, 1965 heptane	2102, 2093	1993/2, 1985,1967 CH_4 matrix [54]
$Fe(CO)_4(H)(SiEt_3)$	2091, 2017, 2006 heptane[b]	2171, 2131 2126, 2112	2093, 2028, 2018, 2007 hexane[c] [79]
$CpCo(CO)_2$	2031, 1971 heptane	2124, 2085	2031, 1971 n–hexane [61]
$^3CpCo(CO)$	1990 heptane	2121	1993 n–hexane [61]
$CpCo(CO)(H)(SiEt_3)$	1995 triethylsilane	2105	this work
$CpRh(CO)_2$	2047,1984 triethylsilane	2129, 2077	2048, 1985 cyclohexane [80]
$^1CpRh(CO)(EtSiHEt_2)$	1960 triethylsilane	2059	1963[d] cyclohexane [80]
$CpRh(CO)(H)(SiEt_3)$	2011 triethylsilane	2101	2010 n–pentane [77]

a. Data are for the model compounds and are necessarily gas phase data. The DFT calculated frequencies are generally known to be blue–shifted from the experimental values, see ref. 81.
b. A fourth peak is likely overlapped with the 2023 cm^{-1} $Fe(CO)_5$ parent bleach.
c. The spectral data are for $Fe(CO)_4(H)(SiMe_3)$.
d. The spectral data are for CpRh(CO)(cyclohexane).

Table 4.4. Summary of the observed vibrational frequencies, DFT result, and literature references in brackets.

results may be interpreted in terms of two factors: the barrier at the singlet / triplet curve crossover and the calculated coupling of the singlet and triplet surfaces.

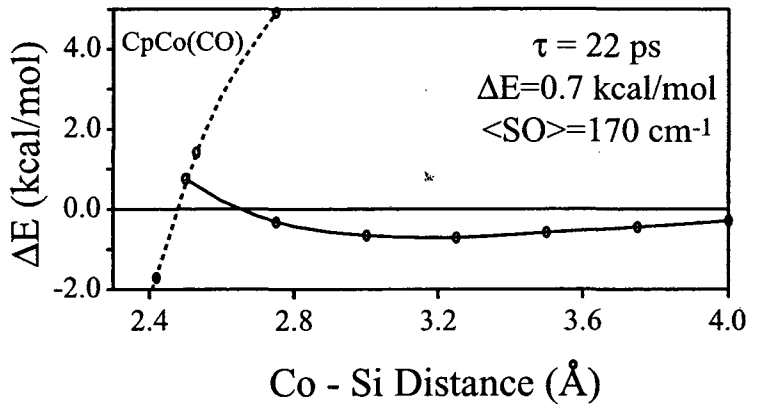

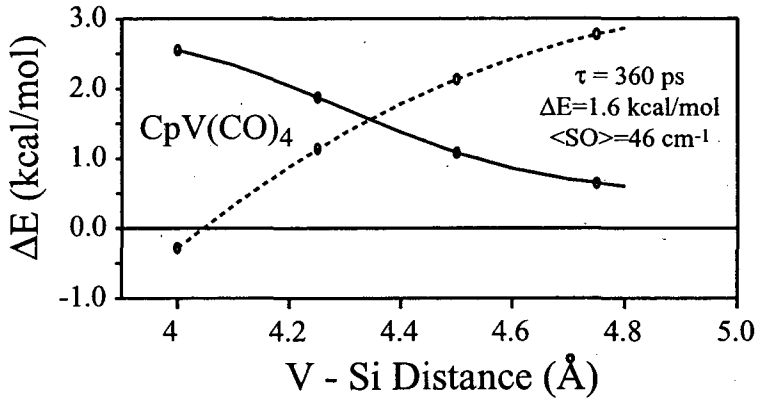

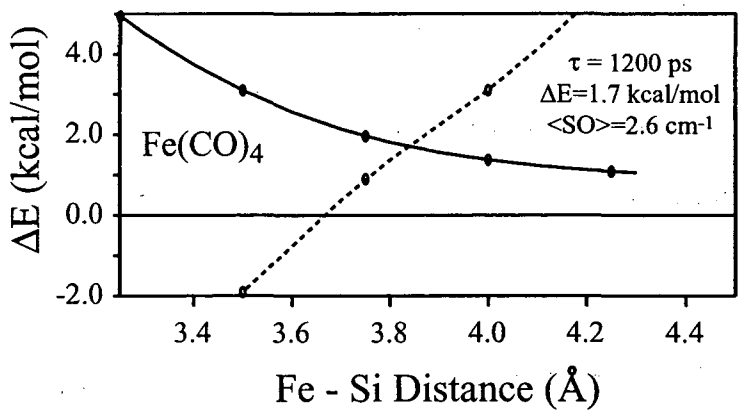

Figure 4.7 The results for the metal–Si potential energy surfaces for singlet and triplet organometallic species with SiH_3CH_3

complex / SiH_3CH_3	minimum (Å)	interaction E (kcal/mol)	singlet/ triplet crossover (Å)	Barrier (kcal/mol)	SOC (cm^{-1})	τ (silane) (ps)
CpCo(CO)	3.2	−0.71	2.5	0.73	170	22
$CpV(CO)_3$	–	–	4.3	1.56	46.2	340
$Fe(CO)_4$	–	–	3.9	1.73	2.55	1200
$CpMn(CO)_2$[a]	–	–	–	–	232	105[b]

a. The potential curves for singlet and triplet $CpMn(CO)_2$ / SiH_3CH_3 were not calculated as this species is unstable in alkane as well as in triethylsilane solution.
b. From ref. 2.

Table 4.5. The results of the DFT potential energy curve calculations. The potential minimum data are reported for triplet CpCo(CO) / SiH_3CH_3. The singlet / triplet spin–orbit constants and the triplet species lifetimes in triethylsilane solution are also summarized.

The trends in the reactivity of these species may be understood in terms of the approximate nonadiabatic potential energy surfaces generated by the DFT singlet and triplet organometallic / model silane calculations in Fig. 4.7. The singlet state (dashed) curves for all the species slopes downhill with decreasing M–Si distance, which shows that the singlet Si–H bond activated product is overall the most favorable species energetically. The triplet (solid) curves, however, show that the triplet species' interaction with SiH_3CH_3 is generally unfavorable. These theoretical calculations elucidate the fast reactivity of triplet CpCo(CO) in triethylsilane. In this system, there exists a small classical barrier at the singlet / triplet crossover due to what appears to be a small attractive interaction between the triplet cobalt species and the model silane solvent. The triplet species metal–Si minimum is less than 1 Å from the singlet activated product bond length, which indicates that only a slight rearrangement is necessary to

form the product. At the triplet minimum, the spin–orbit calculation shows a strong coupling between the triplet and singlet surfaces. This result is important as the spin–orbit coupling is responsible for intersystem crossing. Consequently, the low classical barrier as well as the large coupling between states explains why such a fast ($k=4.5 \times 10^{10}$ s^{-1}) reaction occurs between triplet CpCo(CO) and the Si–H bond. There does not appear to be an attractive interaction of triplet $Fe(CO)_4$ and triplet $CpV(CO)_3$ with SiH_3CH_3, which results in a larger classical barrier at greater crossing point distances than seen in triplet CpCo(CO). The reactivity of these species may be understood in two limiting regimes. The vanadium triplet species has a significant singlet / triplet coupling, however this species also has a larger classical barrier to activation than the cobalt complex. The $Fe(CO)_4$ intermediate, which reacts with triethylsilane at the slowest rate of all the triplets species, has a similar activation barrier to that of $CpV(CO)_3$ yet has a very small coupling between the spin states. We can conclude that knowledge of the spin–orbit strengths as well as the potential energy surfaces are necessary in understanding the reactivity of these species.

Section 4.5 Conclusion

We have shown in this paper that the photochemical reaction dynamics of $Fe(CO)_5$ and $CpCo(CO)_2$ are due to the formation of triplet state intermediates. The results are in contrast to the singlet intermediate dynamics seen with $CpRh(CO)_2$. Due to a change in the reaction mechanism, the overall reactivity of the triplet species is much greater than that of similar singlet species.

A general mechanism explaining the reactivity of triplet organometallics may now be proposed. Coordinatively unsaturated singlet organometallics will tend to associate to most solvents, even alkanes. These interactions will likely hinder further

reactivity with a stronger coupling site as these alkyl solvated species may exist for milliseconds in solution. The triplet species are free to react at a faster rate as they do not coordinate to the same degree with a weak coupling alkyl site. The timescale of the triplet metal complex reactivity can be understood in terms of spin–orbit coupling between the singlet and triplet surfaces as well as the classical barrier to bond activation. This mechanistic change explains the differing reactivity of triplet and singlet coordinatively unsaturated organometallic complexes in triethylsilane, and can likely be extended to other chemical systems.

Chapter 5

The Photochemical Reaction Dynamics of $Fe(CO)_5$

Section 5.1 Introduction

Our previous studies of triplet intermediates have established that high spin species do not have significant interactions with the alkyl groups of a solvent molecule. As such, studying the photochemistry of triplet species provides a unique opportunity to investigate the effects of solvent viscosity on the reaction rates of coordinatively unsaturated organometallic intermediates. This cannot be accomplished using a singlet unsaturated species, which have very complex interactions with solvents due to their ability to coordinate with alkyl groups. Establishing a firm connection between solvent viscosity and reaction rate for coordinatively unsaturated singlet species is thus very difficult due to these complex interactions, as the rate is also influenced by several factors such as the number of alkyl binding sites as well as the known alkyl chain–length dependence of the binding energy.[23,85,86] Triplet intermediates, however, will only react with the strong coupling site of a solvent molecule. As such, the primary influences of the reaction rate of a high spin intermediate ought to be attributed to the viscosity of the reactive media under the assumption that the spin–orbit coupling does not significantly change in similar solvents. Our group has measured the reaction rate of the spin solvation / crossover reaction of triplet $Fe(CO)_4$ in a series of long chain alcohol solvents in order to address the issue of solvent viscosity in unsaturated organometallic reactivity.

A description of the photochemistry of $Fe(CO)_5$ would not be complete without some discussion of the unusual two carbonyl loss photosubstitution reaction of this compound with trisubstituted phosphines. The observation of double CO substitution via a one photon process conflicts with the conventional belief that only a single carbonyl is lost from an organometallic species following photoexcitation in solution. First observed by Lewis et. al.,[87] this reaction was characterized by Nayak and Burkey in a series of elegant mechanistic experiments.[59,65] These authors proposed that the double CO loss dynamics were due to the formation of triplet $^3Fe(CO)_4$, although other researchers have proposed that the dynamics are due to a singlet species.[61] As we have recently confirmed that $^3Fe(CO)_4$ is formed on the ultrafast timescale in room temperature alkane solution, we have studied this system in neat triethylphosphine to develop a comprehensive mechanism for this unusual photosubstitution reaction. The reactivity of the photogenerated species is also described using DFT, which qualitatively reproduces the trends seen in the experimental data. The overall reactions under study are summarized in Scheme 5.1.

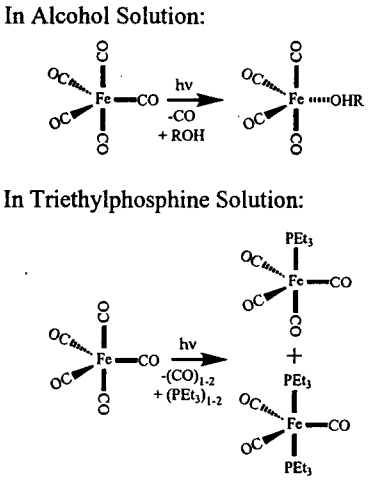

Scheme 5.1: The photochemical substitution reactions under study.

Section 5.2 Experimental Results

A. Photolysis of $Cr(CO)_6$ and $Fe(CO)_5$ in neat alcohol solution. The time–resolved spectra of $Fe(CO)_5$ in tert–butyl alcohol are shown in Figure 5.1 on page 65. At early times the spectra of the triplet species appear broad and highly overlapped with parent

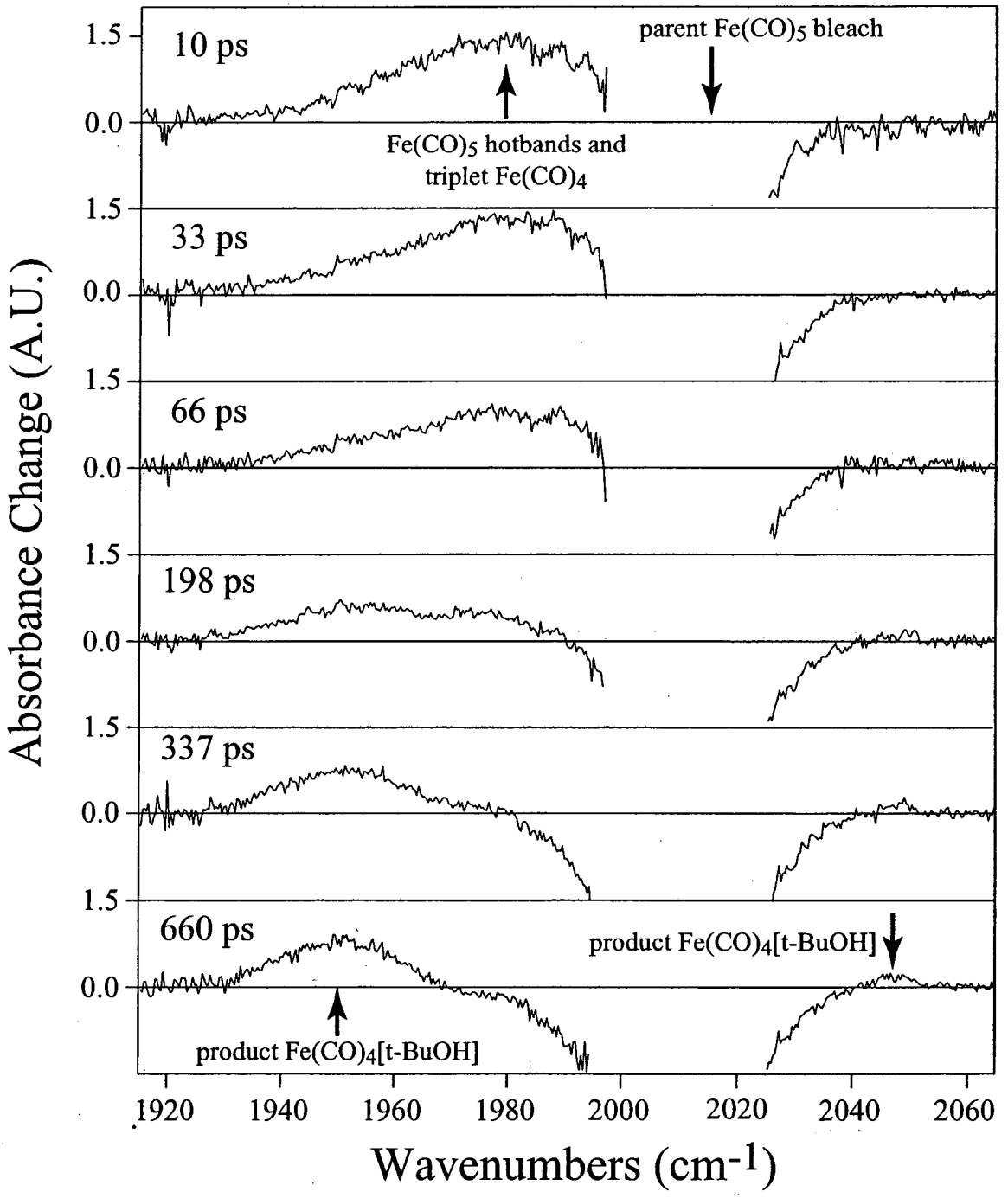

Figure 5.1. The ultrafast time resolved spectra resulting from the photolysis of $Fe(CO)_5$ in tert–butyl alcohol.

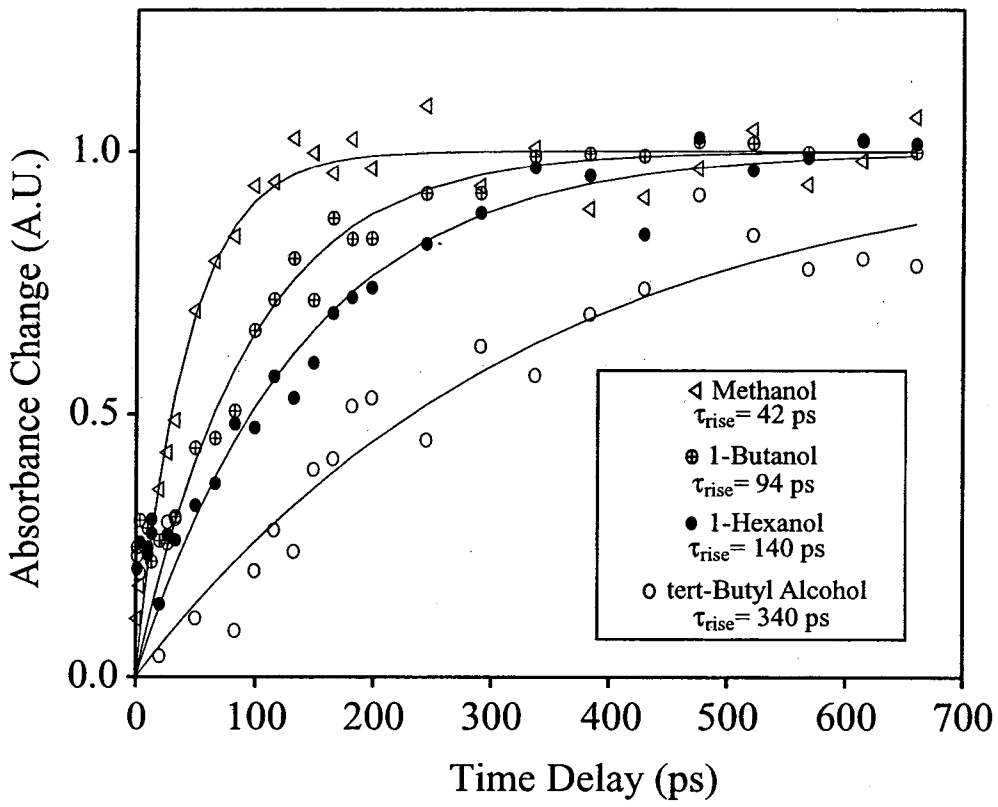

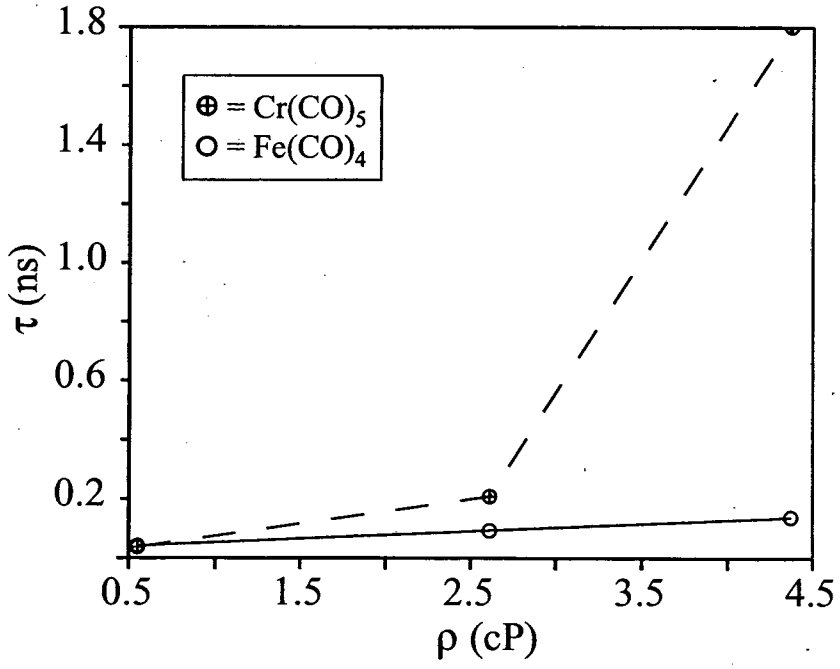

Figure 5.2. The ultrafast kinetics of $Fe(CO)_4$ in various alcohol solutions.

	methanol (ps)	n–butanol (ps)	n–hexanol (ps)	tert–butyl alcohol (ps)
Solvent viscosity[a]	0.55	2.61	4.37	5.88
τ, $^3Fe(CO)_4$	42.3[b]	93.7	138	335
τ, $^1Cr(CO)_5$	38[b]	209	1800	–

a. The viscosity in units of centipoise, from ref. 88.
b. In methanol, the alkyl solvated $Cr(CO)_5$ or high spin $Fe(CO)_4$ intermediates are not observed. Consequently, the kinetics are likely due to cooling of the final photoproduct which forms at a faster rate. In fact, Simon et al. observed a timescale of 2.5 ps for the formation of $Cr(CO)_5(HOCH_3)$ in their earlier visible wavelength study.[18]

Table 5.1. The timescales of formation of the OH–solvated singlet intermediate for the photochemical reaction of $Fe(CO)_5$ and $Cr(CO)_6$ in various alcohols. The $Fe(CO)_5$ results approximately scale with the solvent viscosity, see text.

hot bands. At later times the triplet species decays to form the singlet hydroxyl solvated $Fe(CO)_4(HOR)$ product with peak positions at 1950 and 2047 cm^{-1}. The spectra in other alcohol solvents are qualitatively similar. The kinetic traces of the formation of the singlet hydroxyl solvated products in all the alcohol solvents are shown in Fig. 5.2 and are summarized in Table 5.1. The solvent viscosities and timescales of rearrangement of singlet $^1Cr(CO)_5$ to form the hydroxyl solvated products in methanol, 1–butanol and 1–hexanol are also given in Table 5.1. Overall, the rearrangement timescales are much longer than those observed for the iron complexes.

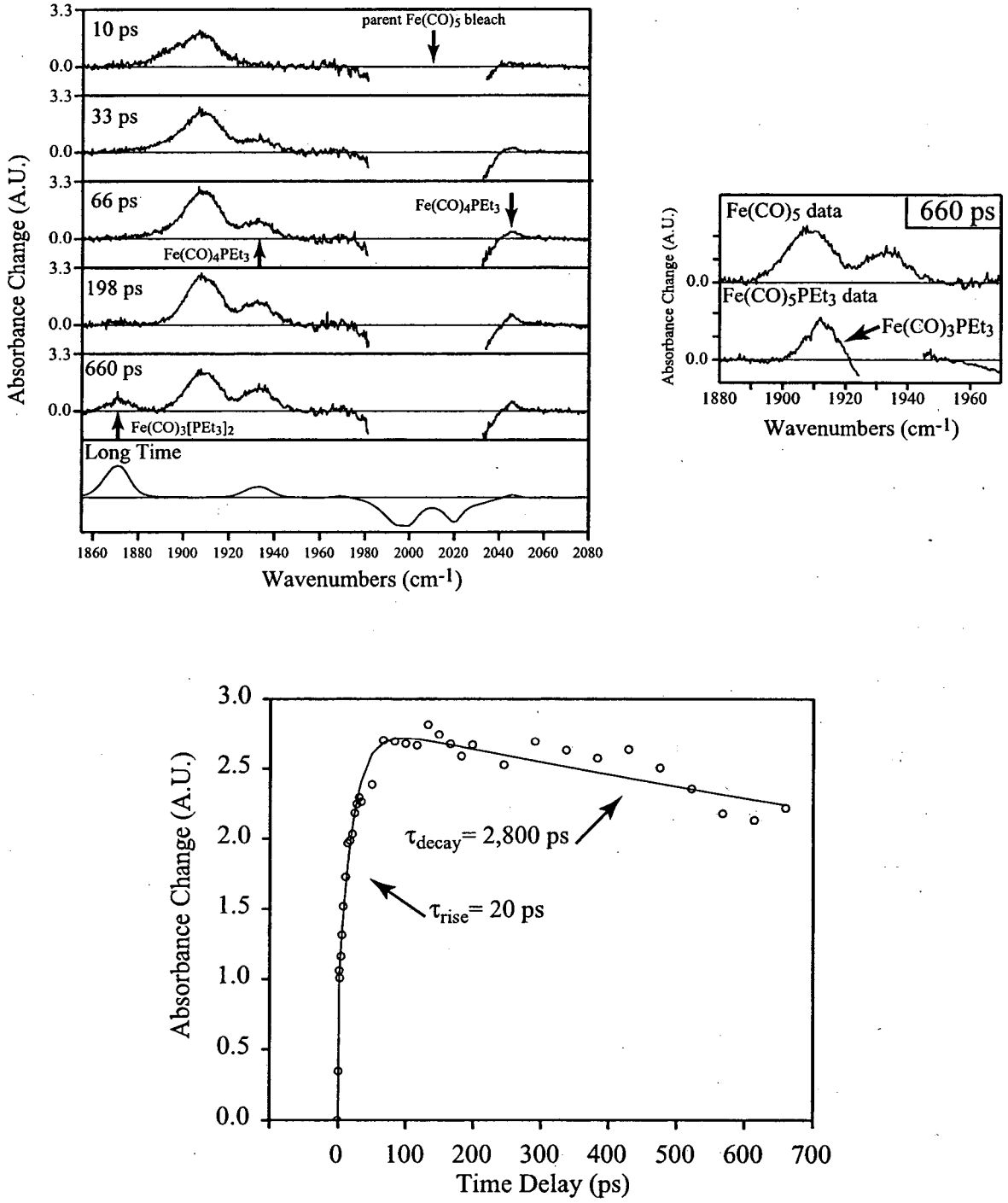

Figure 5.3. The ultrafast difference spectra and kinetics of $Fe(CO)_5$ taken in triethylphosphine solution. Shown in the inset is the difference spectra of $Fe(CO)_4(PEt_3)$ taken in heptane.

B. Photolysis of $Fe(CO)_5$ in neat PEt_3 solution. In neat triethylphosphine solution, the single substituted product $Fe(CO)_4PEt_3$ absorbing at 1932, 1969 and 2047 cm^{-1} appears on a timescale of 50 ps and remains constant to 660 ps as shown in Fig. 5.3. Also appearing in the spectra is an unknown intermediate absorbing at 1908 cm^{-1}, which decays in 2.8 ± 0.5 ns with the concomitant formation of the disubstituted $Fe(CO)_3(PEt_3)_2$ peak at 1870 cm^{-1}. The single substituted $Fe(CO)_4PEt_3$ and disubstituted $Fe(CO)_3(PEt_3)_2$ products are identified by comparing the vibrational frequencies with the literature values,[89,90] and the assignment of the unknown species is given in the discussion. The kinetic trace of the decay of the unknown intermediate is shown at the bottom of Fig. 5.3. The rise times of the iron species may be attributed to vibrational relaxation of the initially hot photoproduct confirmed by the slight narrowing and blue shifting of the photoproduct peak at early times.[14–16] Shown in Fig. 5.3 is the spectrum of the single substituted product $Fe(CO)_4PEt_3$ in heptane solution taken upon photolysis at 295 nm. A single species appears absorbing at 1911 cm^{-1}, which coincides with the unknown intermediate peak seen in the $Fe(CO)_5$ / neat PEt_3 data.

Section 5.3 Discussion

The spectra of $Fe(CO)_5$ in tert–butyl alcohol solution are shown in Fig. 5.1. At early times the triplet $^3Fe(CO)_4$ peaks are broadened and possibly overlapped with both parent $Fe(CO)_5$ and triplet $^3Fe(CO)_4$ hot bands, all of which decay with the concomitant formation of the singlet hydroxyl solvated product species $^1Fe(CO)_4(HOR)$. As summarized in Table 5.1 and Fig. 5.2, the kinetics of the formation of the singlet hydroxyl solvated products are generally faster than observed in the $^1Cr(CO)_5$ studies and

scale linearly with solvent viscosity. The same linear trend is not observed in the chromium data. These results are consistent with the formation of intermediates in different spin states. Triplet $^3Fe(CO)_4$ has been shown to have weak interacts with the alkyl group of the solvent, and yet reacts upon encountering the strong coupling hydroxyl site and quickly cross over to the hydroxyl solvated singlet state. As a result, the reaction timescale is essentially diffusion controlled and thus should have a linear viscosity dependence.[91] On the other hand, the singlet species $Cr(CO)_5$ has stronger interactions with alkanes and the kinetics are dominated by the dissociation timescale of an alkyl / $Cr(CO)_5$ complex.[23,86,87] Consequently, the strength of the metal–alkyl interaction as well as the number of alkyl sites determines the rearrangement timescales for this singlet intermediate.

In triethylphosphine, the triplet $^3Fe(CO)_4$ photoproduct is not directly observed. Instead, the spectra in Fig. 5.3 show the fast formation of $Fe(CO)_4PEt_3$ and an unknown intermediate at 1908 cm^{-1}. While $Fe(CO)_4PEt_3$ concentration appears constant to 660 ps, the intermediate at 1908 cm^{-1} appears to decay in 2.8 ± 0.5 ns with the concomitant formation of the double substituted product $Fe(CO)_3(PEt_3)_2$ absorbing at 1870 cm^{-1}.

Considering that the unknown intermediate and the disubstituted product are kinetically coupled, the identity of the intermediate is proposed to be $^3Fe(CO)_3PEt_3$ and is supported by spectroscopic evidence.

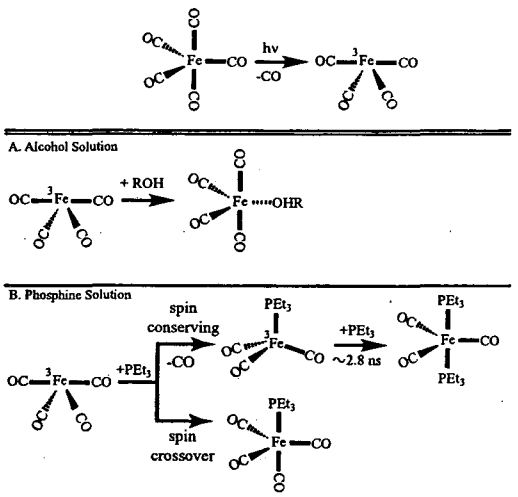

Scheme 5.2: The proposed mechanisms of photochemical ligand substitution.

As seen in the inset of Fig. 5.3, the intermediate $^3Fe(CO)_3PEt_3$ formed upon photolysis of $Fe(CO)_4PEt_3$ in heptane solution absorbs at 1911 cm^{-1}, and no other absorptions attributed to this species are observed. The fact that the absorption frequency of this species is similar to that observed in the $Fe(CO)_5$ / triethylphosphine study and the DFT calculations have established the triplet species is the ground state, we are led to the conclusion that the intermediate is $^3Fe(CO)_3PEt_3$. This result is also consistent with the previously reported mechanism.[59,65] These results are summarized in Scheme 5.2 B.

With the identity of the double–CO substitution intermediate in mind, a mechanism for the phosphine substitution reaction may be proposed. Our previous investigation has shown that upon photolysis of $Fe(CO)_5$ in solution, a single carbonyl is lost and the photoproduct is in the unsolvated ground triplet state.[49] This species is stable to 660 ps in alkane solution yet is very reactive in triethylphosphine. In neat triethylphosphine solution, the initial reaction of $^3Fe(CO)_4$ with PEt_3 is divided into two parallel channels. On the triplet potential energy surface, there exists a concerted process in which a second carbonyl is lost and the $^3Fe(CO)_3PEt_3$ intermediate is formed, which is overall spin conserving. This species then reacts with PEt_3 to form the final di–substituted product $^1Fe(CO)_3(PEt_3)_2$. The reaction of $^3Fe(CO)_4$ with PEt_3 may also nonadiabatically cross to the singlet surface to form $^1Fe(CO)_4PEt_3$, which is chemically inert to substitution at room temperature.[92] The proposed mechanism is qualitatively similar to that previously reported, however the present study finds no spectroscopic evidence for the formation of $^3Fe(CO)_4PEt_3$ as a precursor to $^1Fe(CO)_4PEt_3$ and $^3Fe(CO)_3PEt_3$. As a previous account suggests that $Fe(CO)_5$ also undergo photochemical disubstitution reactions with olefins,[93] the spin conserving/non–conserving reaction to

form monosubstituted and disubstituted products appears to be a more general phenomena.

Section 5.4 Quantum Chemical Modeling.

As in the previous studies of bond activation by coordinatively unsaturated intermediates, we have used quantum chemical calculations to model the interactions of high and low spin transient species with a reactive solvent molecule. The results of these calculations support the conclusions based on the experimental results and reveal a greater detail of the microscopic nature of the interactions between the reactive molecules.

A. Methods The methods used in the characterization of the transient intermediates are similar to those employed in Chapter 4, section 4.3 All geometries were optimized at the 6–31G**/B3LYP level of theory using the Jaguar package.[7,10,11] All optimizations were followed by a frequency analysis to make certain that the optimized geometries were at a minimum. The coupling (spin–orbit) strengths of the proposed triplet intermediates were calculated at the ground state triplet geometries using lanl2dz/casscf optimized wavefunctions,[42,44–47] with the GAMESS–US package.[9] The Z_{eff} at the metal center described by Koseki et. al. was used to calculate the spin–orbit coupling using the lanl2dz basis set.[73]

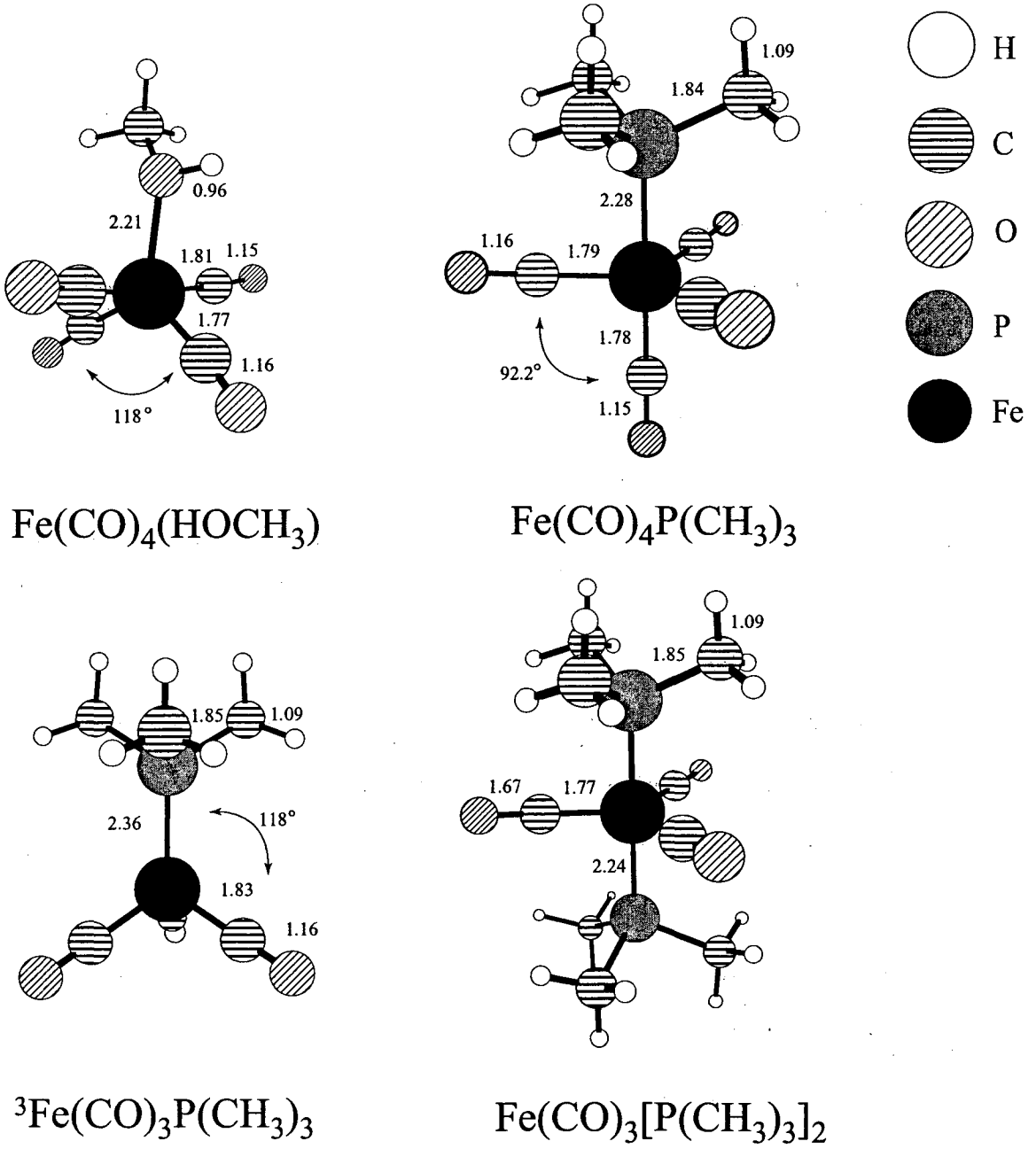

Figure 5.4. The DFT optimized geometries of several of the species observed in the $Fe(CO)_5$ study.

For computational efficiency, the neat PEt_3 interaction with the singlet organometallic complexes was modeled using $P(CH_3)_3$. Likewise, the alcohol interaction calculations use CH_3OH as a model. The bond strengths of the ground state species were also calculated at the DFT / B3LYP level of theory using the counterpoise method to account for basis set superposition error including zero point energy (ZPE) corrections.[74,75] The ΔE for the reactions:

$$P(CH_3)_3 + {}^3Fe(CO)_4 \rightarrow {}^3Fe(CO)_3[P(CH_3)_3] + CO \quad (1)$$

and

$$HOCH_3 + {}^3Fe(CO)_4 \rightarrow {}^3Fe(CO)_3[HOCH_3] + CO \quad (2)$$

were also calculated as $\Delta E = E_{products} - E_{reactants} + \Delta ZPE$.

In order to describe the trends seen in the reactivity of the triplet species ${}^3Fe(CO)_4$ in alcohol solution, the DFT potential energy curves for the singlet and triplet $Fe(CO)_4$ with $HOCH_3$ were calculated by fixing the metal–O bond lengths of the organometallic complex and optimizing the remaining geometric parameters. Likewise the DFT potential surfaces for $Fe(CO)_4$ and $Fe(CO)_3(PEt_3)$ in triethylphosphine were calculated using fixed Fe–P bond lengths using $Fe(CO)_3P(CH_3)_3$ and $P(CH_3)_3$ as model complexes. This was done for both singlet and triplet organometallic fragments at various distances the singlet–triplet crossing region. This type of analysis builds an approximate potential energy surface for the bond activation reaction as a function of the Fe–X (X=P, O) distance, although the actual activation coordinate is more complex due to the high dimensionality of the dynamics.

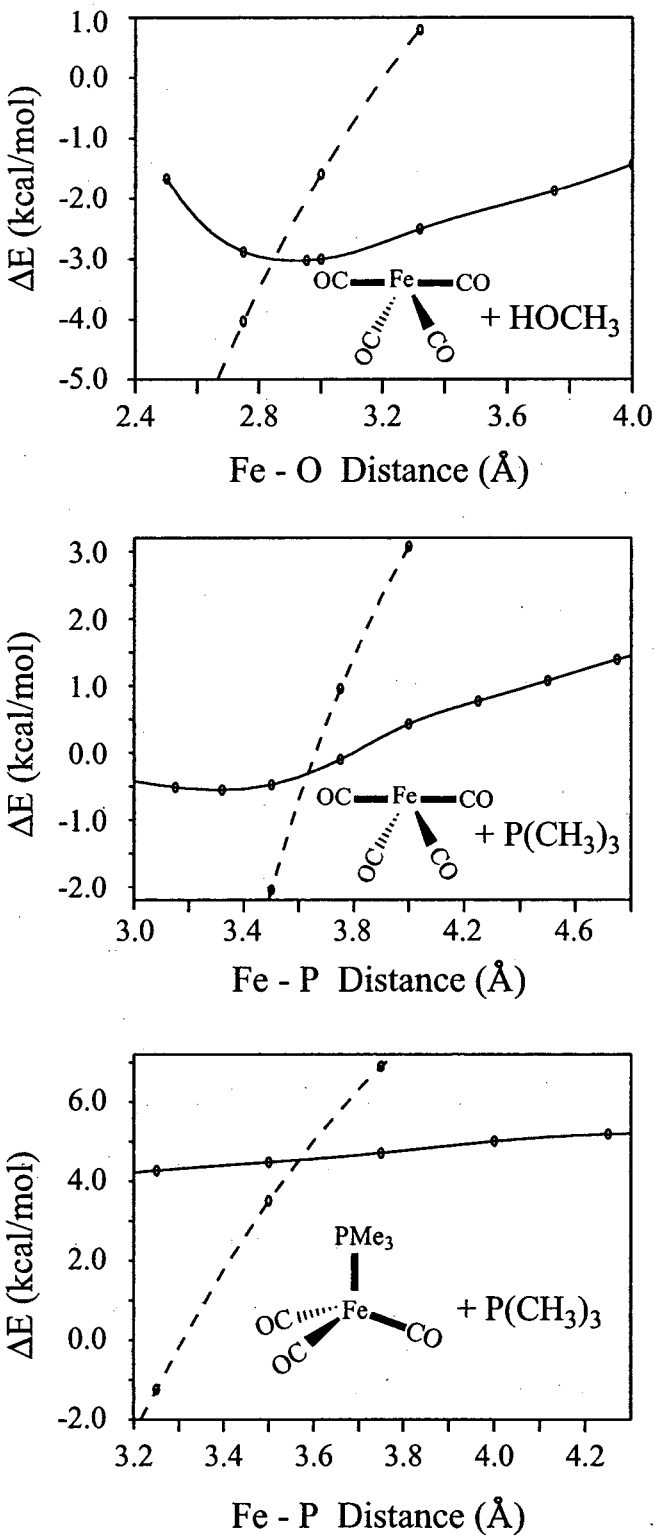

Figure 5.5. The calculated potential energy surfaces of singlet and triplet $Fe(CO)_4$ with various ligands.

B. Geometry optimization. Shown in Fig. 5.4 are the ground state geometries and relevant geometric parameters of $^1Fe(CO)_4(HOCH_3)$, $^1Fe(CO)_4P(CH_3)_3$, $^3Fe(CO)_3P(CH_3)_3$, and $^1Fe(CO)_3[P(CH_3)_3]_2$. These structures were used in the calculations of ground spin states and ligand binding energies, discussed below.

C. Energy calculations. The calculated metal–ligand binding energies as well as spin state energy splittings are listed in Tables 5.2 and 5.3, respectively. The DFT results predict a lower energy for the triplet state relative to that of the singlet for $^3Fe(CO)_4$, $^3Fe(CO)_3[P(CH_3)_3]$, and $^3Fe(CO)_3[HOCH_3]$ and as summarized in Table 5.3. The reaction enthalpy for carbonyl substitution of $^3Fe(CO)_4$ by $P(CH_3)_3$ (1) has been calculated to be +1.4 kcal/mol, while the corresponding substitution by $HOCH_3$ (2) is unfavorable by +14.5 kcal/mol. In order to understand the reactivity of these triplet species, the Fe–O (Fe–P) coordinate potential energy curves were calculated at the DFT level of theory. The results are shown in Fig. 5.5 and are summarized in Table 5.4. The triplet / singlet $Fe(CO)_4 + HOCH_3$ crossover point occurs at a Fe–O distance of 2.85 Å at –3.01 kcal/mol below the (unsolvated) triplet ground state energy. The triplet $Fe(CO)_4$ / $HOCH_3$ calculations also show that the triplet species has an attractive interaction with the model alcohol, which occurs at a well depth of –3.02. kcal/mol near the spin crossing point. The triplet / singlet $Fe(CO)_4 + P(CH_3)_3$ and $Fe(CO)_3P(CH_3)_3 + P(CH_3)_3$ crossover points occur at Fe–P distances of 3.63 and 3.57 Å and at potentials of –0.31 and +4.53 kcal/mol, respectively. The $^3Fe(CO)_4 + P(CH_3)_3$ calculation results show that this triplet species has a slight attractive interaction with the model phosphine solvent. The –0.6 kcal/mol well of this interaction occurs at a metal–P distance of 3.30 Å, which is 1.02 Å away from the optimized singlet state Fe–P product distance of 2.28 Å. A local

Fragment	Ligand	ΔE (kcal/mol)
$Fe(CO)_4$	CO[a]	67.3 (ax), 52.2 (eq)
$^1Fe(CO)_4$	$HOCH_3$	13.2
$^1Fe(CO)_4$	$P(CH_3)_3$	46.0
$^3Fe(CO)_4$	$P(CH_3)_3$	1.3
$^3Fe(CO)_3$	$P(CH_3)_3$	28.8
$^1Fe(CO)_4$ $[P(CH_3)_3]$	$P(CH_3)_3$	37.8

a. From ref. 49.

Table 5.2. The binding strengths of various organometallic species with CO, MeOH, and $P(CH_3)_3$.

(ground state)–organometallic	ΔE[a] (DFT) kcal/mol	vert.–ΔE[b] (DFT) kcal/mol
(triplet)–$Fe(CO)_4$	5.43[c]	22.9
(triplet)–$Fe(CO)_3P(CH_3)_3$	6.31	29.3
(triplet)–$Fe(CO)_3(HOCH_3)$	3.09	27.7

a. Calculated as E(singlet)–E(triplet)
b. The ΔE between the ground and excited spin state at the ground state geometry
c. From ref. 7.

Table 5.3. The energetic splitting between singlet and triplet states at various levels of theory.

minimum of the $^3Fe(CO)_3P(CH_3)_3$ / $P(CH_3)_3$ interaction occurs at a Fe– P distance of 3.07, however the complex is unstable with respect to the isolated fragments by +4.2 kcal/mol. Overall, there does not appear to be a significant attractive interaction between triplet $^3Fe(CO)_3P(CH_3)_3$ and $P(CH_3)_3$.

Spin–orbit coupling (SOC) calculations at the ground state triplet geometry were also performed using the optimized multiconfigurational wavefunction and are summarized in Table 5.4. Overall, the coupling constants are similarly small for $Fe(CO)_4$ and $Fe(CO)_4P(CH_3)_3$, and for the most part the observed dynamics may be attributed to the calculated singlet / triplet spin crossing barriers.

C. Understanding the Trends of Reactivity. While it has been shown that triplet $^3Fe(CO)_4$ is stable to 660 ps in alkane solution, this intermediate reacts on a fast (ps) timescale in alcohol and triethylphosphine solution. Although triplet $^3Fe(CO)_4$ is very reactive, the triplet intermediate $^3Fe(CO)_3PEt_3$ reacts in triethylphosphine on a much longer (ns) timescale. The experimental results may be interpreted in terms of the barrier at the singlet / triplet curve crossover and the similarity of the calculated coupling of the singlet and triplet surfaces.

The trends in the reactivity of these species are elucidated the approximate nonadiabatic potential energy surfaces generated by the DFT (singlet and triplet organometallic) / (model alcohol or phosphine) calculations in Fig. 5.5. The singlet state (dashed) curves for all the species slopes downhill with decreasing Fe–O (Fe–P) distance, which shows that the singlet substituted product is overall the most favorable species energetically. These theoretical calculations explain the fast reactivity of triplet $Fe(CO)_4$ in alcohol and triethylphosphine solution. This system appears to have no classical barrier to the reaction due to the attractive interactions between $^3Fe(CO)_4$ species with $HOCH_3$ and $P(CH_3)_3$. The triplet species Fe–O (Fe–P) minima are on the order of 1 Å from the singlet activated product bond length, which indicates that only a slight rearrangement is necessary to form the product. Although the spin–orbit strength

complex/ model solvent	Minimum (Å)[a]	interaction E (kcal/mol) [b]	singlet/ triplet crossover (Å)[c]	Barrier (kcal/mol)[d]	SOC (cm^{-1})	τ (ps)
$Fe(CO)_4/CH_3OH$	2.92	−3.02	2.85	−3.01	2.6	<42
$Fe(CO)_4/$ $P(CH_3)_3$	3.30	−0.6	3.63	−0.31	2.6	<50
$Fe(CO)_4P(CH_3)_3/$ $P(CH_3)_3$	–	–	3.57	4.53	36	2800

a. The Fe–O (Fe–P) distance at a local minimum.
b. The well depth at the local minimum.
c. The Fe–O (Fe–P) distance where the singlet and triplet curves cross.
d. The energy at the singlet / triplet crossover.

Table 5.4. The results of the DFT potential energy curve calculations. The singlet / triplet spin–orbit couplings and the triplet species lifetimes in solution are also summarized.

of $Fe(CO)_4$ is calculated to be very small, the low classical barrier as well as triplet–solvent interactions elucidates why such a fast reaction occurs between $^3Fe(CO)_4$ and alcohols and triethylphosphine.

There does not appear to be an attractive interaction of triplet $^3Fe(CO)_3P(CH_3)_3$ with $P(CH_3)_3$, resulting in a larger classical reaction barrier. The spin–orbit strengths of $^3Fe(CO)_3P(CH_3)_3$ and $^3Fe(CO)_4$ are comparably low, and as a result the longer timescale of this reaction compared to $^3Fe(CO)_4$ + $P(CH_3)_3$ follows the trend in the calculated classical barriers. It is interesting to note that there is no evidence for disubstitution in alcohol solution. Unfortunately, we have not been able to calculate the transition state structures for these disubstitution reactions with certainty. It is interesting to note, however, that the DFT enthalpy results show that carbonyl substitution of $^3Fe(CO)_4$ by

$P(CH_3)_3$ is energetically unfavorable only by +1.4 kcal/mol. In contrast, the calculated ΔE for carbonyl substitution of $^3Fe(CO)_4$ by $HOCH_3$ is an order of magnitude larger.

Section 5.5 Conclusion

We have shown that the dynamics of $^3Fe(CO)_4$ are consistent with triplet state reactivity. The fact that high spin $^3Fe(CO)_4$ has negligible interactions with alkyl groups, the lifetime of this species scales with the inverse of the solvent viscosity in alcohol solution. This is in contrast with the dynamics seen with the singlet intermediate $^1Cr(CO)_5$, which has a very complex interactions with the solvent environment. These complex interactions mask the effects of solvent viscosity on the reaction rate. The reactivity of $^3Fe(CO)_4$ with phosphines is also consistent with triplet state dynamics. The unusual two carbonyl photosubstitution has been found to be a concerted process on the triplet state manifold. Despite previously reported mechanisms, this investigation found no evidence for triplet state / solvent complexes or singlet intermediates.

The theoretical methods employed in this manuscript greatly assist our understanding of these transient intermediates, which have lifetimes too short for conventional characterization. As in the previous work on $Fe(CO)_5$ and $CpCo(CO)_2$ in triethylsilane, the reaction rates of triplet intermediates may be understood in light of the spin–orbit coupling and the approximate potential energy surfaces generated using Density Functional Theory. The reaction rates have been found to correlate to the classical barrier at the singlet / triplet crossing region, given a similar spin–orbit coupling.

Chapter 6. Ultrafast UV Pump/IR Probe Studies of C–H Activation In Linear, Cyclic and Aryl Hydrocarbons

6.1 Introduction

The C–H bond activation reaction by transient organometallic species is the subject of great interest in the chemical sciences.[28,51,94–98] Previously, we reported our results on the mechanism of photochemical C–H activation by η^3–Tp*Rh(CO)$_2$ (Tp*=HB–Pz3*, Pz*=3,5–dimethylpyrazolyl),[1,26] which is known to form stable C–H activated products upon photolysis with appreciable quantum efficiency.[99–101] These findings are summarized in Scheme 6.1. While this work focused on the role of intramolecular ligand dynamics, a natural question is to assess the influence of the hydrocarbon structure in the activation process. A number of recent studies have addressed this issue for related transition metal systems, although none have focused on ultrafast timescales.[102–104]

It has been established that C–H activation by Group 9 coordinatively unsaturated complexes is a two–step process.[97,105–108] The first step (coordination) involves binding of the hydrocarbon to the coordinatively unsaturated metal center, while the second step (insertion) involves breakage of the C–H bond with the concerted formation of new metal–carbon and metal–hydride bonds. With regard to the coordination step, saturated alkanes are thought to form σ–complexes through interaction of the metal with a C–H bond. Olefins and aromatic compounds can also

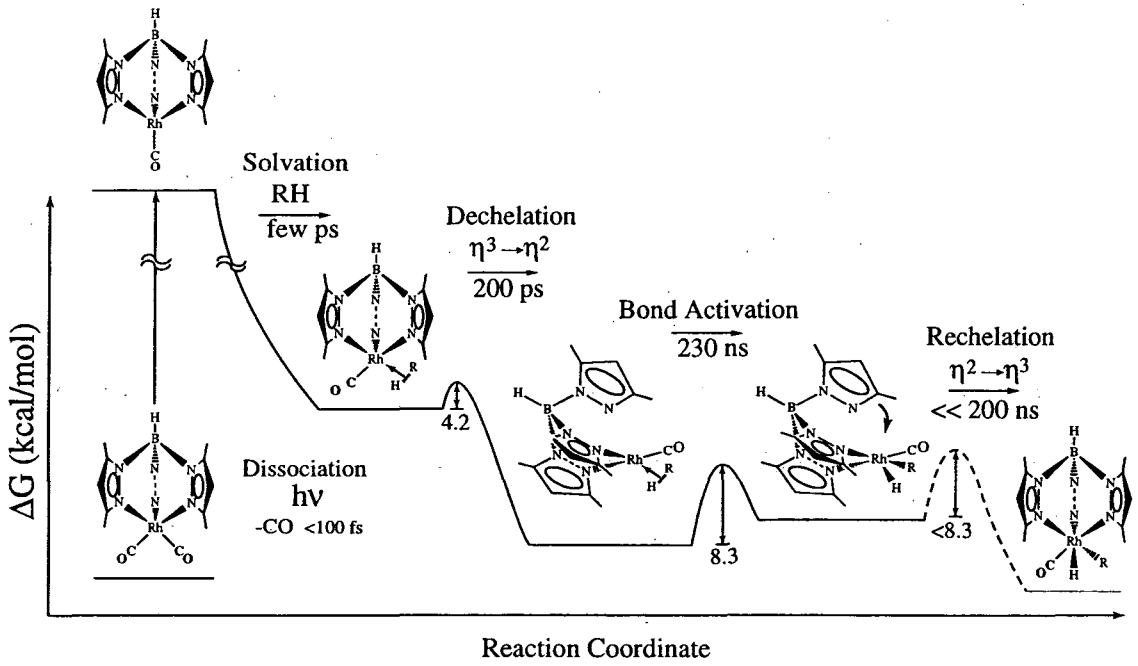

Scheme 6.1 The C–H bond activation mechanism of η^3–Tp*Rh(CO)$_2$ in linear and cyclic hydrocarbons.

bind to the metal center through their π electron systems.[109–114] The role of such π–complexes in C–H activation of unsaturated hydrocarbons has not been entirely resolved.[115]

The insertion step has been studied in great detail. Bergman and co–workers have shown that for reaction of hydrocarbons at the Cp*Rh(CO) center in low temperature liquid Kr, insertion proceeds two to ten times more rapidly for linear alkanes than for the comparable saturated cyclic substrates.[104] In a similar vein, Jones and co–workers have recently shown that the relative barrier for insertion at the Tp*Rh(CNCH$_2$C(CH$_3$)$_3$) center increases in the order methane < primary C–H < secondary C–H.[102] The results presented in this chapter will attest to the generality of these results.

6.2 Experimental Results

A. $Tp^*Rh(CO)_2$ in linear and cyclic hydrocarbons. The C–H activation reactions of η^3–$Tp^*Rh(CO)_2$ in n–pentane and n–hexane as well as in cyclopentane and cyclohexane have been previously investigated by our group. The results of these studies have shown that the dynamics are divided between early picosecond and longer timescale nanosecond to microsecond components. On the early picosecond timescale, the spectral data indicate that there is little difference in the reactivity between linear and cyclic alkanes. After the initial photochemical CO loss, the coordinatively unsaturated organometallic is solvated via the C–H bond to form a σ–complexed intermediate. After 200 ps, the Tp* ligand in known to dechelate to an η^2 form as confirmed by analogous studies with η^2–Bp*Rh(CO)(alkane) (Bp*=H_2BPz_2*) and by theoretical calculations.[116] On the nanosecond timescale, the C–H bond of the bound substrate in the η^2–Tp*Rh(CO)(alkane) complex is activated, prompting the rechelation of the pyrazolyl group to form the product. This process is illustrated in Scheme 6.1.

It is in the nanosecond timescale that differences are noted between linear and cyclic hydrocarbons. Shown in Figure 6.1 are the nanosecond kinetics of the product η^3–Tp*Rh(CO)(H)(R) in n–pentane and in cyclopentane. Although the rise time of the product in n–pentane is difficult to determine due to the transient heating of the sample during the course of the experiment, the formation of the product in n–pentane is nonetheless significantly faster than observed in cyclopentane solution. Similar results are obtained in n–hexane and cyclohexane.

In order to explore the differences between linear and cyclic hydrocarbons further, the reaction of η^3–$Tp^*Rh(CO)_2$ in methyl–cyclohexane was examined. It was

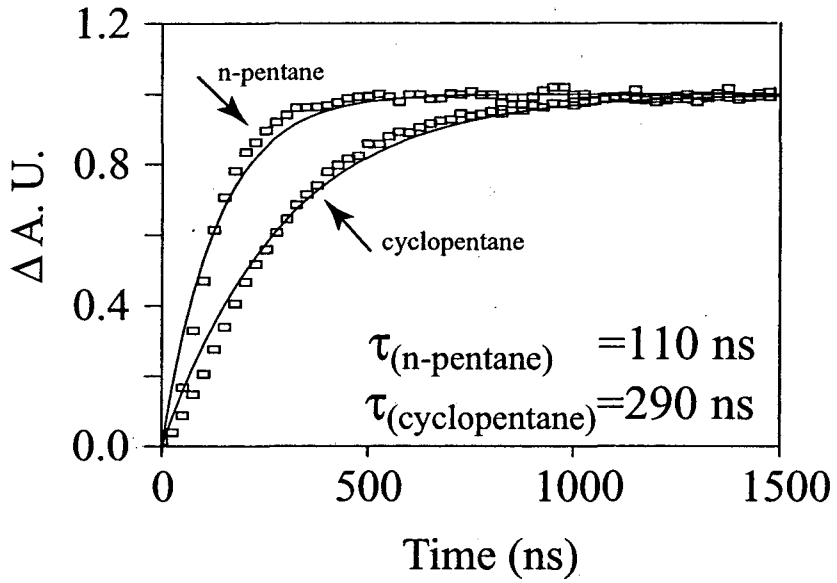

Figure 6.1 Transient kinetics of the product η^3–Tp*Rh(CO)(H)(R) observed in cyclopentane and n–pentane.

found that the final activation step timescale is instrument limited and is similar to that of linear alkanes, which is likely due to preferential activation at the primary methyl site despite the greater number of methylene C–H bonds. Experiments in mixed linear / cyclic alkane solvents also indicate a faster formation of the product upon addition of a small portion of n–pentane to neat cyclopentane.[117]

B. Tp*Rh(CO)$_2$ in aromatic hydrocarbons. The C–H activation reaction of η^3–Tp*Rh(CO)$_2$ in d_6–benzene and toluene has been studied. The early time spectra of η^3–Tp*Rh(CO)$_2$ in d_6–benzene are shown in Figure 6.2. The results indicate that the previously proposed C–H activation mechanism is not significantly altered in aromatic solvents at early times. The solvated monocarbonyl appears at 1965 cm^{-1} and decays in ~200 ps to form a new intermediate absorbing at 2006 cm^{-1}. Shown in Figures 6.3 and 6.4 are the nanosecond spectra and kinetics of η^3–Tp*Rh(CO)$_2$ in d_6–benzene. The

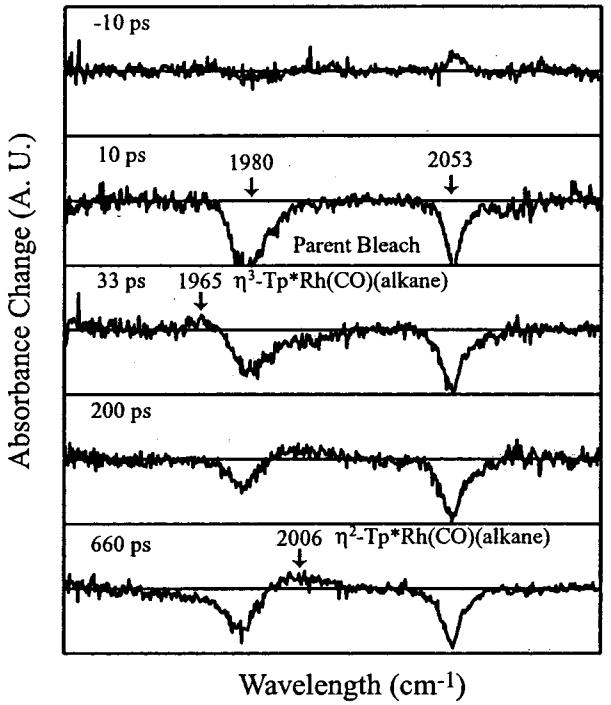

Figure 6.2 Transient difference spectra in the CO stretching region for η^3–Tp*Rh(CO)$_2$ in neat d_6–benzene at 10, 33, 66, 198 and 660 ps following UV photolysis.

intermediate absorbing at 2006 cm^{-1} is seen to decay with a concomitant rise in the bond activated product η^3–Tp*Rh(CO)(D)(C_6D_5) absorbing at 2042 cm^{-1}. This transient intermediate decays on a 2.4 ±0.2 μs timescale, while the C–D activated product's growth monitored at 2043 cm^{-1} has a thermal effect limited (<120 ns) rise as well as a longer μs growth component that can not be accurately determined from the data. While the μs component of the product formation may be correlated with the μs decay of the intermediate absorbing at at 2006 cm^{-1}, the faster timescale growth must be due to product formation from an unobserved intermediate.

The nanosecond spectra and kinetics of η^3–Tp*Rh(CO)$_2$ in toluene are almost identical to the d_6–benzene results. An intermediate species is observed at 2005 cm^{-1},

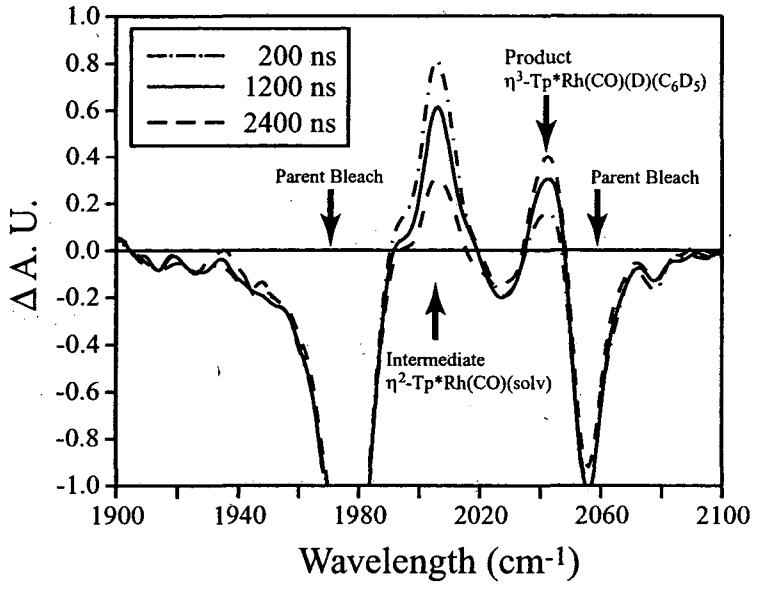

Figure 6.3 Transient difference spectra in the CO stretching region for η^3–Tp*Rh(CO)$_2$ in neat d_6–benzene at 200, 1200, and 2400 ns following UV photolysis.

decaying along a 2.1 ± 0.1 μs timescale. The product η^3–Tp*Rh(CO)(H)(C_7H_7) absorbing at 2042 cm^{-1} kinetics are biexponential, with an instrument limited rise and a longer μs component that can not be accurately determined from the data. These results indicate that bond activation in toluene and d_6–benzene occur by similar mechanisms.

The fact that the intermediates and product species in these aryl C–H activation reactions have absorptions that are significantly shifted with respect to the intermediates η^2–Tp*Rh(CO)(solvents) and products η^3–Tp*Rh(CO)(H)(R) seen in the linear and cyclic hydrocarbon solvent data prompted the measurement of the nanosecond spectrum of the compound η^2–Bp*Rh(CO)$_2$ in d_6–benzene, as shown in Figure 6.5. The results indicate that the known intermediate η^2–Bp*Rh(CO)(d_6–benzene) absorbs at 1990 cm^{-1}, as seen in the previous linear alkane and cyclic hydrocarbon data. These results call into

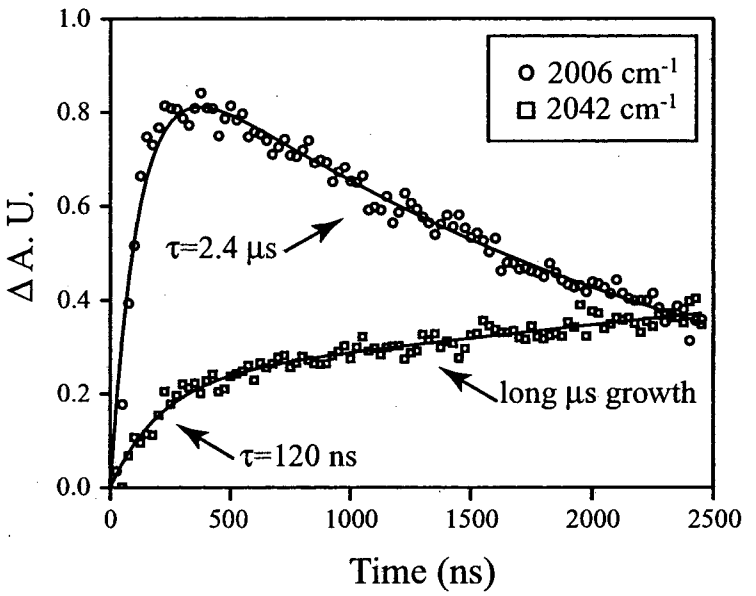

Figure 6.4 Ultrafast kinetics of the intermediate η^2–Tp*Rh(CO)(solvent) and product η^3–Tp*Rh(CO)(H)(R) in d_6–benzene. The time constants for the exponential fits (solid line) are shown in the graph.

question the nature of the intermediate state in these aryl C–H activation studies.

C. $CpRh(CO)_2$ in linear hydrocarbons. Shown in Figure 6.6 are the time resolved difference IR spectra of $CpRh(CO)_2$ in n–pentane and n–hexane following UV excitation. At early times the spectra show the fast formation of the monocarbonyl alkyl solvate at 1963 cm^{-1} as well as two well resolved hot bands of the parent $CpRh(CO)_2$ compound at 2020 and 2034 cm^{-1}, consistent with an earlier report.[80] These hot bands decay by 200 ps. At later times the spectra indicate the formation of a new product absorbing at 2019 cm^{-1} with a corresponding decay of alkyl solvate. The species absorbing at 2019 cm^{-1} is assigned as the product $CpRh(CO)(H)(C_5H_{11})$, as its spectral position corresponds to the bond activated product seen at 2016 cm^{-1} in the 50 ns spectrum in hexane. Based on the slight (2.5 ns) decay of the alkyl solvated species, the

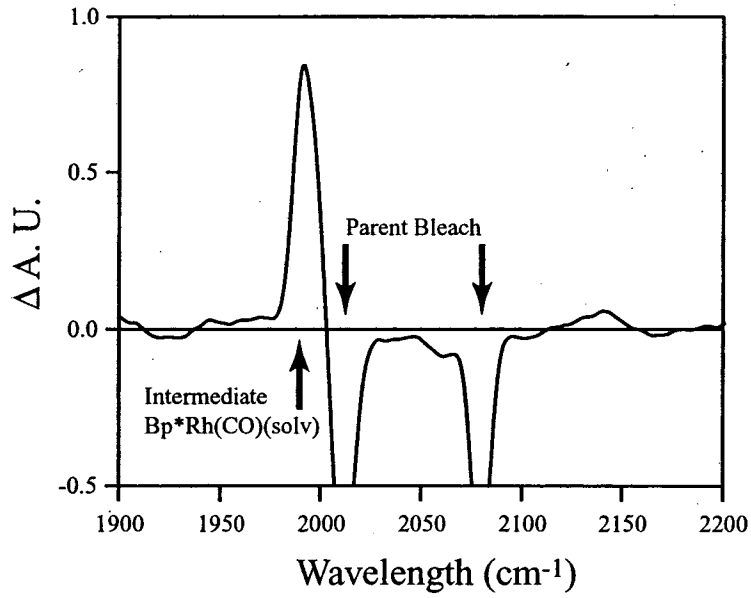

Figure 6.5. Transient difference spectrum in the CO stretching region for η^2–Bp*Rh(CO)$_2$ in neat d_6–benzene after UV photolysis.

reaction barrier of CpRh(CO)$_2$ in neat pentane is estimated from standard transition state theory as 5.6 kcal/mol.

D. DFT Results. Shown in Figure 6.8 are the DFT optimized structures of the proposed intermediate species η^2–Tp*Rh(CO)(benzene) and η^2–Tp*Rh(CO)(CH_4). These structures were calculates at the 6–21G/B3LYP level of theory using the Gaussian 98 suite of packages. The metal atom uses the lanl2dz basis set and corresponding effective core potentials (ECPs). It can be seen that the metal atom adopts a local square planar configuration when the Tp* ligand is coordinated in a bidentate fashion for both of the structures in Figure 6.8. The benzene is bound to the metal via the C=C bond. The binding energies of the metal intermediate and the substrate have been found to be

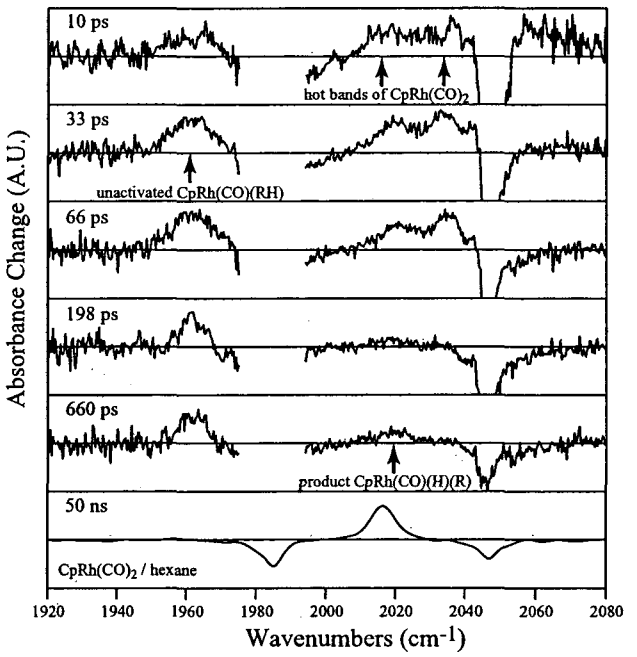

Figure 6.6 Transient difference spectra in the CO stretching region for $CpRh(CO)_2$ in neat n–pentane and n–hexane (50 ns spectrum) after UV photolysis.

−15.3 kcal/mol for benzene and −7.4 kcal/mol for CH_4. A stable structure for the benzene C–H–Rh σ–type coordination could not be found when the Tp* ligand is partially dechelated, as our attempts to locate such a minimum resulted in the geometry converging to an η^3–Tp*Rh(CO)(benzene) configuration.

Section 6.3 Discussion

The findings reported in this chapter are consistent with earlier studies; the C–H activation rate increases from primary to secondary C–H bonds. Similar kinetic preferences have been observed with $CpRh(CO)_2$ as well as η^3–Tp*$Rh(CO)_2$. The results of the $CpRh(CO)_2$ data also elucidate the importance of ligand dynamics of the metal species in the bond activation reaction.

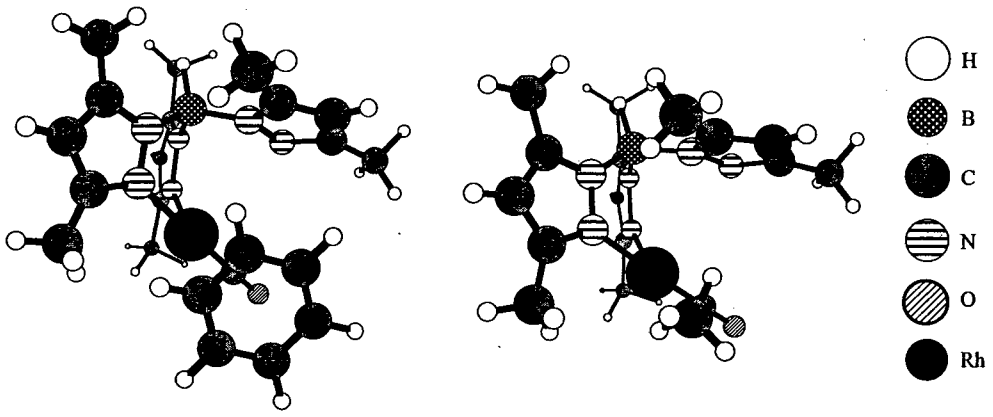

η^2-Tp*Rh(CO)(η^2-C_6H_6) η^2-Tp*Rh(CO)(CH_4)

Figure 6.7 Geometries of the intermediate species η^2–Tp*Rh(CO)(CH_4) and η^2–Tp*Rh(CO)(C_6H_6) optimized at the B3LYP level of theory.

A. Linear versus cyclic hydrocarbon C–H activation. The results of the n–pentane / cyclopentane and the n–hexane / cyclohexane studies with η^3–Tp*Rh(CO)$_2$ as well as CpRh(CO)$_2$ indicate that the activation process is more facile in linear hydrocarbons compared to their cyclic counterpart. There are two possibilities that explain this trend. For one, there may exist electronic differences between linear and cyclic hydrocarbons that account for the faster activation timescale in the former, regardless of whether a primary or a secondary C–H bond is activated. A more likely explanation is that C–H activation in linear hydrocarbons is occurring preferentially at the primary sites, reacting at a faster rate than activation at secondary sites. Similar observations have been made in the reductive elimination studies of Northcutt et. al., concluding that activation of primary C–H bonds is both kinetically and thermodynamically more favorable compared to secondary C–H activation of the same substrate.[102] Likewise the rates of photochemical C–H activation by Cp*Rh(CO)$_2$ in

linear and cyclic hydrocarbons measured by McNamara et. al. are in agreement with the observation that C–H bond activation in a linear hydrocarbon occurs at a faster rate than observed in the cyclic counterpart.[104] These observations may explain early synthetic results which found that activation in the final product occurs at the terminal primary C–H site of alkanes such as propane and hexane.[118,119] This data, however does not allow us to determine whether C–H activation is occurring exclusively at primary C–H sites in linear hydrocarbons and some degree of secondary C–H activation likely occurs as well. The degree to which primary versus secondary C–H bonds are activated may be understood in context of the previous studies of Si–H activation and alcohol rearrangement, as discussed in previous chapters. An interplay of rearrangement, binding strength and activation barrier are responsible for the observed dynamics.

B. Ligand Dynamics of $CpRh(CO)_2$ in C–H activation. The effect of ligand dynamics in the C–H activation reaction can be studied by comparing the reaction of $CpRh(CO)_2$ to η^3–$Tp^*Rh(CO)_2$ in alkanes. The ultrafast dynamics of $CpRh(CO)_2$ in cyclohexane were previously studied by Asbury et al.[81] The results of these studies showed the exclusive formation of the alkyl solvate CpRh(CO)(cyclohexane) with no evidence for the formation of the bond activated product or a ring slipped intermediate within 500 ps. As the η^3–$Tp^*Rh(CO)_2$ results above have shown that linear alkanes undergo bond activation at faster rates than their cyclic counterparts, we have taken a second look at the reaction of $CpRh(CO)_2$ in n–pentane and n–hexane. The results are shown in Figure 6.6. The spectral data show the fast formation of the alkyl solvated intermediate CpRh(CO)(alkane) absorbing at 1963 cm^{-1} as well as two well resolved vibrationally hot bands of the parent which cools within 200 ps. There is a 2.5 ns timescale decrease in the absorption of the alkyl solvated intermediate with the

concomitant formation of the bond activated product seen at 2019 cm^{-1}. Consequently, there is no evidence for additional ligand dynamics in the C–H activation reaction such as the formation of ring slipped intermediates. These observations also show that the higher barrier towards secondary versus primary C–H activation is also true for $CpRh(CO)_2$. Similar results were obtained in our earlier study of Si–H activation of $CpRh(CO)_2$ in triethylsilane,[49] in which a slight decay of the alkyl solvated species due to C–H activation of the ethyl moiety of the triethylsilane solvent was observed as discussed in Chapter 4.

C. Aryl C–H Activation. At early times, the activation of d_6–benzene by η^3–$Tp^*Rh(CO)_2$ appears qualitatively similar to the linear and cyclic hydrocarbon activation results. Upon UV photolysis of η^3–$Tp^*Rh(CO)_2$ in d_6–benzene, the picosecond spectra shows the formation of a transient species absorbing at 1965 cm^{-1}, which decays within ~200 ps to form an intermediate absorbing at 2006 cm^{-1}. Based upon the previous work, the first intermediate absorbing at 1965 cm^{-1} is proposed to be solvated η^3–$Tp^*Rh(CO)(d_6$–benzene), which rearranges to possibly a dechelated η^2–$Tp^*Rh(CO)(\eta^2$–benzene) intermediate (see below). The decay of η^2–$Tp^*Rh(CO)(\eta^2$–benzene) is kinetically coupled to the growth of the final η^3–$Tp^*Rh(CO)(D)(C_6D_5)$ product on a timescale of 2.4 μs.

While these assignments and general observations are in agreement with the mechanism seen in linear and cyclic alkanes, there are several important differences to note. First, the intermediate species' and products' absorption spectra are ~15 cm^{-1} blue shifted with respect to the spectra of the intermediates and products observed in linear and cyclic alkanes. These results may be explained by previous mechanistic studies,

which found evidence for the formation of a C=C η^2–bound complex as an intermediate to activation.[109–114] The possible coordination by the double bond likely results in the formation of a strongly bound complex, which increases the lifetime of the intermediate as observed in the kinetic data. Based on these results, the intermediate absorbing at 2006 cm^{-1} proposed to be η^2–Tp*Rh(CO)(η^2–benzene) solvated via the C=C double bond of d_6–benzene. These results are supported by our ab initio calculations, in which it was found that the binding strength of the η^2–Tp*Rh(CO)(η^2–benzene) complex is twice as strong as the binding strength of the methane substrate in the η^2–Tp*Rh(CO)(CH_4) intermediate. It is interesting to note that ultrafast experiments with the model precursor η^2–Bp*Rh(CO) in d_6–benzene shows a single absorption at 1990 cm^{-1}, the same as observed in linear and cyclic alkanes. While we propose that the intermediate absorbing at 2006 cm^{-1} is the dechelated double bond solvate, the η^2–Bp*Rh(CO) results and the fact that the product η^3–Tp*Rh(CO)(D)(C_6D_5) absorption is also significantly blue shifted indicate that there are more complex solute / solvent interactions in aromatic solvents than we are presently aware of. This is also supported by our DFT calculations of the model precursor complexes η^2–Bp*Rh(CO)(C_6H_5) and η^2–Bp*Rh(CO)(CH_4), which do not have significantly altered CO stretch frequencies as found for the Tp* analogs. The differences are thus attributed to the effect of the solvent, which are not included in these calculations.

The fact that the bond activated product has biexponential kinetics indicates that there exist two possible routes to the formation of the product. The fast component may be attributed to product formation from an early time Rh–H–C σ–bound species that

forms the bond–activated product on a timescale comparable to what has been observed in linear hydrocarbons. Similar observations have been made in the bond activation reaction of ethylene at the Cp*Ir[P(Me_3)] center [Cp*=$C_5(CH_3)_5$], in which the activation of the vinyl C–H bond does not proceed through a π–complex precursor, but possibly through a σ–complex.[112] The longer ~2 μs timescale component can be attributed to the decay of the π–complex to form the product as the two are kinetically coupled. Unfortunately, as this intermediate is not observed directly, it is impossible to tell whether the Tp* ligand is dechelated into a bidentate form or not.

Results in toluene are similar to the d_6–benzene data. The intermediate and product peak positions are the same as in benzene, and the product growth occurs on a similar μs timescale. This is especially interesting as the methyl–cyclohexane data indicate that the activation of the primary carbon is favored. Perhaps the formation of the π–complex directs the reaction towards exclusive activation at aromatic sites, as has been observed in previous activation studies using analogous compounds.[120] The mechanism for aromatic C–H activation by η^3–Tp*Rh$(CO)_2$ is summarized in Scheme 6.2.

4. Transition States. The fact that the fully chelated CpRh(CO) intermediate is faster CH activator than η^2–Tp*Rh(CO) has implications for the nature of the transition state. The general picture of CH or SiH bond activation is that the metal is able to simultaneously donate electron density to the antibonding orbitals as well as accept electron density from the bonding orbitals. However, this is not consistent with observations made in this study and that of McNamara et al., which shows that the

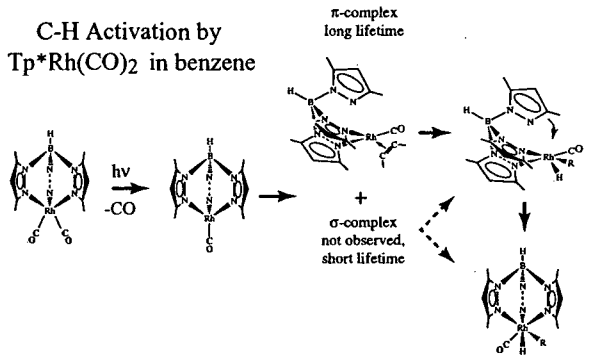

Scheme 6.2 The C–H bond activation mechanism of η^3–Tp*Rh(CO)$_2$ in aryl solvents. It cannot be determined whether the sigma complex exists as a dechelated intermediate, see text. Inset shows the simple C–H activation mechanism of CpRh(CO)$_2$ in linear hydrocarbons.

facility to activate CH bonds follows the trend η^5–Cp*Rh(CO) > η^5–CpRh(CO) > η^2–Tp*Rh(CO). Another study by Tellers et al. has recently confirmed that addition of electron donating ligands has the effect of increasing the rate of arene activation in a series of cationic transition metal complexes.[121] As a fully bonded Cp or Cp* ligand should donate extra electron density to a metal than a dechelated η^2–Tp* ligand. This observation has been supported by preliminary DFT calculations, which show that there is more charge density at the metal for a CpRh(CO) intermediate than a η^2–Tp*Rh(CO) species by ~1/3 of an electron. The extra electron density likely increases the overlap between the metal electrons and the antibonding orbitals of an alkane, and is the fundamental driving force behind the rate of CH activation. Future experiments in our lab will hopefully shed more light on this proposal.

Section 6.4 Conclusion

We have shown through direct observation that the compound η^3–Tp*Rh(CO)$_2$ reacts at a faster rate in linear hydrocarbons compared to their cyclic counterparts. The source of this observation is likely the fact that the primary C–H bonds are preferentially activated over the C–H bonds of secondary sites. In the case of C–H activation in aryl solvents, a strongly bound η^2–aryl complex is formed resulting in a much longer timescale for activation. The activation in aryl solvents also appears to have two pathways for activating the C–H bond. The results of the CpRh(CO)$_2$ studies reveal that additional ligand dynamics do not appear to play a direct role in the activation process. The preferential activation of linear alkanes has also been shown to be true for CpRh(CO)$_2$ as well as η^3–Tp*Rh(CO)$_2$. The ability to donate charge density to antibonding CH orbitals of an alkane is the reason for the observed rate differences between the intermediates CpRh(CO) and η^2–Tp*Rh(CO).

Part II: Theoretical Studies of Solvation Dynamics

Due to some of the limitations of ultrafast spectroscopy, including finite pulse duration and the effects of vibrational relaxation, the microscopic nature and early time dynamics of some chemical systems may not be elucidated using this method. In order to quantify these properties, we have turned to using theoretical methods such as molecular dynamics simulations. Specifically, the solvation dynamics of the excited states of $[Ru(bpy_3)]^{2+}$ and the excess electron have been investigated. Rearrangement of token ligands to coordinatively unsaturated organometallic intermediates have also been studied in Transition Path Sampling (TPS) simulations. These studies have shown that the formation of localized excited states of $[Ru(bpy_3)]^{2+}$ is intrinsically favorable. The degree to which these states are stabilized in an acetonitrile solvent scales with the dipole moment of the excited state. The structure and dynamics of a solvated electron in low temperature bulk, in the gas phase and at a surface interface have also been investigated. These results reveal that there are minimal differences between the timescales of solvation in a room temperature liquid and in a low temperature methanol glass. This implies that large scale hydrogen bond breakage and diffusive motion does not play a significant role in equilibrium solvation dynamics. The newly discovered interfacial solvated electron has also been investigated. Finally, we have characterized the intramolecular rearrangement of methanol with the coordinatively unsaturated intermediate $Cr(CO)_5$. These studies have allowed us to derive a generalized mechanism for this form of ligand exchange reaction.

Chapter 7

The Solvation Dynamics of the Excited States of Tris–(2,2'–bipyridine)ruthenium(II)

Section 7.1. Introduction

The photochemistry of tris–(2,2'–bipyridine)ruthenium(II), abbreviated as $[Ru(bpy)_3]^{2+}$, has been the subject of numerous investigations. This species is often used as a model complex for studying organometallic charge transfer reactions and complexes of this type have recently been incorporated as dye sensitizers for TiO_2 based solar cells. Despite the large amount of attention that $[Ru(bpy)_3]^{2+}$ has received in the literature, there does not appear to be an agreement about the early time dynamics of this species. The issues that are still debated include localization of the excess charge density as well as the timescale for intersystem crossing to the lowest triplet excited state manifold. These issues are discussed in more detail below.

It has been established that the intense visible absorptions of $[Ru(bpy)_3]^{2+}$ are due to metal to ligand charge transfer (^{1}MLCT $\leftarrow$ $^1A_1$) in which a single electron is excited from a metal d–type orbital to the antibonding π^* system of a bipyridine ligand.[122–124] Based upon femtosecond absorption experiments, the singlet state that is initially populated upon low energy visible excitation intersystem crosses on a timescale of 100–300 fs to a long lived triplet ^{3}MLCT manifold. This process occurs with a near unit quantum efficiency.[125,126] However, a recent fluorescent upconversion study has

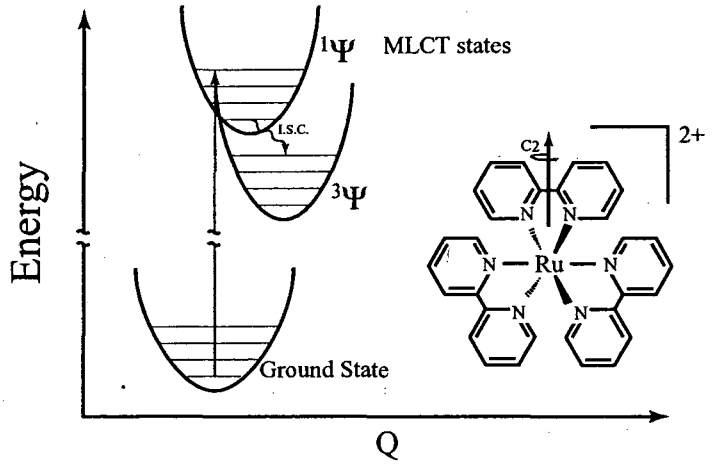

Scheme 7.1 The electronic excited state dynamics of $[Ru(bpy)_3]^{2+}$.

determined that the intersystem crossing occurs within 45 ± 15 fs.[127] These electronic state dynamics are summarized in Scheme 7.1. The photophysics of this system are interesting due to the fact that the excess electron eventually becomes localized on one of the three equivalent bipyridine ligands in the excited states.[128–132] The localization dynamics have been studied in recent femtosecond absorption anisotropy experiments. The results of these studies have suggested that the singlet excited state initially formed upon visible photon absorption has excess electron density delocalized over three equivalent bipyridine ligands.[126] The excess electron then localizes on a single ligand, which has been proposed to be the result of a solvent assisted mechanism. Resonance Raman studies, however, have indicated that the excited singlet states formed upon photoexcitation of $[Ru(bpy)_3]^{2+}$ may be initially localized in character.[133]

The excited singlet and triplet states of $[Ru(bpy)_3]^{2+}$ have been studied in the gas phase and in solution using a combination of ab initio, DFT and Molecular Dynamics (MD) methods. First, the lowest excited singlet and triplet state properties were

calculated using a wavefunction based approach from which models suitable for MD simulations were created. Using MD based thermodynamic integration techniques, the solvent / solute interactions of the first excited $[Ru(bpy)_3]^{2+}$ singlet and triplet states with a polar acetonitrile bath have been studied. These results have shown that the $[Ru(bpy)_3]^{2+}$ excited state species with localized charge redistribution are preferentially solvated in an acetonitrile bath. These results provide a microscopic knowledge of the excited states of $[Ru(bpy)_3]^{2+}$ as well as the nature of the solute / solvent interactions of these states.

Section 7.2. Methods and Results

Our original purpose was to try to simulate the solvent response timescale for $[Ru(bpy)_3]^{2+}$ in acetonitrile solution to ascertain whether the experimentally derived localization timescale was consistent with the solvent response from MD simulation. We also wished to determine whether a localized or a delocalized charge transfer excited state has more favorable interactions in a polar solvent. To this end, the ^1A geometry of $[Ru(bpy)_3]^{2+}$ was optimized at the B3LYP level of theory and used a Natural Bonding Orbital (NBO) calculation to define the electrostatic charges at each site. The coordinates of Daul et. al. was used as the starting structure.[134] Other than electrostatic charges, the bpy sites used the Lennard–Jones parameters of liquid pyridine developed by Jorgensen et al.[135] while the metal atom did not use such a potential. The 6–site acetonitrile model of Bohm et al. was used to describe the solvent. All model parameters are given in Table 7.1.[136] The simulations use a single rigid $[Ru(bpy)_3]^{2+}$ unit placed in a bath of 400 acetonitrile molecules in a square simulation box of volume 32.686^3 Å^3. The $[Ru(bpy)_3]^{2+}$ molecule was held at the center of the simulation box while the solvent

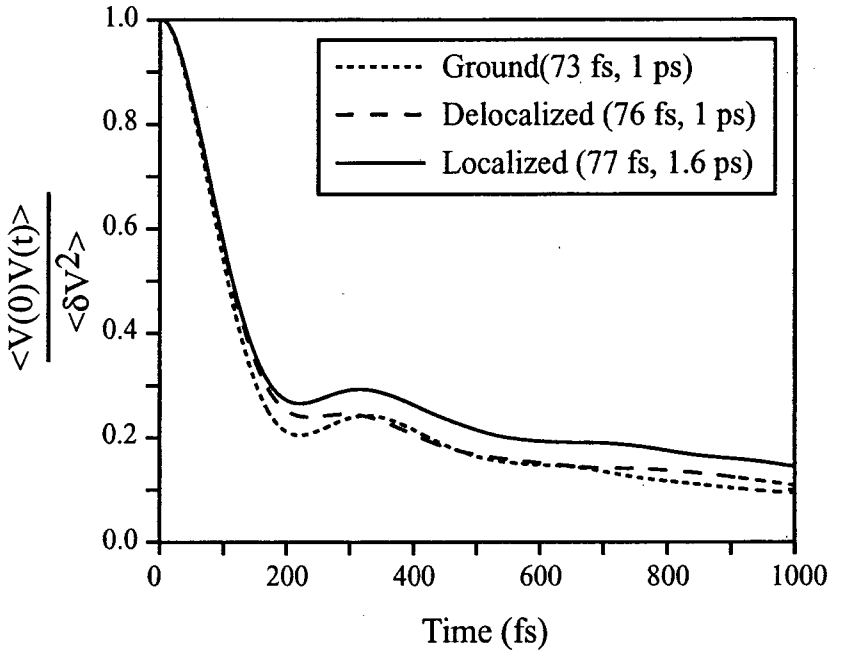

Figure 7.1. The equilibrium solvent response for the ground state and excited state models of $[Ru(bpy)_3]^{2+}$ discussed in the text.

Compound / site	σ (Å)	ε (kcal/mol)	q
[a]CH_3CN / N	3.3	0.4177	−0.514
[a]CH_3CN / C1	3.4	0.4177	0.488
[a]CH_3CN / C2	3.0	0.4177	−0.577
[a]CH_3CN / H	2.2	0.0835	0.201
[b]$[Ru(bpy)_3]^{2+}$ / CH	3.75	0.4602	c
[b]$[Ru(bpy)_3]^{2+}$ / N	3.25	0.7113	c
$[Ru(bpy)_3]^{2+}$ / Ru	–	–	c

a. From Ref. 135.
b. From Ref. 134.
c. See Harris Group lab archives for partial charges of the for the ground and excited states of $[Ru(bpy)_3]^{2+}$.

Table 7.1. The Lennard–Jones and partial charges of the acetonitrile solvent and $[Ru(bpy)_3]^{2+}$ solute.

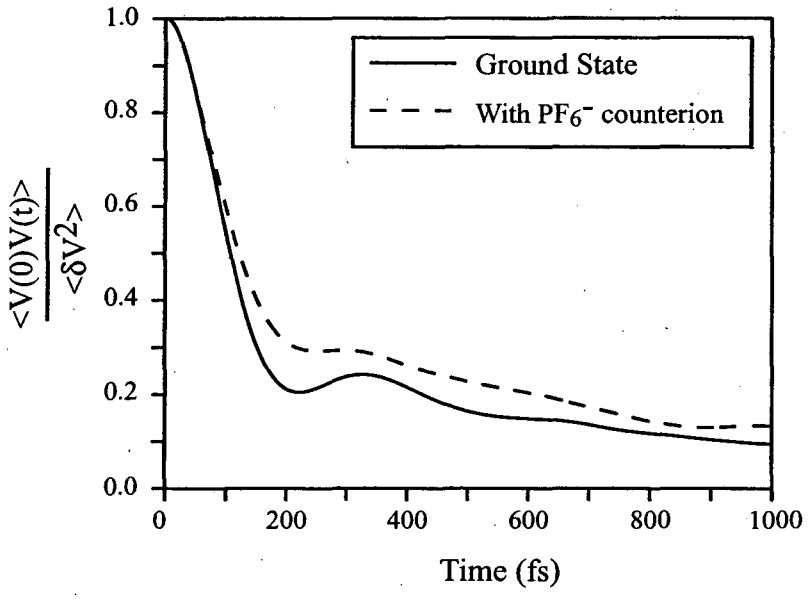

Figure 7.2. The equilibrium solvent response for the ground state with and without a single PF_6^- counterion.

is allowed to move freely. The internal geometries of the solvent molecules were fixed using the SHAKE method and the NVE ensemble has been employed throughout these simulations.[137] The calculations used a time step of 2.5 fs.

The equilibrium solvent response was calculated for the ground state and for two model excited states. A "delocalized" excited state was defined as having a whole unit of electric charge removed from the ruthenium center with a corresponding addition of 1/6 e^- unit of charge placed at the centroid of all the pyridine subunits of the ligand system. This model retains D_3 symmetry. The "localized" state had 1/2 e^- unit of excess charge placed at the centroid of two pyridine units on one ligand and is thus C_2 symmetric. The solvent response, defined as $\langle V(0)V(t)\rangle/\langle\delta V^2\rangle$ was calculated for all three models and is shown in Figure 7.1. These equilibrium solvation dynamics are largely composed of an

initial fast Gaussian component followed by an exponential decay. The $\tau_{1/2}$ Gaussian component timescale for all three models is on the order of 75 fs and the solvent response appears very similar in all three models. This is similar to the 59 fs timescale for localization observed in the study by Yeh et. al., which was attributed to the preferential solvation of the localized state.[126] This conjecture is supported in the simulation results as the excited state localized model is preferentially solvated by the bath by –8.4 kcal/mol compared to the delocalized state. We also addressed the issue of the presence of a counterion in these simulations. Shown in Figure 7.3 are the equilibrium solvent responses to the $[Ru(bpy)_3]^{2+}$ chromophore with and without a single PF_6^- counterion. Overall, the effect of the counterion is to restrict the solvent's response to $[Ru(bpy)_3]^{2+}$ by constraining to the system. This is supported by the strong solvent structure about PF_6^- as well as the fact that the counterion located itself as far from $[Ru(bpy)_3]^{2+}$ as the simulation would allow.

While these results are in excellent agreement with the experimental findings, there are a few issues that these methods do not allow us to address. First, the ruthenium atom has diffuse d–orbitals which increases the covalency of $[Ru(bpy)_3]^{2+}$. Consequently, a fully ionic charge transfer model is not a realistic representation of the excited states and our results are likely overestimated. Further, the process of electron localization is more complicated than can be properly described by the equilibrium solvent response of such a simple model. In order to resolve these issues, we decided to try to improve our methods to provide a more accurate description of the excited states.

The first way to improve our simulations was to create a better model for the lowest excited states. To this end, a method is needed to calculate the properties of the

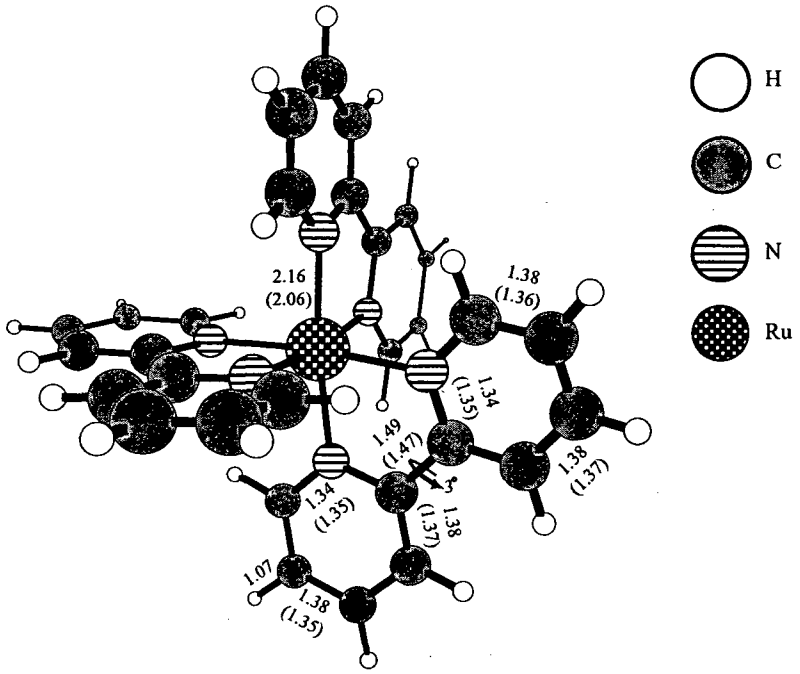

Figure 7.3 The optimized Hartree–Fock geometry of $[Ru(bpy)_3]^{2+}$ at the ground state. Relevant geometric parameters are marked in the figure and are summarized in Table 1. Experimental results are in parentheses and are from ref. 45.

ground and excited states at the Frank–Condon as well as the optimized excited state geometries. While Time Dependent DFT (TDDFT) is the best method given the size of the molecule, Configuration Interaction with Single excitations (CIS)[138,139] was used to calculate the electrostatic properties and optimized geometries of the excited states. This was done since the properties of excited molecules can not be calculated with TDDFT in the Gaussian '98 suite of packages. For computational feasibility, the active spaces of these CIS geometry optimization calculations were reduced to all the occupied valence orbitals in addition to an equal number of virtual orbitals. The geometry of the ^1A ground state of the molecule was optimized at the Hartree–Fock level of theory. This

species	bpy[o,a] [$N_{1,2}$–Ru (Å)]	bpy[o,a] [$N_{1,2}$–Ru (Å)]	bpy[o,a] [$N_{1,2}$–Ru (Å)]
[b,1]A	3 [2.16, 2.16]	3 [2.16, 2.16]	3 [2.16, 2.16]
Singlet 1	12 [2.39, 2.39]	5 [2.16, 2.29]	5 [2.16, 2.29]
Singlet 2	11 [2.24, 2.41]	11 [2.24, 2.41]	1 [2.19, 2.19]
Triplet 1	12 [2.33, 2.46]	9 [2.18, 2.37]	1 [2.16, 2.23]
Triplet 2	12 [2.22, 2.47]	12 [2.22, 2.47]	0 [2.17, 2.17]

a. The angle of the pyridine subunits about the conjoining bond.
b. Data for the electronic ground state.

Table 7.2. The relevant optimized geometric parameters of the ground and lowest (initially degenerate) singlet and (initially degenerate) triplet excited states of $[Ru(bpy)_3]^{2+}$.

was used as the reference ground state theory as CIS theory is the analog of Hartree–Fock theory for excited states.

The Hartree–Fock optimized geometry of the ^1A ground state of the D_3 symmetric $[Ru(bpy)_3]^{2+}$ is shown in Figure 7.3. The properties of the lowest excited degenerate singlet and triplet states were calculated at this ground state (Frank–Condon) geometry. For the singlet states, the transition moments are non–degenerate and that both excited singlet states have dipole moments of 0.19 D at the Frank–Condon region. The triplet states each have dipole moments of 0.22 D. Based upon the Mulliken population analysis, charge is removed from the metal center and added to the pyridine ligands, confirming the metal to ligand charge transfer character for the lowest ^1E and ^3E states in the Frank–Condon region.

ΔE[a] Excited State (wavelength/ nm)	Experiment[b] (nm)
^{3}E (639)	
^{3}A (621)	
^{1}E (463)	532
^{3}E (461)	474
^{1}A (456)	457
^{3}? (443)	422
^{3}E (391)	395
^{3}? (391)	
^{3}? (323)	
^{1}E (303)	290
^{1}? (290)	
^{1}E (226)	

a. Not all of the symmetries of the excited states were determinable.
b. Experimental results from ref. 143.

Table 7.3. The singlet and triplet UV/VIS spectra of $[Ru(bpy)_3]^{2+}$ at the ground state geometry.

ΔE (nm) singlet state 1	ΔE (nm) singlet state 2	ΔE (nm) triplet state 1	ΔE (nm) triplet state 2
881[a]	792[a]	2169[a]	2444[a]
2287	47322	5786	14586
2248	1659	1971	1843
698	987	1111	1038
676	590	783	669
517	558	715	630
303	315	474	464
301	311	471	457 / 457
296	308	467	369 / 369
		376 / 376	368
		375	

a. Fluorescent (phosphorescent) transitions from the optimized excited state to ground state.

Table 7.4. The spin allowed spectra of the first degenerate excited singlet and triplet states at their individual optimized geometries.

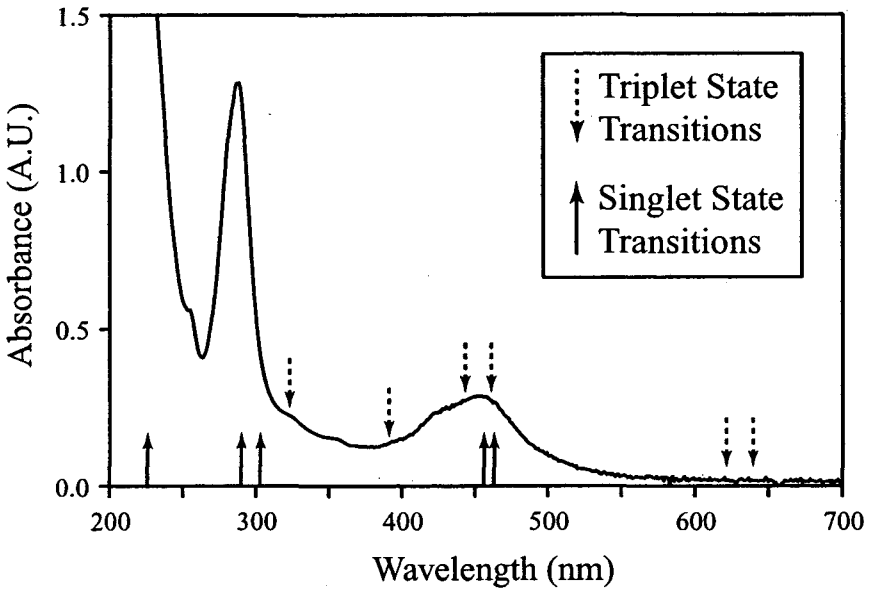

Figure 7.4 The calculated and observed UV/Vis spectra of $[Ru(bpy)_3]^{2+}$. Experimental results are for $[Ru(bpy)_3]^{2+}$ in butyronitrile solution. Singlet spin allowed absorptions are shown by upward arrows and triplet excited state energies are shown by downward pointing arrows.

The geometries of the excited states were optimized at the CIS level of theory as well. The lowest excited singlet and triplet states break symmetry from D_3 point group of the ground state to form C_2 symmetric structures. The degeneracies of the lowest excited states are split as a result. The optimized geometry of the first excited singlet state has a bipyridine ligand twisted about the conjoining bond of the pyridine subunits by an angle of 12°. The other bipyridine ligands are nearly planar with pyridine subunit twist angles of 5°, which is close to the ground state value of 3°. The second excited singlet state has one near planar bipyridine ligand while the other two ligands have pyridine subunit twists of 11°. The relaxation of the geometry from the Frank–Condon

region stabilizes the first excited singlet state by −18.8 kcal/mol while the second excited singlet state is lowered in energy by −15.8 kcal/mol. When the geometries of the singlet excited states are allowed to relax, the net dipole increases to 0.98 D for the first excited degenerate singlet state and 0.77 D for the second. The increase in dipole moment is accompanied by a return of charge density to the metal center from the bpy ligands, which reduces that the MLCT character of these states. The relevant geometric parameters the of the optimized ground state and excited state geometries of $[Ru(bpy)_3]^{2+}$ are also summarized in Table 7.2.

The degenerate lowest excited triplet states have dipole moments of 1.01 D and 0.99 D for the first and second excited singlet degenerate states, respectively, at their optimized geometries. The first triplet state has two bipyridine ligands with twist angles of 12° and 9°, while the second degenerate triplet state also has two twisted bipyridine ligands. As was observed for the singlet states, these is a return of charge density to the metal center from the bpy ligands as the molecular geometry relaxes to equilibrium. These results are also summarized in Table 7.2. The full set of geometry coordinates for all states may be obtained directly from the Harris Group data archives.

Once the geometries of the ground and lowest excited state intermediates were optimized, the molecular properties and UV/VIS absorption spectra of all $[Ru(bpy)_3]^{2+}$ species were calculated using the full CIS active space with the 6–31G basis set for the first and second row atoms.[40] The results of the Mulliken population analysis were used to generate models acceptable for MD simulations, as discussed above.[140] Shown in Figure 7.4 are the calculated gas phase electronic transitions of $[Ru(bpy)_3]^{2+}$ at the optimized ground state geometry superimposed with the experimental UV/VIS

Transition[a]	ΔE (kcal/mol)[b]
$\Delta E^{(1)}_{vert\rightarrow opt}$	-1.20 ± 0.03
$\Delta E^{(2)}_{vert\rightarrow opt}$	-1.13 ± 0.05
$\Delta E^{(1\rightarrow 2)}_{vert}$	0.00 ± 0.00
$\Delta E^{(1\rightarrow 2)}_{opt}$	0.05 ± 0.03

a. See text for details.
b. A negative ΔE represents energetically favorable transition.

Table 7.5. The solvation free energy differences between various excited states at their Frank–Condon and optimized geometries as determined from MD based thermodynamic integration.

spectrum in butyronitrile solution. The spin allowed singlet transitions, as well as triplet state excitations, are represented by the solid and dashed arrows of Fig. 7.4, respectively. These results are summarized in Table 7.3 along with the experimental values from ref. 144. Also reported in Table 7.4 are the calculated spin allowed absorption transitions of the lowest excited singlet and triplet states at their respective optimized geometries. Overall, the calculated ground and excited state absorption spectra correlate well with the previous experimental results as discussed below.

We previously calculated the differences of the solvation energies between our model localized and delocalized states by averaging the calculated solvent / solute interaction energy over several hundred picoseconds. However, it is difficult to accurately determine such differences due to the large standard variance in the solvent / solute potential. In order to improve the relative free energy calculation between excited state species, we turned to thermodynamic integration techniques.[141] This method measures the relative free energy differences between species A and B by evaluating:

(1) $E_a - E_b = \Delta E = -RT \ln \langle \exp(-\Delta H/RT) \rangle_A$

where ΔH refers to the difference between the solution phase expectation value for Hamiltonians of species A and B. While (1) is suitable for evaluating the energy differences between similar species, we have used the thermodynamic integration (slow growth) method in which (1) is calculated by summation along a coupling parameter λ. The Hamiltonian is redefined using the λ coupling parameter as:

$H(\lambda) = \lambda H_B + (1-\lambda) H_A$

and (1) is evaluated as:

$$(2) \quad \sum_{\lambda=0}^{\lambda=1} (H_{n+1} - H_n)$$

A single topology method has been employed using a total of 10 windows to calculate (2). Each measurement window was preceded by 2.5 ps of equilibration followed by 25 ps of MD simulation. The error of this process has been calculated by forward and backward simulations and by construction of appropriate thermodynamic cycles. Due to the long simulation times, the NVT ensemble was used to avoid energy drift that is inherent due to integration errors in the NVE ensemble.

There are four models which have been developed from our ab initio results. First, the solvent / solute free energy difference of either the first or second degenerate excited singlet state at the Frank–Condon region versus the same state at its optimized geometry has been calculated using (2). We have designated these transitions as $\Delta E^{(1or2)}_{vert\rightarrow opt}$ which represents the solvation free energy difference between the vertical (Frank–Condon) and optimized models of the first or second state of the lowest degenerate singlet excited states. The energy difference (2) has thus been evaluated for $\Delta E^{(1)}_{vert\rightarrow opt}$, $\Delta E^{(2)}_{vert\rightarrow opt}$, $\Delta E^{(1\rightarrow 2)}_{vert}$, and $\Delta E^{(1\rightarrow 2)}_{opt}$. This provides a model for the measurement of the solvation energy differences of an excited state at the initially formed Frank–Condon region versus the same species at the bottom of its electronic potential.

The summary of molecular dynamics results are given in Table 7.5. In the Frank–Condon region, the solvent / solute free energy difference between the first two degenerate singlet excited states is equal. As the geometry of the first excited state is relaxed, the solvation free energy decreases by -1.20 ± 0.03 kcal/mol. The optimized second state has more favorable solvent / solute interactions at the optimized geometry versus the Frank–Condon region by -1.13 ± 0.05 kcal/mol. The first optimized singlet excited state with the more localized change in electron density appears to have more favorable interactions with the solvent by 0.05 ± 0.03 kcal/mol compared to the second excited singlet state. Overall, the free energy of solvation is correlated with the magnitude of the dipole moment of the excited state.

Section 7.3. Discussion

The results presented in this chapter are twofold. The first set of ab initio results have clarified many of the issues concerning the electronic structure (and thus the UV/Vis absorption spectrum) of the excited states of $[Ru(bpy)_3]^{2+}$. The microscopic details of the lowest energy singlet and triplet excited states also have been revealed. To the CIS level of theory, these findings have shown that the initial electronic transitions from the ground state to the excited states that comprise the lowest lying ^1E term involve metal to ligand charge transfer. The excess electron density appears to be associated with the nitrogen sites of the bipyridine ligands. As the geometry is allowed to relax to equilibrium, the difference in charge density becomes more localized and the MLCT character of the excited state is diminished. The degree to which the excited states are preferentially solvated in acetonitrile has been determined from the MD data. These results are useful for understanding the magnitude of the solvent driving force for the formation of localized electron density in an excited inorganic chromophore.

A. The ab initio excitation energies of $[Ru(bpy)_3]^{2+}$. The electronic structure of $[Ru(bpy)_3]^{2+}$ in the ground state geometry has been previously studied using a variety of techniques.[124,128,134,142,143] The results of the present study agree with the previous work in that the ground state has been found to have a D_3 symmetric geometry with a singlet ^1A electronic ground state. The lowest energy occupied states are largely metal d–type and ligand π bonding in character while the lowest unoccupied orbitals are ligand π^* centered. It is likely that the photophysical properties of $[Ru(bpy)_3]^{2+}$ are poorly described by considering single electron excitation configurations between individual occupied and unoccupied molecular orbitals. This is evident from the

expansion of the CIS excited state wavefunction, for which the LUMO ← HOMO transition has an insignificant weight in the lowest excited states.

The transition energies from the ground to the excited states of $[Ru(bpy)_3]^{2+}$ have been calculated at the CIS level of theory. The CIS method is more flexible than some of the previously employed theoretical models as the excited state wavefunctions are constructed from linear combinations of *all* possible one–electron excitation configurations. Overall, the calculated spin allowed UV/Vis excitation energies are in excellent agreement with the experimental data as shown in Figure 7.4 and summarized in Table 7.3. The calculations show a total of 5 non–overlapping absorptions occurring in the 400 nm–500 nm range, as has been observed in previous circular dichroic experiments.[144] Absorption in the visible region is dominated by spin allowed transitions to states of ^1E and ^1A symmetry as has been proposed in previous experimental and theoretical studies.[145–147] The near UV region is also well described in our calculations. It has been proposed that two overlapping transitions are responsible for the intense 290 nm absorption of $[Ru(bpy)_3]^{2+}$,[145,146] as observed in our present results. The excited state energies for the triplet states are not in such good agreement, however. The low energy shoulder of the $^1E \leftarrow {}^1A$ transition around 500 nm is thought to be due to excitation into the lowest triplet state, which agrees with the fact that the luminescence spectrum has a maximum around 625nm. Consequently, the calculated value for excitation to the lowest excited triplet state is not in agreement with these experimental results.

The spin allowed UV/VIS absorption spectra of the transient excited species at their individual optimized geometries have also been calculated and are summarized in

Table 7.3. The calculated absorption spectra of the long lived triplet excited states are in excellent agreement with previous experimental results. The CIS results predict several spin allowed triplet absorptions in the 376–369 and 474–457 nm range, which are comparable to the experimental results of 360 nm and 430 nm.[148] The calculations also predict red visible and near–IR absorptions for the transient high spin species which have been observed in femtosecond studies using similar compounds.[149] The present results have provided a basis for the underlying factors responsible for the ~4000 cm^{-1} intra–valence charge transfer (IVCT) absorptions observed in the reduced $[Ru(bpy)_3]^+$ spectrum.[150] As the lowest ^3E MLCT excited states are allowed to relax into equilibrium, the reduction of symmetry causes the degenerate orthogonal states to split into a set of closely spaced excited states. This splitting of the formerly degenerate states is responsible for the low energy absorption due to electron transfer between bpy ligands. Note that at the optimized excited triplet state geometries the correlation of the calculated phosphorescence transition from the excited triplet states to the ground singlet state (~7000 cm^{-1}) results is poor when compared to experiment (16,000 cm^{-1}).[127] This discrepancy between experiment and theory may be due to the differences in the spectrum in the gas phase vs. solution phase, the influence of Frank–Condon factors, as well as the ~1 eV error inherent in the CIS method. Based upon these results, we conclude that the CIS method is best at calculating spin allowed spectra.

B. The ab initio optimized geometries of the ground and excited states of $[Ru(bpy)_3]^{2+}$. The properties of the two singlet degenerate excited states belonging to the lowest energy ^1E term were calculated at the ^1A ground state (Frank–Condon) geometry. Based upon the Mulliken population analysis, electron density is removed

from the metal center and is added to the three bipyridine ligands. The excess charge density appears to be associated with the nitrogen sites of the ligands, although there are slight differences between the first and second degenerate singlet states. In the first excited state, the excess charge density is preferentially associated with the trans nitrogen sites of two bipyridine ligand. The second ^1E excited state has the excess electron density associated with nitrogen sites in an orthogonal plane. As discussed below, the change in the charge density becomes more localized as the geometries of the excited states are allowed to relax. These degenerate excited singlet states have moderate dipole moments, which coupled with their non–degenerate transition moment vectors (x or y, respectively) and optimized C_2 symmetries suggests localized excited states.

Upon geometry optimization of the first and second singlet excited states, the molecule energetically relaxes by ~20 kcal/mol by breaking the D_3 symmetry of the ground state and form C_2 symmetric structures. As the geometry relaxes, electron density is returned to the metal center with a corresponding removal of electron density from bpy ligands, which reduces the MLCT character of these states. At the minimum of the first singlet potential, the change in charge density from the ground state to the excited state is localized between the metal center and a single bpy ligand. The second optimized singlet state has the charge density differences associated with the metal center and two bpy ligands, specifically at nitrogen sites which are trans to eachother. This relaxation to lower symmetry structures and localization of the difference in charge density supports the concept that electron localization in $[Ru(bpy)_3]^{2+}$ is intrinsically favorable.[151] In the first degenerate excited singlet state, a single bipyridine ligand partially dissociates and twists about the conjoining pyridine subunit bond by ~12°. This

increase in the twist angle mirrors that of a local minimum of a free bipyridine molecule, which has a 44° pyridine group twist angle calculated at the same level of theory. With the increased bond length of the N–Ru bond distances of the twisted ligand and the coupled increase in electron density at the metal center, these results suggest that the ligand partially dissociates in the excited state which allows electron density to be returned to the charge deficient Ru atom. The results for the second excited singlet state are similar except for the fact that two bipyridine ligands are partially dissociated while the third ligand remains bound in a planar configuration. The structural reorganization results in the increase of the dipole moment for both states, while the largest increase in the dipole is associated with the first singlet excited state. As will be shown from the MD results, a polar solvent preferentially solvates the first (most localized) singlet excited state.

The properties of the lowest energy triplet states are strikingly similar to the lowest energy singlet states. The optimized geometries break symmetry of the ^{1}A ground state and the optimized structure has increased electron density at the metal center compared to the same state in the Frank–Condon region. The bpy ligands are partially dissociated and the net dipole moment increases beyond that observed in the singlet states.

C. Solvent / Solute Interactions. As it has been suggested that electron localization occurs in the excited singlet state,[125] we have used models of the first excited singlet states to examine the details of solvent / solute interactions. The interaction of the model excited states with the polar acetonitrile solvent has been evaluated using thermodynamic integration, assuming that the solvent has time to fully

respond to the formation of the excited state. At first, we believed that this assumption was justified given the ~60 fs timescale of acetonitrile solvent response,[152] and the previous observation that intersystem crossing occurs within 100 – 300 fs based upon triplet absorptivity data.[125,126] A recent result based upon direct observation of singlet state fluorescence has shown that the ISC timescale is 40 ± 15 fs.[127] Along such a short timescale, an excited singlet state would not likely thermalize and the solvent would not have fully responded to the system.

Although the excited singlet state does not exist for long enough to become fully solvated, the difference in the excited state models at the Frank–Condon and optimized geometries will reflect the solvent effect on excess charge localization. As the ISC timescale is very short, it would be better to use the triplet state manifold to model the solvation energetics of localization. As we have found that the excited singlet and triplet properties are very similar, the excited singlet state calculations should have some bearing on the photophysics of $[Ru(bpy)_3]^{2+}$.

In the Frank–Condon region both singlet excited states have moderate dipole moments and are thus have equal interaction with the polar acetonitrile solvent ($\Delta E^{1\rightarrow 2}_{vert}$ =0.00 ± 0.00 kcal/mol) The fact that the dipole moment increases as the geometry of the excited states relaxes is reflected in the MD results. The calculated value for $\Delta E^{1}_{vert\rightarrow opt}$ is −1.20 ± 0.03 kcal/mol while $\Delta E^{2}_{vert\rightarrow opt}$ is −1.13 ± 0.05 kcal/mol, which shows that the more polar molecule with the electron density localized on one bipyridine ligand is the overall most stabilized molecule energetically. The preferential solvation of the more local state is confirmed by the $\Delta E^{1\rightarrow 2}_{opt}$ calculation results of 0.05 ± 0.03 kcal/mol.

The excited state dipole moment of $[Ru(bpy)_3]^{2+}$ in the first excited singlet state has been previously measured by Kober et. al. to be 14.1 ± 6.1 D,[153] and by Oh and Boxer to be (8.8 ± 0.7)/f D.[147] These results indicate that our model has underestimated the solution phase dipole moment due to the lack of solvent polarization effects in the excited state calculations, as the present results are applicable to the gas phase molecule. Nonetheless, the difference in the dipole moment from the Frank–Condon region to the excited state minima may represent a meaningful quantity. Preliminary calculations using a point charge and dipole model has shown that the system responds linearly to the change in magnitude of the dipole moment even with a large (~8 D) starting dipole moment. We will also take into account the solvent polarization in a future model, as discussed below.

Unfortunately, there are still technical issues that must be addressed. For one, ab initio calculations of this type are prone to an artifactual symmetry breaking phenomena.[154] Symmetry breaking will result in artificially larger dipole moments and a reduction of symmetry when optimizing geometries. While some of the calculated ground state wavefunctions had broken symmetry, the addition of symmetry constraints to the scf optimization procedure produced identical results to unconstrained calculations. Thus, it would appear that the presence of artifactual symmetry breaking in some of our calculations does not alter our results to any significant extent. Another issue that should be addressed is whether the present level of theory is sufficient to describe multibody effects which may be responsible for the coupling of the bipyridine ligands via the metal center in the excited state. A method that might account for such interactions is a configuration interaction model which includes simultaneous multiple excitations in the

ligand system and the metal. Unfortunately, the ab initio methods employed in the present study do not allow for this type of electron correlation and such a level of theory is unobtainable for such a large molecule as $[Ru(bpy)_3]^{2+}$. In order to address these issues, we plan to alter our theoretical models to allow for electron correlation, include solvent effects and reduce the influence of symmetry breaking. As it has been shown that the singlet excited state has a very short lifetime, we plan to model the excited state entirely as the high spin species. As such, we may use ground state methods to calculate the properties and geometries of the ground and lowest triplet excited states. We will also include solvent continuum models and can account for electron correlation by using DFT methods. The BLYP functional will be used as this level of theory is not as susceptible to symmetry breaking as other methods. Unfortunately, these studies will not be completed in time to be include in this chapter.

Section 7.4. Conclusion

We have shown that to the CIS level of theory the lowest gas phase excited states of $[Ru(bpy)_3]^{2+}$ may be described as intrinsically localized charge transfer states. Upon absorption of a photon into the Frank–Condon region, the molecule has a small dipole moment in both of the lowest singlet degenerate states. Upon relaxation in the excited state manifold, the excited state breaks symmetry to form C_2 symmetric structures. The electron density that was donated to the ligands in the Frank–Condon region returns to the metal as well, thus diminishing the MLCT character of these states. The relaxation of the geometry and greater localization of the charge density increases the dipole moment in the excited states to ~1 D. In a polar solvent, the localization is energetically favorable

by ~1 kcal/mol. Consequently, the preference for localized charge transfer states may be interpreted as the preferential interaction of polar solutes with polar solvents. This relaxation energy is likely underestimated due to the lack of inclusion of solvent polarization effects in the excited state calculation, which will increase the dipole moment and increase the magnitude of the solvent / solute interaction. A future method has been proposed which will account for some of the discrepancies noted in the present study.

Chapter 8

Simulations of the Solvated Electron in Low Temperature Matrices, in Gas Clusters and at a Surface Interface

Although identified in 1908,[155] the dynamics of the excess electron in solution is still the subject of numerous experimental,[156–161] as well as theoretical[162–165] investigations. This is a result of the fact that the excess electron is the best solute to study solvation dynamics due to the lack of internal degrees of freedom. Our group and others have made significant advances in the study of the solvated electron at low temperature surface interfaces.[166–168] Extending the understanding of solvated electron dynamics developed from bulk systems to those of reduced dimensionality is of clear interest given the many processes that occur in quasi–two dimensional environments, such as electron transfer in electrochemistry and in molecular electronic devices. The interfacial bath with which the excess electron interacts may have distinct physical differences from the bulk due to the intrinsic asymmetry of the environment. The interfacial potential may alter the equilibrium structure of an adsorbate layer and hinder certain molecular motions compared to the isotropic bulk. In order to expand our knowledge of the dynamics of the excess electron, our group developed the programming capacity in order to simulate this species using previously published models. These theoretical studies have provided a detailed microscopic understanding of the solvated electron in low temperature and low dimensional media.

This chapter is outlined as follows. First, an introduction to the methods are provided in Sec. 8.1. The methods to calculate the wavefunction of the electron is provided in Sec. 8.2, while the models for the solute–solvent potential (as well as solvent–solvent and solvent–surface interactions) are described in Sec. 8.3. The results and conclusions of this work are given in Sec. 8.4. The molecular dynamics program uses standard algorithms and will not be published here, however the wavefunction calculation program is given in the Appendix.

Section 8.1 Introduction

Simulations involving an excess electron must be treated using methods firmly based on quantum mechanical principals due to the low mass of the particle. The low mass and a moderate kinetic energy results in the electron having a deBroglie wavelength which is significant on a molecular length scale. Likewise, due to the relatively heavy mass of a molecule such as methanol, a classical description is sufficient. Consequently, a mixed quantum / classical treatment is sufficient to simulate the interaction of an excess electron with a methanol solvent bath. All that is needed is a pseudopotential to describe the solute / solvent interactions and a method to solve the Schrödinger wave equation for the excess electron. The coupling of the excess electron to the solvent (i.e. the force the solvent feels from the excess electron) is calculated via the Hellman–Feynman Theorem as discussed below.

In 1993 Zhu and Cukier developed a potential to describe an electron's interaction with a methanol molecule,[169] the exact form of which is discussed in Sec. 8.2. These authors used the split operator method of Feit and Steiger to calculate the wavefunction of the excess electron given a pre–defined potential energy surface.[170–

172] The electron was assumed to respond adiabatically to the instantaneous solvent configuration, which is a valid assumption given the large energetic splitting between the ground and excited states. The solvent configuration is then updated and a dynamical trajectory for the electron properties may thus be calculated. This model has been applied successfully by a number of authors in studies of excess electrons in methanol.[173,174] Once we had verified that our model was working correctly by reproducing previous results, we extended our model to characterize the excess electron in low temperature glassy methanol, in a gas phase cluster and at a Pt(100) surface interface as discussed below.

Overall the simulations work as follows. Given a valid configuration of a methanol bath, the potential that a single electron would experience at every point on a 16×16×16 3–dimensional grid inside of a finite volume of the configuration is calculated. The spacing of the grid points is on the order of a Bohr and the potential energy is calculated by using the model of Zhu and Cukier. Once the potential is known, then the wavefunction is calculated using an initial guess generated from a previous simulation. The equation of motion of methanol may then be calculated by solving:

$$M_i \frac{d\mathrm{R}_i}{dt^2} = \frac{dV_{nn}(\mathrm{R}^\mathrm{N})}{d\mathrm{R}_i} - \int dr\,|\Psi(\mathrm{r},\mathrm{R}^\mathrm{N},t)|^2 \frac{dV_{ep}(\mathrm{r},\mathrm{R}^\mathrm{N})}{d\mathrm{R}_i}$$

were M_i is the mass of a solvent site, R_i is the solvent site coordinates, R^N represent all the solvent site coordinates, V_{nn} is the methanol–methanol potential and V_{ep} is the methanol–electron pseudopotential. The first term on the right hand side is the classical force and the second term is the quantum force from application of the Hellman–Feynman theorem.[175,176] The force that the bath experiences from the quantum mechanical electron can be essentially determined by the (negative) derivative of the

potential weighted by the amount of normalized charge $\Psi(x,y,z)^2$ at each point on the grid. The coordinates of the solvent are advanced and the process is repeated for the length of the simulation.

Section 8.2 The Split Operator Method

The evolution of a wavefunction may be propagated in time by the application of the Schröedinger equation:

$$d|\ \Psi(p,x,t+\Delta t)\ >/dt = -i\,\mathrm{H}(\mathbf{p},\mathbf{x})\,|\ \Psi(p,x,t)\ > \qquad (1)$$

where $\mathrm{H}(p,x) = \ -\nabla^2/2\cdot m + V(x)$

For a time–independent Hamiltonian reduces to the application of the operator:

$$|\ \Psi(p,x,t+\Delta t)\ >/dt = \ e^{-i\cdot\Delta t\cdot(\nabla^2/2\cdot m+V(x))}\ |\ \Psi(p,x,t+\Delta t)\ > \qquad (2)$$

for a discretized time period Δt of a mass m particle.

The time evolution operator $e^{-i\cdot\Delta t\cdot \mathrm{H}(p,x)}$ is difficult to apply due to the fact that ∇^2 is diagonal in momentum space and V(x) is diagonal in real space. This problem is circumvented by using the split operator method in which the time evolution of a wavefunction over a finite time step of Δt may be written as [170–172]:

$$\Psi(\mathbf{x},t+\Delta t) = e^{i\cdot\Delta t\cdot\nabla^2/4\cdot m}\cdot e^{-i\cdot\Delta t\cdot V(x)}\cdot e^{i\cdot\Delta t\cdot\nabla^2/4\cdot m}\cdot\Psi(\mathbf{x},t) \qquad (3)$$

This partitioning of the time evolution operator has an inherent commutation error proportional to Δt^3. The kinetic operation: $e^{i\cdot\Delta t\cdot\nabla^2/4\cdot m}$ is equivalent to a free particle propagation over a half a timestep. The potential operator: $e^{-i\cdot\Delta t\cdot V(x)}$ results in a phase change due to the action over a whole timestep, which followed by another kinetic operation. Unfortunately, the kinetic operation is not local in position, which makes a tractable (i.e. analytic) expression impossible. However, by making two

resolutions of the identity (first in **x**, then in **p**) and then rearranging the summation, the first step becomes a Fourier transformation of the spatial wavefunction to **p** space. Thus the resulting wavefunction becomes diagonal in momentum. As a consequence of the need for Fourier transformation, the wavefunction must be discretized over a certain length L_0 divided into (L_0 / δl) segments. The computational difficulty of calculating the nonlocal kinetic operator is thus traded for the expense of fast Fourier transformation of the discretized wavefunction.

The split operator method may be summarized as follows: the first step is to generate a starting, normalized spatial wavefunction. This initial wavefunction does not need to correspond to any particular eigenvector of the model potential. This wavefunction is then transformed to **p**–space by fast Fourier transform. After transformation, the wavefunction is altered over a half timestep by application of the kinetic operator: $e^{i\cdot\Delta t\cdot \mathbf{p}^2/4\cdot m}\Psi(\mathbf{p},t)$. Practically, in momentum space the real and imaginary values of the wavefunction are multiplied by $\cos(\Delta t\cdot\mathbf{p}^2/4\cdot m)$ and $\sin(\Delta t\cdot\mathbf{p}^2/4\cdot m)$, respectively. The propagated wavefunction is then Fourier transformed back into real space upon which the potential operator $e^{-i\cdot\Delta t\cdot V(\mathbf{x})}$ is applied. This process is repeated N times until the wavefunction has been propagated over the desired total time $\tau=N\Delta t$.

While the split operator is a useful method for calculating the time evolution of any arbitrary initial wavefunction, one is often more interested in the eigenvalues and eigenstates of a given Hamiltonian. Fortunately, the split operator method is amenable to the task. First, as any arbitrary wavefunction may be expanded in the space of the

eigenstates of the Hamiltonian, the time dependent wavefunction may be written as follows:

$$\Psi(t)=\sum_n A_n \Omega_n e^{-i\cdot E_n\cdot t} \tag{5}$$

Where Ω_n represent the nth eigenstate, E_n the nth eigenvalue, and A_n the contribution of that state to the initial wavefunction.

Now define a complex overlap correlation function P such that:

$$P(t)=\langle \Psi(\mathbf{p},\mathbf{x},t)|\Psi(\mathbf{p},\mathbf{x},0)\rangle \tag{6}$$

Using the expansion in (5) and the orthonormality of the eigenstates the result is:

$$P(t)=\sum_n |A_n|^2\cdot e^{(-i\cdot E_n\cdot t)} \tag{7}$$

Fourier transformation of this correlation function then gives:

$$P(E)=\sum_n |A_n|^2\cdot \delta(E-E_n) \tag{8}$$

Thus eigenvalues appear as peaks in the absolute value of the Fourier transform of the complex time correlation function of the overlap trajectory. This is why this type of calculation has been labeled as a spectral method. Now that the eigenvalues are known, the corresponding eigenfunctions may also be calculated. First take the expression:

$$\int_0^\tau e^{i\cdot E_\alpha\cdot t}\cdot \Psi(t)\cdot dt \tag{9}$$

which after insertion of the expansion of the wavefunction (5) this becomes:

$$\int_0^\tau \sum_n \Omega_n e^{i\cdot(E_\alpha-E_n)\cdot t}\cdot dt \tag{10}$$

Of this expression, only the eigenstate $\Omega_{n=\alpha}$ for which $E_n - E_\alpha = 0$ is not removed during the evaluation of the integral through deconstructive interference from a

finite $e^{i\cdot(E_n-E_0)\cdot t}$ term. As a matter of practical consideration, in order to calculate any arbitrary eigenvalue / eigenstate of the Hamiltonian, that state must contribute to some degree to the initial wavefunction. Further, calculation of both the eigenvalues and eigenstates requires knowledge of both the overlap correlation function as well as the actual wavefunction trajectory itself. Thus either the trajectory needs to be calculated twice or the trajectory must be saved to disk in order to evaluate eq. 9. In the case of the solvated electron, the ground state is the state of interest and only the ground state eigenvalue (or binding energy) and eigenfunction are calculated in the course of these simulations. A copy of the program that calculates the wavefunction is given in the Appendix.

Section 8.3 Simulation Details

A. The Methanol–Excess Electron Pseudopotential In 1993, Zhu and Cukier derived a pseudopotential to describe the energetics of a single methanol molecule with an excess electron.[169] Basically, the potential may be broken down as:

$$V(r)=V^{el}(r)+V^{p}(r)+V^{r}(r)+V^{ex}(r) \qquad (11)$$

which describes the electronic, polarization, repulsion and exchange contributions to the total energy. The electrostatic potential is the Coulomb potential and is calculated as:

$$-\Sigma\, q_i e/\max(r_{ei}, r_{cut}) \qquad (12)$$

where r_{ei} is the electron / site radial distance, e is an electron charge, and the max function is used to prevent singularities with a cutoff distance of r_{cut}=0.5 bohr. The polarization energy is calculated via

$$-\Sigma(1-\exp[(-r/r_o)^6])\, \alpha_i e^2/(2r_{ei}^4) \qquad (13)$$

where α_i is the site polarizability and $(1-\exp[(-r/r_o)^6])$ is a switching function used to exclude the space of the atomic core and used a cutoff of ro=1.9 bohr. The repulsion potential is derived from the Pauli exclusion principal and is calculated from

$$(e^2/2a_o)\ \Sigma\ [3\pi^2\rho_i(r_{ei})]^{2/3} \qquad (14)$$

where $\rho_i(r_{ei})$ is the electron density at site i and is given by

$$n_i(r_{ei}/a_o)^z \exp(-3r_{ei}/a_o) \qquad (15)$$

The final term in the potential is from Slater's exchange potential and is calculated from

$$-\gamma e^2/a_o[(3/\pi)\ \rho_i(r_{ei})]^{1/3} \qquad (16)$$

The parameters for the potential are given in Table 8.1.

	q_i/e	$\alpha_i/Å^3$	n_i	z_i	σ_{ij}/ Å	ε_{ij}/k_b
H	0.431	0.0	1	0	0.0	0.0
O	−0.728	1.44	8	0	3.083	87.94
CH_3	0.297	1.7	6	1	3.861	91.15

Table 8.1 The simulation parameters used for the solvent and solvent / electron potential.

As it is impossible to simulate a large enough system such that long range potentials are adequately described within the spatial cutoff, and as such these long range correction factors may be estimated using standard techniques. The Ewald summation technique has been employed in order to calculate the coulomb potentials and forces. [177] While summations that scale as 1/r or $1/r^2$ are normally divergent, the Ewald summation is able to converge to a solution by partitioning the electrostatic potentials and forces between real and reciprocal spatial contributions. For potentials that are convergent, the formula for long range corrections may be estimated from [12]:

$$V_{lrc} = 4 \cdot \pi \cdot \rho \int_{rc}^{\infty} r^2 \mathrm{V}(r) \cdot g(r)\, dr \qquad (17)$$

where *rc* is the cutoff used in the simulations for the potential V(r), typically half of the simulation box length, and ρ is the number density. The usual assumption is that at large enough length scales, the radial distribution function has no structure and is equal to unity. The long range correction may then be applied via simple numeric integration of eq. 17 with g(r)=1. The long range correction for the polarization potential is –0.35 eV for the room temperature results and –0.43 eV for the glassy simulations. The long range corrections for the other terms in Zhu and Cukier pseudopotential are negligible, as are the polarization potentials for surface simulations.

B. The Methanol–Pt(100) Potential In order to describe the interaction of an electron in a 2–D media, a second potential is needed to describe the interaction of a methanol molecule with a surface. Previous studies of water on a Pt(100) surface have been conducted using an empirically derived potential,[178,179] and the same methodology has been employed to derive a methanol / Pt(100) 2–D interfacial interaction model. Density Functional Theory (DFT) calculations were performed for a single methanol molecule and a cluster of 5 singlet platinum atoms in an optimized pyramid geometry. The Jaguar program was used to calculate the optimized geometries at the B3LYP level of theory using the LANL2DZ basis set and effective core potentials for Pt and the 6–31G** basis set for H, O and C. The oxygen atom of the methanol molecule was constrained to be at the center, bridge and top positions of an optimized cluster of 5 singlet Pt atoms. The remaining geometric parameters were then optimized and all the calculated geometries were used to minimize the parameters of a methanol–Pt(100) potential. Unfortunately, the sheer number of parameters prevented the accurate

minimization to a physically meaningful potential for all the methanol (H, O, and CH_3) sites, and as such a different approach was necessary. The problem with fitting was resolved by directly employing the H–Pt(100) potential of Berkowitz and by solving for the CH_3/Pt(100) potential by optimizing the geometries of several configurations of CH_4 with the platinum cluster. These results were then used in conjunction with the methanol–Pt cluster calculations to derive the parameters of the final O / Pt(100) part of the pseudopotential, which takes the following form:

O–Pt(100):

$V = o0 + o1q1 + o2q2$

$o0 = A1 \times \exp(-B7 \times r_z) + A2 \times \exp(-B8 \times r_z) + A3 \times \exp(-B9 \times r_z)$

$o1 = A4 \times \exp(-B10 \times r_z) + A5 \times \exp(-B11 \times r_z)$ $\quad q1 = \cos(2\pi r_x/l) \times \cos(2\pi r_y/l)$

$o2 = A6 \times \exp(-B12 \times r_z) + A7 \times \exp(-B13 \times r_z)$ $\quad q2 = \cos(4pr_x/l) + \cos(4\pi r_y/l)$

CH_3–Pt(100):

$V = c0 + c1q1 + c2q2$

$c0 = A8 \times \exp(-B8 \times r_z) + A9 \times \exp(-B9 \times r_z) + A10 \times \exp(-B10 \times r_z)$

$c1 = A11 \times \exp(-B11 \times r_z)$ $\quad q1 = \cos(2\pi r_x/l) \times \cos(2\pi r_y/l)$

$c2 = A12 \times \exp(-B12 \times r_z)$ $\quad q2 = \cos(4\pi r_x/l) + \cos(4\pi r_y/l)$

H–Pt(100):

$V = h0 + h1q1 + h2q2$

$h0 = A13 \times \exp(-B13 \times r_z)$

$h1 = A14 \times \exp(-B14 \times r_z)$ $\quad q1 = \cos(2\pi r_x/l) \times \cos(2\pi r_y/l)$

$h2 = A15 \times \exp(-B15 \times r_z)$ $\quad q2 = \cos(4\pi r_x/l) + \cos(4\pi r_y/l)$

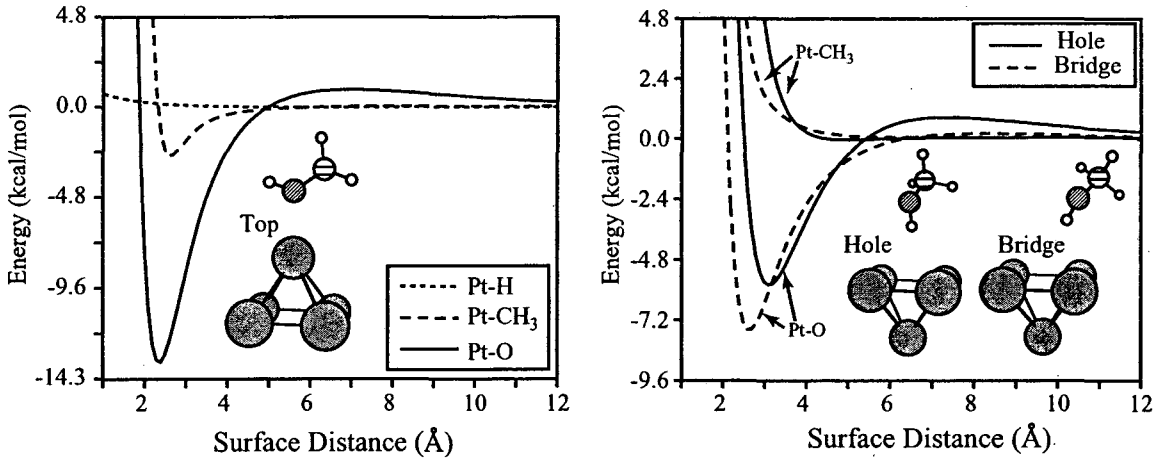

Figure 8.1 The potential energy surfaces and optimal structures of methanol at various positions on a platinum cluster.

with l=0.392 nm, the lattice constant of platinum. The parameters are given in Table 8.2.

It was found that the optimal position for the methanol was at the top position of the cluster, which has an interaction energy of −14.6 kcal/mol. The next favorable position was in the center of the four platinum atoms followed by the bridging position by −4.17 kcal/mol and −4.09 kcal/mol, respectively. The [CH_4 or CH_3] / Pt(100) potential is mostly repulsive except at the top position, which has a well depth of −2.57 kcal/mol. The potential energy surfaces for the methanol sites at the top position are shown on the left of figure 8.1 and the Pt–O and Pt–CH_3 potential surfaces are shown on the right. The optimal structures are also shown in the insets of Fig. 8.1.

The methanol–methanol interaction has been described by the H1 model of Haughney et. al., which has been found to adequately represent the bulk properties of the liquid.[180] The Lennard–Jones parameters and electrostatic charges are also given in Table 8.1.

O–Pt(100): kJ/mol		CH_3–Pt(100)[a]: kJ/mol		H–Pt(100): kJ/mol	
A1	60382.3559	A8	3178822.309	A13	8.028
A2	–477.6497	A9	2096.8431	A14	–0.168
A3	238.0177	A10	0.2847446	A15	0.0050
A4	9019.8	A11	12774.97		
A5	–5564.9	A12	–247.209		
A6	–210.8173				
A7	108.8193				
	nm^{-1}		nm^{-1}		nm^{-1}
B1	30.14	B8	48.6752	B13	9.9020
B2	7.6517	B9	15.7219	B14	21.9630
B3	8.0555	B10	0.1245	B15	30.0550
B4	14.8032	B11	22.9003		
B5	13.3941	B12	11.7690		
B6	5.8097				
B7	4.1003				

a. This potential is derived for a CH_4 – Pt(100) potential.

Table 8.2 The Pt(100) / methanol potential parameters.

Section 8.4 Results

The purpose of this study is to characterize the equilibrium and non–equilibrium solvent response of methanol to a solvated electron in low temperature and reduced dimensional media. Specifically, we wish to calculate the solvent response to an excess electron in a low temperature glassy bulk, in a gas cluster and on a 2–dimensional surface interface. Standard molecular dynamics methods used for the bulk and are summarized as follows. The trajectory of the methanol molecules was calculated using the leapfrog algorithm which incorporates the SHAKE method in order to constrain each molecule to be a rigid body.[181] The fact that the molecules are rigid allows for the use of a large timestep of 5 fs to be used for these simulations.

A. Room Temperature Methanol. In order to verify that our quantum/classical dynamics program is operating properly, we have run equilibrium simulations of the

solvated electron in room temperature methanol. The temperature of 200 methanol molecule was controlled using the Nóse–Hoover method with the temperature set to 300K for canonical ensemble simulations. The calculated binding energies are in agreement with those of Turi and Rossky and are summarized in Table 8.3. While Turi and Rossky were not certain as to the source of the discrepancy between their results and those of Zhu and Cukier, if one applies the long polarization range correction factor of –0.35 eV to the potential and binding energies to the results the agreement between all three groups is improved. It is likely, however, that Zhu and Cukier did not apply this correction factor as well. Thus slight differences in the models employed are responsible for these discrepancies.

Several properties of the room temperature solvated electron have been calculated to compare to the frozen glass results. Shown in Figure 8.2 on page 135 are the radial distribution functions of the H–e^-, O–e^- and CH_3–e^- site pairs. The results indicate that the electron is preferentially solvated with the electropositive H end of the solvent pointing towards the electron center of mass, as has been observed previously using this model.[169,173] Integration of the radial distribution indicates that there are 4–6 solvent molecules occupying the first solvent shell and there is no indication of long range order which is consistent with a bulk liquid solution. The equilibrium solvation response function for the electron is shown in Figure 8.3. The best fit indicate that there exists an initial 25.2 fs Gaussian responds, followed biexponential decays of 220 fs and 1.7 ps, respectively.

Overall, the results in the room temperature methanol show that our model and program are working in accord with the previously reported findings. These results are

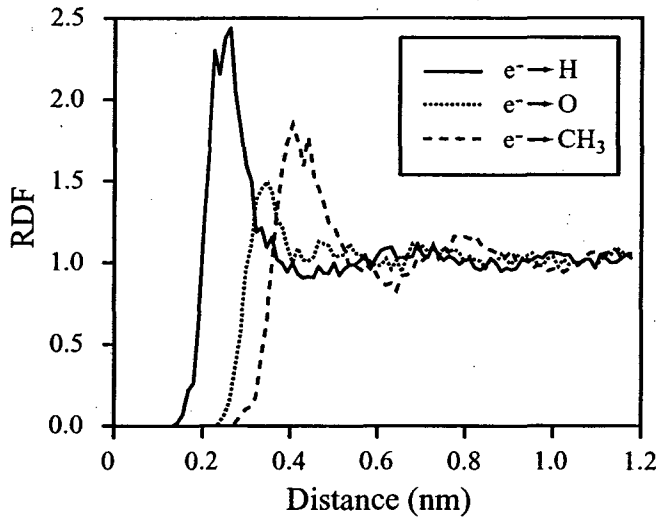

Figure 8.2 The radial distribution functions of room temperature liquid methanol with the solvated electron.

also used in comparison to the solvation dynamics observed with the excess electron in frozen glasses and at surface interfaces as discussed below.

B. Frozen, Glassy Methanol. The results of the room temperature simulations indicate that the program is performing acceptably. With this in mind, we have moved to simulating of the excess electron in low temperature glass. The simulation methods were the same as the room temperature results with the thermostat set to 100K with the density taken from ref. 182. These results are summarized in Table 8.3. After equilibrating a configuration of methanol at 100 K, an electron was introduced into the system and was allowed to equilibrate for ~50 ps. After equilibration, the dynamics were monitored for an additional 75 ps of simulation.

The results of the simulations of the excess electron in low temperature bulk methanol reveal several properties of solvation in a glassy medium. For one, the kinetic energy (which is a measure of the size of the solvent cavity of the quantum mechanical

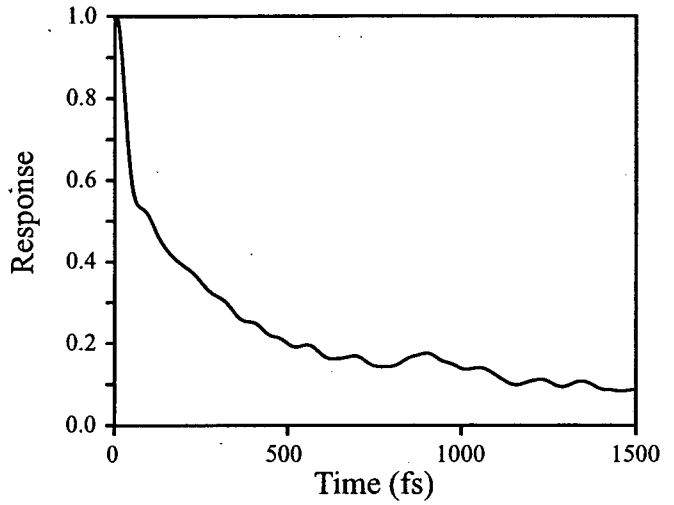

Figure 8.3 The solvation dynamics of an excess electron in room temperature methanol.

electron) increases to 1.99 eV compared to the 1.79 eV value observed in the room temperature liquid results. This fact is reflected in the change in the radius of gyration of the spherically symmetric ground state, which contracts from 2.6 Å to 2.3 Å with the decrease in temperature. The compression of the electron and the larger kinetic energy are likely the result of the increased ordering of the solvent structure about the excess electron at low temperatures, as shown in the radial distribution functions in Fig. 8.4. This enhanced local structure of methanol about the electron is indicative of more favorable solvent interactions with the particle, which is reflected by the lowering of the binding energy by −0.38 eV in the low temperature glass compared to the ambient liquid. Integration of the radial distribution functions indicates that 4 methanol molecules comprise the first solvent shell. Overall, the electron is much more strongly bound in the frozen glass compared to the electron at room temperature solution.

The solvation dynamics of the localized electron in glassy methanol has been investigated. Shown in Fig. 8.5 are the equilibrium and non–equilibrium solvation

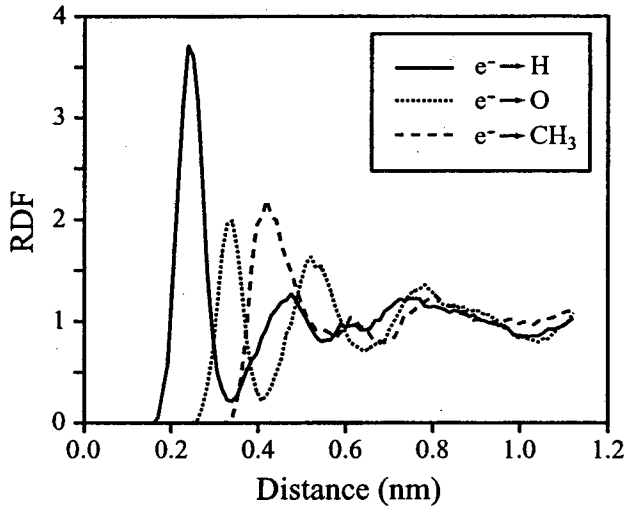

Figure 8.4 The radial distribution functions of frozen glassy methanol with the solvated electron.

dynamics of the excess electron in frozen methanol glass. The best fit to the equilibrium solvation dynamics is composed of a 22 fs Gaussian response and a 87 fs followed by a ~1.6 ps biexponential decay. The ps bath response in low temperature methanol glass is similar to the long time exponential decay in the room temperature liquid, which is surprising given that long timescale exponential solvation dynamics has often been attributed to diffusive bath motion.

The non–equilibrium dynamics of electron injection into the low temperature methanol glass has also been simulated. As has been observed in previous room temperature charge injection studies,[174] the electron probability distribution is initially diffuse and quickly collapse. There is a corresponding fast increase in the kinetic energy which then relaxes by ~0.4 eV. As shown in the inset of Figure 8.6, the electron initially has 4 methanol molecules occupying the first solvent shell which decreases to 1 solvent molecule within ~200 fs. This process is likely facilitated by the large temperature

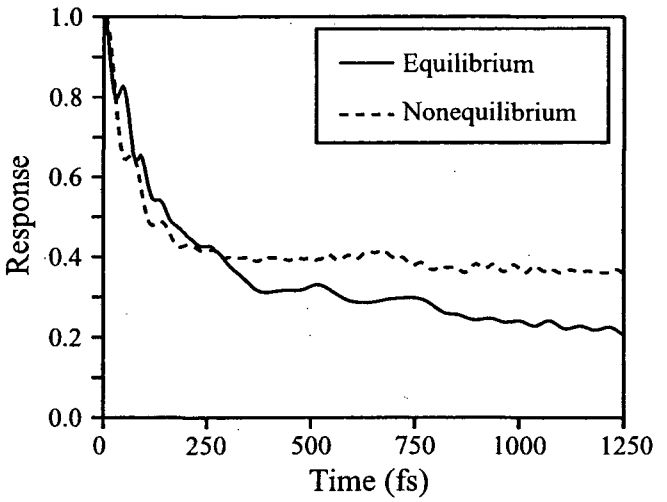

Figure 8.5. The equilibrium and non–equilibrium solvation dynamics of an excess electron in low temperature glassy methanol.

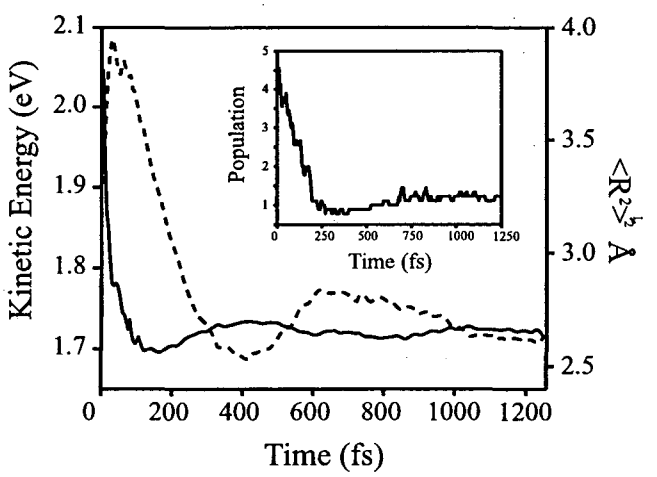

Figure 8.6. Various properties of the electron and bath in the low temperature charge injection simulations.

increase in the first shell to ~350 K. The population within this shell appears to slowly recover on a timescale much longer than the non–equilibrium trajectory of 1.5 ps.

C. Solvation Dynamics at the MeOH–Pt(100) Interface. The dynamics of an excess electron in a 2D periodic methanol bath have been simulated within the NVT ensemble for the equilibrium simulations. Periodic boundary conditions were enforced in the x and y directions. In order to describe the long range Coulombic interactions, the Ewald method has been utilized with a large z simulation edge length to minimize layer–to–layer interactions. This approach has been used successfully in several recent investigations of interfacial systems with slab periodicity.[183–186] As the split operator method is unstable when divergent potentials are close to the grid edge, a surface image potential was not used in these simulations. The x and y box length was set to 35.28 Å and the z length was set to 90 Å. Given the lattice constant of Pt(100), this geometry represents a methanol molecule to Pt atom coverage ration of ~2.5. Our preliminary work showed that the excess electron needed 125 ps of simulation time to equilibrate, after which time the dynamics of this system were characterized for an additional 200 ps. Unfortunately, our methods are not suitable to conduct non–equilibrium simulations under these conditions as discussed below.

As part of the characterization of the electron, we have developed a novel method for calculating radial distribution functions for systems with slab periodicity. The algorithm is based on an 'on–the–fly' normalization scheme and does not require any *a priori* approximation. A full description of our method is given in the Appendix.

Overall, the loss of periodicity in a single direction results in the electron becoming less bound at the surface interface by a factor of ~2 compared to in the low temperature bulk. There is a corresponding decrease in the kinetic energy and expansion of the radius of gyration of the excess electron. The extra spatial width of the electron also manifests itself in the 2D radial distribution function shown in Fig. 8.7, for which

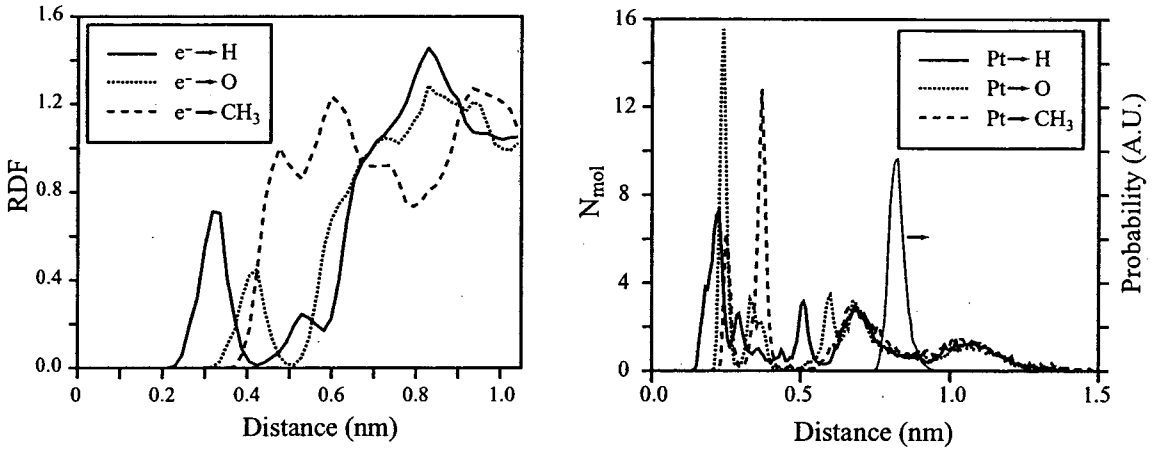

Figure 8.7. The radial distribution functions of methanol with the solvated electron at a Pt(100) interface. Also shown are the z–dependent distributions.

the closest approach for the hydrogen and oxygen sites are nearly 1 Å greater than observed in bulk and cluster simulations. These results also indicate that there is a significant change in the solvent structure for the interface, with the CH_3 site distribution almost overlapping and dominating over that of the oxygen site. This may be a result of the strong surface potential which solvent / excess electron interaction and introduces asymmetry in the z direction.

Shown in Figure 8.7 is the solvent response function. The equilibrium response has a long time component of >4 ps, which is the longest solvation timescale seen in all the media. Unfortunately, the non–equilibrium calculations could not be performed as the split operator method did not converge to a localized wavefunction in the initial step. Consequently, the FFT grid based method generally gives spurious results and the simulation results are not reliable representation of the dynamics of the system.

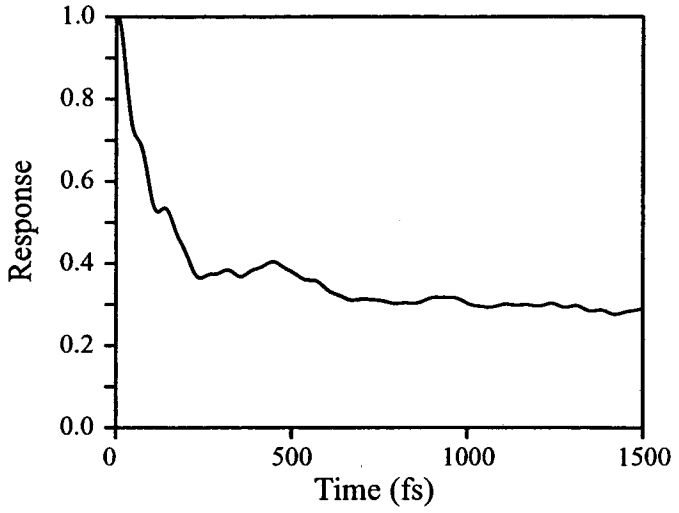

Figure 8.8. The equilibrium solvation dynamics of an excess interfacial electron in low temperature methanol bath at a Pt(100) interface.

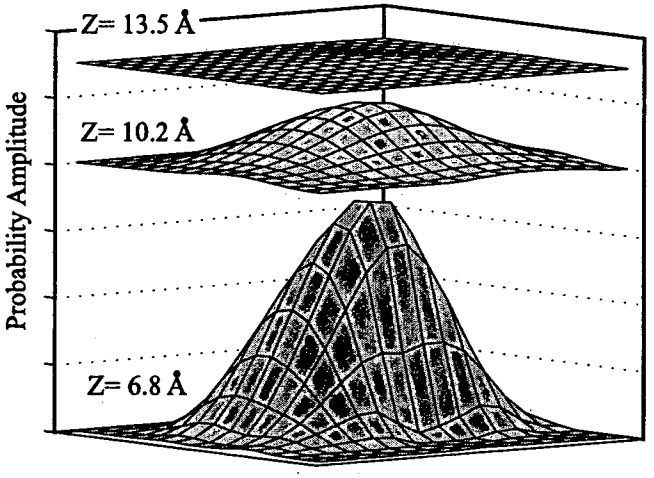

Figure 8.9. The probability distribution of an excess interfacial electron in a methanol bath.

D. Solvation Dynamics in the Gas Phase Cluster. The dynamics of an excess electron in a gas cluster of 200 methanol molecules has been simulated within the NVE

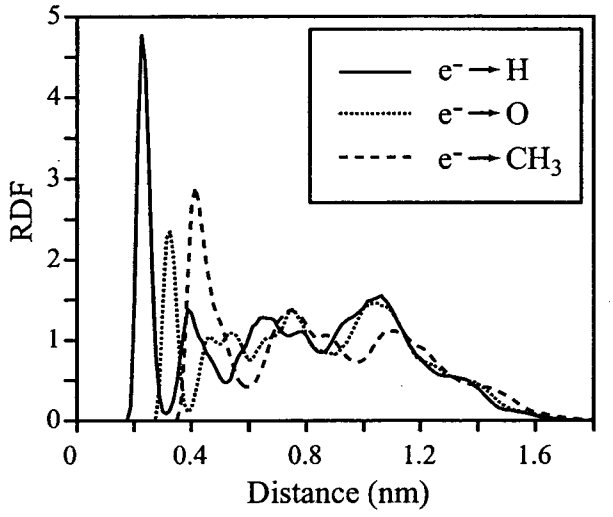

Figure 8.10 The radial distribution functions of frozen gas phase methanol cluster with the solvated electron.

ensemble for the equilibrium and non–equilibrium studies. The non–equilibrium calculations were performed in the same manner as described for the bulk. The excess electron was allowed to equilibrate for 50 ps and while properties and response functions were calculated over an additional 75 ps. The electron was initially placed in the center of the cluster and did not significantly deviate from this location during the course of these simulations. Because of the unusual solvation dynamics that were observed, we re–equilibrated the gas cluster to 100 K and performed a second 75 ps simulation. These calculations were also repeated in the NVT ensemble. Unfortunately, the use of the NVE ensemble in the equilibrium calculations results in a slow yet steady drift in the temperature. Thus, the average temperature of 106 K in these simulations is slightly higher than in other calculations.

The results of the simulations of the excess electron in a low temperature methanol gas cluster provide an excellent contrast to the dynamics observed in

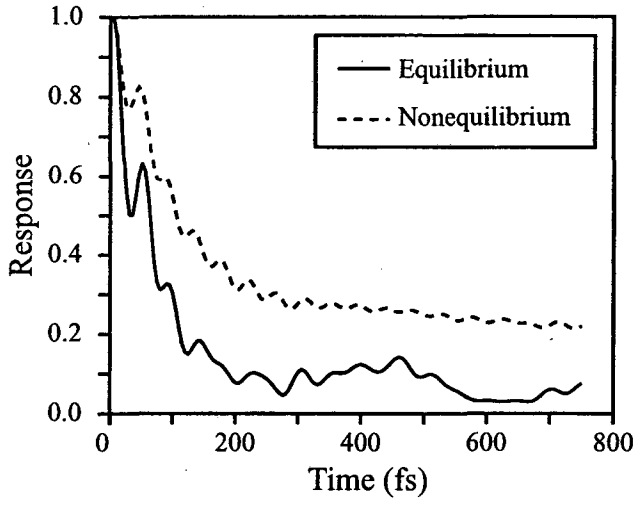

Figure 8.11. The equilibrium and non–equilibrium solvation dynamics of an excess electron in low temperature methanol gas cluster.

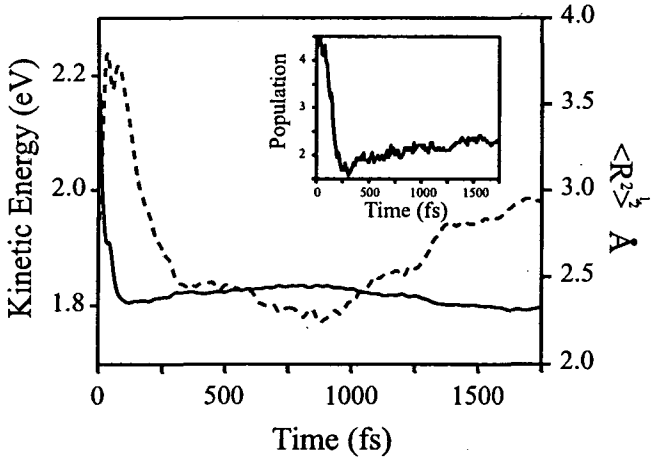

Figure 8.12. Various properties of the electron and methanol gas cluster in the low temperature charge injection simulations.

conditions of bath 3D and 2D periodicity. Energetically, there is very little difference between the solvated electron in the gas phase cluster and in the bulk. The electron has a

Bath Temperature	Binding Energy (eV)	Potential Energy (eV)	Kinetic Energy (eV)	Size[b] (Å)
Bulk, 300 K	−1.95[a]	−3.74[a]	1.79	2.61
Bulk, 100 K	−2.33[a]	−4.32[a]	1.99	2.32
Surface, 100 K	−0.99	−1.87	0.88	3.69
Cluster, ~107 K	−2.30	−4.40	2.09	2.22

a. The long range correction factor to the polarization has been applied to these results.

b. Calculated as $\langle\Psi|(r-r_0)^2|\Psi\rangle^{1/2}$, where r_0 is defined as $\langle\Psi|r|\Psi\rangle$.

Table 8.3. The average properties of the solvated electron in the various simulations reported.

slightly higher kinetic energy and a corresponding smaller radius of gyration in the cold cluster. Inspection of the radial distribution functions, shown in Fig. 8.10, show that this is likely a result of the greater ordering of the methanol bath around the excess electron in the cluster. The solvent appears to be more packed in the first shell and is composed of one less solvent molecule as compared to the frozen bulk environment. Despite the overall similarities in the static properties of the two systems, as shown in Figure 8.11 the equilibrium and non–equilibrium solvent response functions are very different. The equilibrium response is dominated by a 96 fs exponential decay. The non–equilibrium response is similar, except for the appearance of a much longer, several ps component to the relaxation process. As was observed in the bulk simulations, the non–equilibrium dynamics are characterized by a fast radial collapse of the wavefunction, with a corresponding increase and recovery of the kinetic energy. These dynamics are illustrated in Figure 8.12. The number density in the first solvent shell was found to

sharply decrease within the first 200 fs, which then slowly recovers on a timescale of several ps.

Section 8.4 Discussion

A. Bulk Results. Structure and Dynamics. The structure of the solvated electron in the frozen bulk shows that the electron is stabilized under glassy conditions relative to the room temperature liquid. The nearest location of the H site of the solvent compresses to within 2.4 Å and slightly overlaps the wavefunction of the electron, which has a radius of gyration of 2.3 Å in low temperature methanol glass. Integration of the radial distribution functions reveals that 4 methanol molecules comprise the first solvent shell. These results are in excellent agreement with the earlier ESR studies by Kevan.[187,188] Those investigations found that excess electrons prepared by ionizing radiation in 1.5 K methanol glass were solvated by 4 molecules with an average electron / proton distance of 2.3 Å.

The equilibrium solvation dynamics of the excess electron in glassy low temperature methanol are interesting when compared to the room temperature liquid results. The solvation dynamics under ambient and low temperature conditions may be broken into three components, an initial Gaussian followed by two exponential decays as has been previously reported.[174] The fast Gaussian component is more important in the room temperature liquid, while the long timescale exponential is the dominant contribution to the dynamics in the low temperature glass. While the weights of the various contributions to the solvation dynamics depend on the temperature of the bath, it is curious that the solvation timescales are largely identical. Thus, if the Gaussian and fast exponential timescale components are due to reorientation of the solvent OH bonds,

then the overall hydrogen bond network must not be significantly perturbed as the resulting dynamic would be much slower in the low temperature glass. Likewise, the fact that the long timescale dynamics are similar at room temperature and at 100K is not consistent with solvent or solute diffusional motion. These observations are identical to the conclusions based on previous studies of electron solvation dynamics in low temperature glassy media. Low temperature experiments in alcohols have shown that hydrogen bond breakage is not the limiting factor in the dynamics of electron solvation.[189] These experiments also determined that viscosity does not dominate the solvation process as excess electrons are fully solvated at room temperature and at 77K.[187,188] These previous reports concluded that molecular reorientation is the dominate solvation process and occurs in both room temperature and low temperature (>77 K) alcohol baths,[189–192] although more recent investigations in room temperature alcohol solution have concluded that hydrogen bond breaking does occur.[193–197] If large scale hydrogen bond rearrangement is important in electron solvation, then it may be true that we can not simulate this system for long enough at low temperatures to observe those dynamics in both the equilibrium and non–equilibrium simulations.

The non–equilibrium response of the system to charge injection has been investigated. Shown in Figure 8.5 are the equilibrium and non–equilibrium response functions to electron solvation, averaged over 20 such simulations. For the most part, the solvent responses appear similar except for the fact that the final decay to equilibrium appears to take longer in the charge injection simulations. Shown in Figure 8.6 are various time dependent properties of the non–equilibrium dynamics. Following charge injection, the kinetic energy initially increases and then rapidly decays, which is mirrored

by a fast radial collapse of the electron wavefunction. This process is accompanied by a loss of population within the first solvent shell from the initial equilibrium value of 4 methanol molecules to ~1 within 200 fs. The loss of first solvent shell molecules is likely facilitated by the large increase in the local temperature from 100K to ~350 K. The first solvent shell population does not appear to recover on the 1.25 ps timescale that these simulations were conducted and likely accounts for the long return to equilibrium. This fact is reflected in the kinetic energy and radius of gyration of the electron, neither of which appear to approach their equilibrium values. These observations suggest that the long timescale component to the non–equilibrium dynamics is due to either solvent reorientation or diffusion into the first solvent shell followed by a radial collapse and increase in kinetic energy of the excess electron wavefunction. It is interesting to note that our findings in low temperature glass are similar to those reported by Turi et. al. in their non–equilibrium room temperature liquid methanol simulations.[174] It would lead us to conclude that both equilibrium and non–equilibrium solvation dynamics are similar at room temperature and in frozen methanol.

The dynamics observed in these low temperature charge injection studies are in agreement with experimental findings. Previous results have shown that the spectrum of the solvated electron in low temperature alcohol glasses has red–shifted absorptions that decay following charge injection.[189,190,198] The present findings elucidate the microscopic dynamics responsible for these observations. The loss of solvent molecules within the first solvent shell destabilizes the ground state of the excess electron, while previous theoretical studies have shown that larger cavities are preferable to the excited states.[182,195] These findings indicate that the red shifted spectrum of the solvated electron following charge injection is a result of the destabilization of the ground state

energy level with respect to the first excited states. In the language of refs. 196 and 197, in this state this species may correspond to the weakly bound ground state electron, the spectra of which has been proposed to blue shift before the species transforms to a strongly bound state. This spectral shifting may be a result of the slight repopulation within the first solvent shell as shown in Fig 8.6. Unfortunately, due to computational considerations we did not simulate the non–equilibrium dynamics for long enough to observe any possible sudden transformations to a strongly bound ground state.[196,197] Despite this, our equilibrium simulations do show two distinct solvated states, the binding energy of which correlates with the radius of gyration. The observation of two distinct ground states at equilibrium does lend credence to the hybrid model of refs. 196 and 197.

B. Surface Interface Results. Structure and Dynamics. Recent reports have shown that excess electrons may be solvated within a layer of polar molecules deposited on the surfaces of metals.[166–168] In order to theoretically describe the microscopic properties and dynamics of the excess electron in these systems, we have simulated a quantum mechanical electron trapped in a finite interfacial layer of methanol on a Pt(100) surface.

The surface simulations reveal many properties of the dynamics of the interfacial electron. The binding, potential and kinetic energy are reduced by over a factor of half in these simulations. The loss of kinetic energy is accompanied by an expansion in the radius of gyration of the wavefunction. The change in the solvent structure may in part explain these observations. Shown in Figure 8.7 are the radial distribution functions of the solvent with the excess electron calculated using the method described in the Appendix. The electron is largely solvated by the H and O sites, the methyl group

almost overlaps the oxygen site and therefore must interact with the electron to a greater extent than in the cluster and bulk simulations. This is likely due to the asymmetry in the non–periodic direction introduced by the surface potential as shown in Figure 8.7. The electron primarily resides between the second and third methanol layer, as the first layer is very rigid due to the strong interactions with the surface. It is these strong metal / solvent potential at the surface edge that likely prevents charge migration into the 1st layer and alters the OH bond / electron interactions in the 2nd and 3rd layer. While both ambient and low temperature methanol have similar three component equilibrium solvent response functions, the dynamics observed at the low temperature surface interface are only biphasic. Consequently, the 2–dimensional bath has less dynamical modes by which it can respond to fluctuations in the solute as are present in the 3–dimensional bulk.

These calculations are in agreement with our previous observations using two photon photoemission.[166,167] Shown in Figure 8.9 is the probability amplitude of the ground state electron wavefunction from a single methanol / Pt(100) configuration. The largest amplitude is at the center of the electron's configurational grid (z=6.8 Å) and is largely spherical in shape and localized in character. Thus, the methanol bath has formed a stable trap for the electron to become fully solvated. This is in agreement with the earlier observations that electrons may become localized and solvated at surface interfaces; if formation of a localized state were not possible then methods would have produced a divergent trajectory. Our attempts at non–equilibrium simulations were divergent due to the initial convergence of a delocalized electronic wavefunction. Once again, this agrees with experimental results which found that an excess electron is initially delocalized parallel to an alcohol / Ag(111) surface following charge injection.

Section 8.5. Conclusion

The structure and dynamics of the solvated electron in low temperature glassy methanol has been shown to agree with the experimental results. The timescales for the solvation dynamics are similar in room temperature and glassy bulk methanol, leading us to conclude that neither hydrogen bond breaking nor diffusional dynamics are responsible for solvation of the excess electron. However, the lack of any observable large scale hydrogen bond or diffusional dynamics may be due to the fact that we cannot perform simulations for long enough to describe such slow processes at low temperatures. The charge injection studies have shown that the loss of solvent population within the first shell is the likely source of the previously observed red–shifted absorptions in low temperature alcohol solvents.

The excess electron at a low temperature surface has shown that the excess electron is solvated, however destabilized, at the Pt(100) / methanol. The loss of binding energy is the result of the interfacial "freezing" the first bath layer and the lack of long range polarization interactions. The structure of the excess electron is also altered at the interface, becoming more diffuse which is accompanied by an increase in the size of the solvent cage. The solvation dynamics have been shown to be biphasic, which is in contrast to the dynamics observed in both ambient and room temperature bulk.

Chapter 9

Transition Path Sampling of Ligand Exchange

Section 9.1 Introduction

Intermolecular ligand exchange is ubiquitous in the reaction dynamics of organometallic compounds. While the mechanism of ligand exchange of coordinatively saturated species is generally described as associative, dissociative or interchange in nature, the process by which unsaturated species form products has been the subject of debate in the literature.[199–204] Photogenerated unsaturated organometallic intermediates have been proposed to undergo both intermolecular and intramolecular mechanisms.

With the advent of ultrafast laser spectroscopy, it has been possible to directly observe the formation of products from unstable photogenerated reactants in solution. Several investigations have shown that weakly bound intermediates are formed following photolysis of organometallic species in reactive solvents. The rearrangement of the unreactive solvated transient to the product is often the rate limiting step in the reaction mechanism. While previous studies concluded that the formation of the product is an intramolecular process,[20–24] work done in our group and in others have shown that unsaturated organometallic intermediates exchange loosely bound "token ligands" via an intermolecular mechanism.[3,4,205,206] At present, there is no agreement whether this process is associative, dissociative or interchange in nature.[3,4,199–204] In order to resolve these issues, our group decided to model this process using Langevin and Molecular Dynamics (MD) methods. While the results of the Langevin simulations mirror the observed dynamics,[206] the model was stochastic and diffusive in nature. In

	q_i/e	σ_{ij}/ Å	ε_{ij}/k_b
H	0.435	0.00	0.0
O	−0.700	3.03	105.2
CH_3	0.265	3.74	86.5
Cr	−0.928	N/A	0.0
C_{ax}	0.625	3.83	13.2
C_{eq}	0.655	3.83	13.2
O_{ax}	−0.496	3.12	80.1
O_{eq}	−0.456	3.12	80.1

Table 9.1 The Lennard–Jones and electrostatic simulation parameters used for the methanol solvent and $Cr(CO)_5$ solute.

order to simulate ligand exchange without *a priori* assumption and to learn the microscopic details of the transition states, we have used the Transition Path Sampling (TPS) method of Chandler and co–workers.[207–212]

The purpose of these simulations is to augment the experimental conclusions concerning the mechanism of ligand exchange reactions. The model that we have

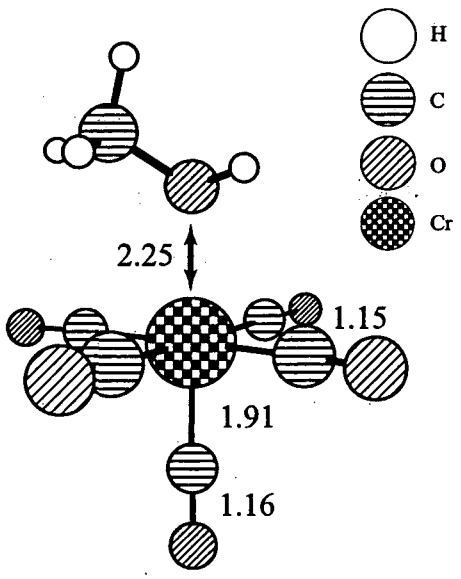

Figure 9.1 The optimized structure of $CrCO_5$ and methanol. Distances are in Å.

Pair	D_o (kJ/mol)	α_{ij} (nm^{-1})	R_{eq} (nm)
O / Cr	66.808	18.644	2.249
CH_3 / Cr	6.906	11.4211	2.879

Table 9.2 The Morse parameters for the $Cr(CO)_5$ / methanol potential.

chosen is that of the molecular complex $Cr(CO)_5(MeOH)$ in a methanol solvent. The simulation parameters for methanol are listed in Table 9.1 while a potential was derived to describe the solvent / $CrCO_5$ solute interaction. The electrostatic charges of $CrCO_5$ were derived from an NBO analysis of a LACVP**/B3LYP optimized geometry calculated with a methanol continuum solvent. Next, 15 optimized structures of a single methanol molecule with $CrCO_5$ were calculated at the LACVP**/B3LYP level of theory with the oxygen or CH_3 group constrained to various distances from the Cr site. The parameters of additional pair potential Morse functions were optimized to fit the calculated interaction energies of these geometries. The fully optimized $CrCO_5$ / methanol structure is shown in Figure 9.1 and the Morse parameters are given in Table 9.2.

The equilibrium characteristics of this system were calculated using the model described above. Shown in Figure 9.2 are the radial distribution functions of Cr with the methanol H, O, and CH_3 sites. It can be seen that the $CrCO_5$ fragment is rigorously solvated by the OH bond, which integrates to exactly 1 methanol molecule within the first solvation shell. The average energy in these simulations was –7.07 kcal/mol which corresponds to a temperature of ~295 K. In the course of our 200 ps of simulation (which takes ~2 days of simulation time on a Pentium III 1.0 GHz processor) not a single

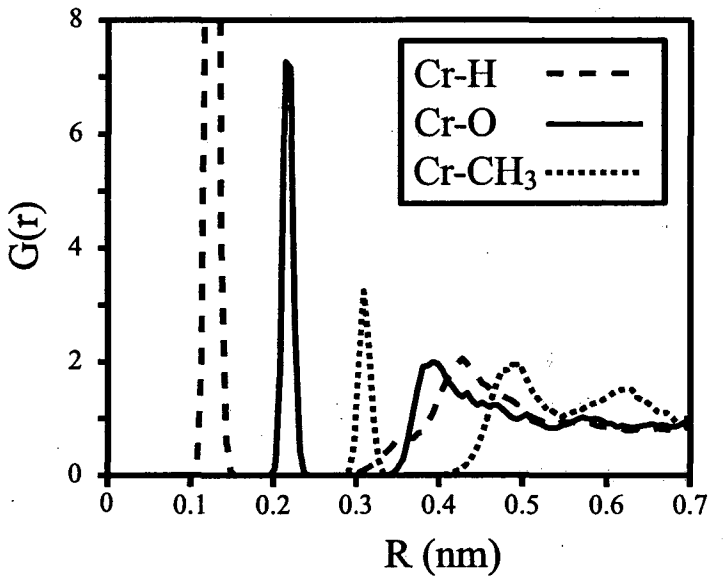

Figure 9.2 The radial distribution functions for H – Cr, O–Cr and CH_3 – Cr sites.

exchange from one solvating molecule to another was observed.

The optimized structure shown in Figure 9.1 has an interaction energy of −19.08 kcal/mol, which means that dissociation from the solvated state is likely a rare event. Consequently, a method is needed to sample the ligand exchange dynamics does not rely on brute force methods. For this reason we have turned to TPS simulations, which do not require *a priori* knowledge of the transition state(s) and is briefly described below.

Section 9.2. Transition Path Sampling

The purpose of Transition Path Sampling is to calculate the transition states and rate constants of rare events through computer simulation. The derivation of this method is rigorous and is given in detail in ref. 212, although a brief description is provided here. The heart of the TPS simulation is the 'shooting' move. A single configuration along a reactive trajectory is chosen at random and the velocities are slightly perturbed. A new trajectory is then propagated forward and backward in time and the new

simulation is accepted or rejected as described below. If accepted, then the configurations are saved as the present working trajectory and the process is repeated. The reactive dynamics can then be characterized from the accepted trajectory.

When performing these calculations in the NVE ensemble under steady state conditions, the acceptance criteria are very simple. The new trajectory needs to satisfy the following constraints: that it begins in a reactive basin and ends in the product state. The trajectory must also conserve the total energy under steady state conditions as there should exist equal probability to visit the altered configuration from the unperturbed state and vise versa. Unfortunately, performing TPS simulations on a constrained model presents a difficult situation. If the perturbed velocities have overlap with constrained vectors, such as fixed bond lengths, those velocity components are removed in algorithms like SHAKE or RATTLE. Consequently, the new configuration will be too "cold" and energy is not conserved. This problem is easily resolved, however, by modifying the RATTLE algorithm to remove velocity components along fixed bond vectors. Thus, once a perturbed state has been generated, the velocities are altered and the remaining components are then rescaled to conserve the total energy of the system.

There are two other important algorithms in the TPS method, which are called "shifting" or "reptation" moves. In a shift, several steps of the reactive trajectory are deleted and the simulation is allowed to propagate from the last configuration for an equal amount of time. This can also be done in reverse and the new trajectory is accepted or rejected as defined above. Although the shifting moves do not likely alter the properties of the transition state(s), they are very important in exploring the phase space within the transition path ensemble. While an equal number of shooting and shifting moves are allowed in the present study, only the reactive shooting trajectories

were used to examine the dynamics of the reaction.

The ligand exchange reaction of methanol bound to a $Cr(CO)_5$ fragment has been characterized using the techniques outlined above. In order to perform these simulations we need to pick a criteria, which is referred to as the order parameter λ, that adequately characterizes reactive and product basins and allows the exploration all of the reactive phase space. In the present case, the Cr–O site distance is used as an order parameter. As shown in the inset of Figure 9.2, the solvated Cr–O distance is no greater than 2.4 Å in the first solvent shell and is clearly divisible from the second shell and continuum which reside at Cr–O distances greater than 3.5 Å. The product basin is thus defined as a molecule which has a Cr–O distance of less than 2.4 Å and all other oxygen sites are ≥3.5 Å. A transition is defined to occur when the same criteria are met yet the identity of the solvating molecule has changed.

Section 9.3 Results and Discussion

The first reactive trajectory in this study was created using artificial forces. While this initial trajectory is not representative of the unconstrained dynamics, the artificial forces were removed and the system was annealed for several thousand successful reactive trajectories. The reaction dynamics were then characterized for an additional one thousand transitions. In these simulations of ligand exchange, various properties are averaged with regard to the last exchange of bound ligands, which in this case is defined as the point when the initially solvating molecule has a greater Cr–O distance than the exchanging methanol. This configuration is treated as the zero timestep in the reaction mechanism.

It was initially believed that a the ligand exchange reaction for the present model

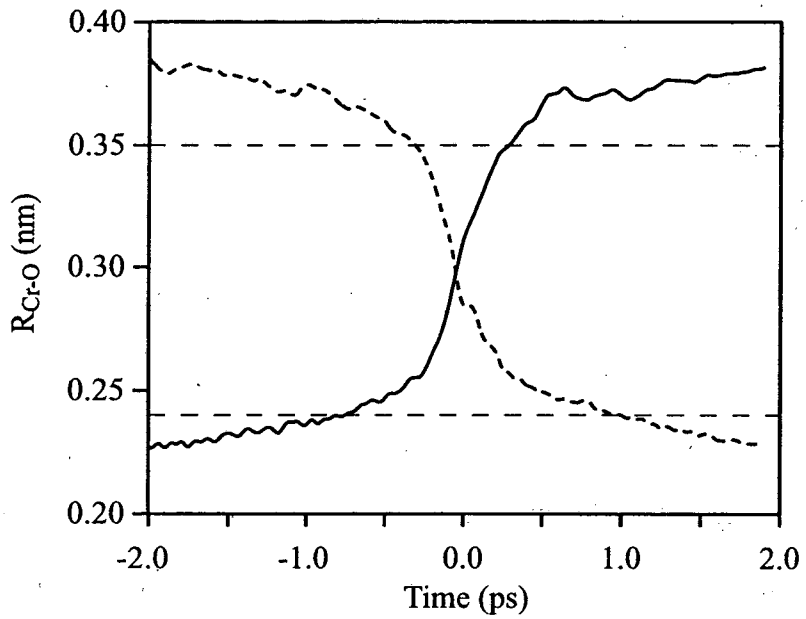

Figure 9.3 The Cr–O distances for the nearest (solid line) and next nearest (broken line) solvent molecules and unsaturated $Cr(CO)_5$. The equilibrium upper and lower limits for the first and second solvent shells, 0.24 nm and 0.35 nm, are also shown.

would be dissociative in nature. Shown in Figure 9.3 is the Cr–O distance for the nearest and next nearest solvent molecules. It can be seen that the initial step of the reaction is the partial dissociation of the initially bound solvent molecule out of the first solvation shell. This dynamic induces a 2nd shell methanol molecule to enter the same region between the first and second solvation spheres. The system propagates in this region for ~1 ps, after which time the formerly bound molecule moves into the solvent continuum, leaving the other to bind to the Cr site. Consequently, while it may appear that these dynamics are more accurately described using an interchange mechanism, the reaction dynamics of ligand exchange is more likely the result of a tandem process comprised of dissociative and associative steps as discussed below.

The present results clarify the dynamics of ligand exchange for coordinatively unsaturated organometallic species. First, the fact that an initially bound solvent must partially dissociate for the exchange to occur gives the reaction dissociative character. In the next step, a second molecule must move into the normally void volume between the first and second solvent shells, giving the mechanism associative character. The system appears to be in a metastable basin in this configuration due to the large amount of time that the exchanging ligands spend in this region. Equilibrium simulations of neat methanol suggest that the oxygen site of a single molecule may diffuse ~1 Å within 1 ps, which is similar to what is observed in the ligand exchange reaction. Further, while the total energy of the exchanging ligands and $Cr(CO)_5$ intermediate is above the equilibrium value, the bath / reactant interaction is favorable in this configuration. While these observations may be due to the existence of a long, flat potential energy surface that connects the stable states, these results suggest that the system is in a local minima in the configuration space of the model. It is interesting to note that the last step in the reaction is the exact microscopic reverse of the first as the initially bound molecule must move into the second shell before the exchanging ligand can bind to the metal center.

The presently proposed model may be applied to previous studies which do not agree on a general mechanism for ligand exchange of coordinatively unsaturated organometallic intermediates. Using traditional experimental techniques, the ligand exchange reaction for any particular system would be characterized as dissociative if the first step in the presently proposed mechanism is the dynamical bottle–neck. In this limiting case, reaction would appear to have a [metal fragment]–ligand bonding ΔH^* and a positive ΔS^*. Likewise, if molecular diffusion from the continuum into the metastable

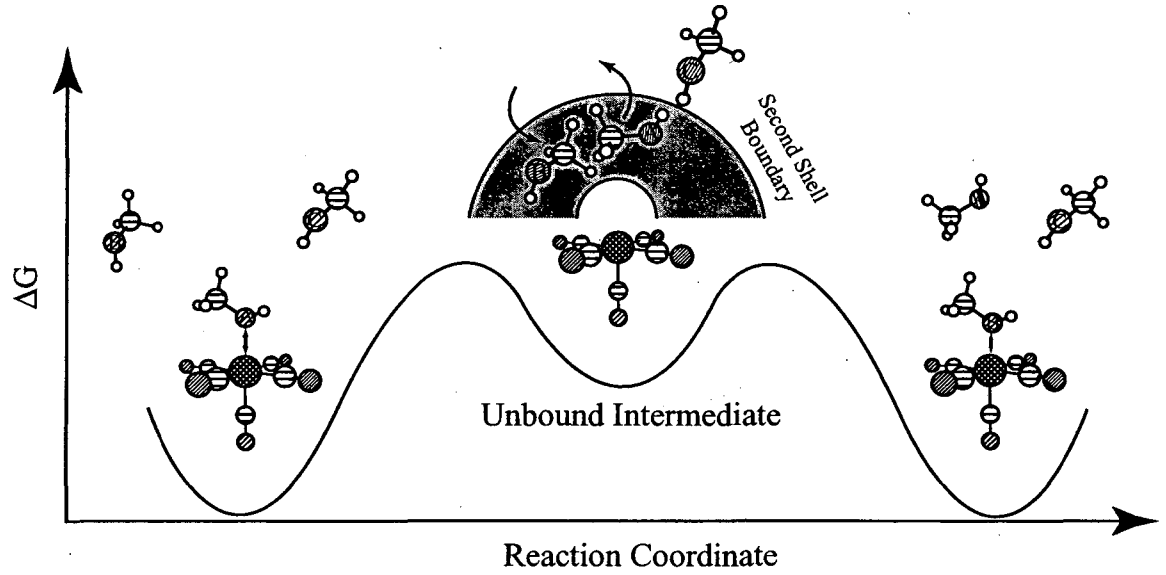

Scheme 9.1. The generalized mechanism of ligand rearrangement.

basin is the slow step, one would likely concur that the reaction is associative by nature. In this limiting case, the presence of a metastable basin may lower the activation energy of the first dissociative step and would reveal a slight ΔH^* and a small or negative ΔS^*. Systems in which both processes are important would appear to undergo interchange. Consequently, a general ligand exchange mechanism involving more than one step may unite the previous conflicting results.

Another interesting aspect of these studies is the dynamics of energy flow as shown in Figure 9.4. It can be seen that the total energy of the three reacting molecules increases until the reaction has completed. Also shown is the internal energy of the exchanging subsystem, which can be seen to overlap and overtake the total energy near the center of the trajectory. The only explanation for this observation is that the methanol bath has an overall stabalizing interaction with the exchanging ligands and $Cr(CO)_5$ beyond that of the equilibrium value. As shown in Figure 9.4, this is in fact the

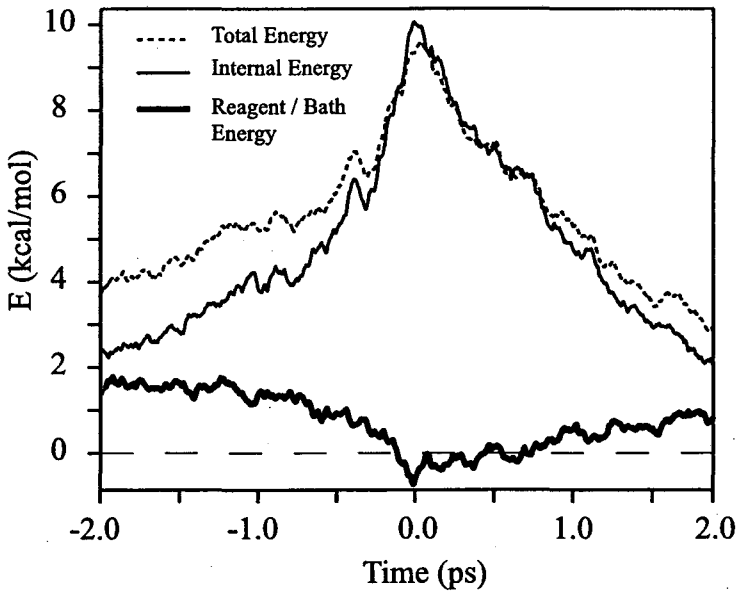

Figure 9.4. The flow of energy during the ligand exchange reaction. All results are the sum of the potential and kinetic energy with respect to their equilibrium values.

case as the reagent / bath interaction energy dips below the equilibrium value by ~1 kcal/mol. Consequently, the solvent is able to assist in the reaction through its favorable interactions with the reacting species, as this gives these molecules the extra energetic boost they need to cross over to form products. This observation is also suprising as the solvent is sometimes seen as having unfavorable interactions with reacting molecules due to their non–equilibrium character and the speed at which most chemical reactions occur. In this case, the bath is able to favorable solvate the intermediate state which is likely the result of the long reaction timescale and the fact that the molecular nature of the reactants is not perturbed.

The fact that the bath favorably solvates the reacting species prompted us to study other types of chemical reactions using Transition Path Sampling. The purpose of these simulations is to test whether this observation is a general phenomenon which has been

underestimated in other studies. Before the TPS method existed, molecular dynamics simulations of rare events were performed by forcing the reacting molecules to move along a predefined coordinate that may not be representative of the unconstrained dynamics. The molecular properties and energy flow may have been affected as a result. While these simulations have not been completed at the time of this writing, our initial data on the S_N2 reaction of Cl^- with CH_3Cl indicates that the fast displacement and charge switching results in largly unfavorable bath / reagent energies. Consequently, it is likely that our observations are representative of systems in which the molecular nature of the reactants is not highly perturbed during the course of a slow transition.

Section 9.3 Conclusion

The present proposed mechanism accounts for the reaction dynamics of ligand exchange in coordinatively unsaturated organometallic intermediates. While it may be true that every system of metal fragments and solvent molecules undergoes ligand exchange from processes that are unique to those interacting species, a tandem dissociative / associative process unites the previous conclusions under a single paradigm. Consequently, traditional mechanistic and ultrafast studies cannot capture the microscopic details of the reaction dynamics. The stabilization of the reacting species by the bath also assists the ligand exchange dynamics, however it is not known if this is a general observation. Further TPS simulations of ligand exchange will test the generality of the present conclusions.

References

[1] Bromberg, S. E.; Yang, H.; Asplund, M. C.; Lian, T.; McNamara, B. K.; Kotz, K. T.; Yeston, J. S.; Wilkens, M. J.; Frei, H.; Bergman, R. G.; Harris, C. B. *Science* **1997**, *278*, 260.

[2] Yang, H.; Asplund, M. C.; Kotz, K. T.; Wilkens, M. J.; Frei, H.; Harris, C. B. *J. Am. Chem. Soc.* **1998**, *120*, 10154.

[3] Yang, H.; Snee, P. T.; Kotz, K. T.; Payne, C. K.; Frei, H.; Harris, C. B. J. *Am. Chem. Soc.* **1999**, *121*, 9227.

[4] Zhang, S.; Zang, V.; Bajaj, H. C.; Dobson, G. R.; van Eldik, R. J *Organomet. Chem.* **1990**, *397*, 279.

[5] Yang, H.; Snee, P. T.; Kotz, K. T.; Payne, C. K.; Harris, C. B. J. *Am. Chem. Soc.* **2001**, *123*, 4204 .

[6] Bethune, D. S. *Appl. Opt.* **1981**, *20*, 1987.

[7] Jaguar 3.5; Schrodinger, Inc.: Portland, OR, 1998.

[8] Frisch, M. J.; Trucks, G. W.; Schlegel, H. B.; Scuseria, G. E.; Robb, M. A.; Cheeseman, J. R.; Zakrzewski, V. G.; Montgomery, J. A., Jr.; Stratmann, R. E.; Burant, J. C.; Dapprich, S.; Millam, J. M.; Daniels, A. D.; Kudin, K. N.; Strain, M. C.; Farkas, O.; Tomasi, J.; Barone, V.; Cossi, M.; Cammi, R.; Mennucci, B.; Pomelli, C.; Adamo, C.; Clifford, S.; Ochterski, J.; Petersson, G. A.; Ayala, P. Y.; Cui, Q.; Morokuma, K.; Malick, D. K.; Rabuck, A. D.; Raghavachari, K.; Foresman, J. B.; Cioslowski, J.; Ortiz, J. V.; Stefanov, B. B.; Liu, G.; Liashenko, A.; Piskorz, P.; Komaromi, I.; Gomperts, R.; Martin, R. L.; Fox, D. J.; Keith, T.; Al–Laham, M. A.; Peng, C. Y.; Nanayakkara, A.; Gonzalez, C.; Challacombe,

M.; Gill, P. M. W.; Johnson, B. G.; Chen, W.; Wong, M. W.; Andres, J. L.; Head–Gordon, M.; Replogle, E. S.; Pople, J. A. In; resision A.9 ed.: Pittsburg, PA, 1998.

[9] Schmidt, M. W.; Baldridge, K. K.; Boatz, J. A.; Elbert, S. T.; Gordon, M. S.; Jensen, J. H.; Koseki, S.; Matsunaga, N.; Nguyes, K. A.; Su, S.; Windus, T. L.; Dupuis, M.; Montgomery, J. A. *J. Comput. Chem.* **1993**, *14*, 1347.

[10] Becke, A. D. *J. Chem. Phys* **1993**, *98*, 5648.

[11] Lee, C.; Yang, W.; Parr, R. G. *Phys. Rev.* **1988**, *B41*, 785.[10]

[12] Allen, M. P.; Tildesley, M. P. *Computer Simulations of Liquids;* Clarendon Press, Oxford Science Publications, 1987.

[13] Collman, J. P.; Hegedus. L. S.; Norton, J. R.; Finke, R. G. P*rincipals and Applications of Organtransition Metal Chemistry;* University Science Books: Mill Valley, California, 1987.

[14] Dougherty, T. P.; Heilweil, E. J. *Chem. Phys. Lett.* **1994**, *227*, 19.

[15] Dougherty, T. P.; Grubbs, W. T.; Heilweil, E. J. *J. Phys. Chem.* **1994**, *98*, 9396.

[16] Dougherty, T. P.; Heilweil, E. J. *J. Phys. Chem.* **1996**, *100*, 201.

[17] Svec, H. J.; Junk, G. A. *J. Am. Chem. Soc.* **1967**, *89*, 2836.

[18] Virrels, I. G.; George, M. W.; Johnson, F. P. A.; Turner, J. J.; Westwell, J. R. *Organomet.* **1995**, *14*, 5203.

[19] Yang, H.; Kotz, K. T.; Asplund, M. C.; Harris, C. B. *J. Am. Chem. Soc*, **1997,** *119*, 9564.

[20] Simon, J. D.; Xie, X. *J. Phys. Chem.* **1986**, 90, 6751.

[21] Simon, J. D.; Xie, X. *J. Phys. Chem.* **1987**, 91, 5538.

[22] Xie, X.; Simon, J. D. *J. Phys. Chem.* **1989**, 93, 291.

[23] Xie, X.; Simon, J. D. *J. Am. Chem. Soc.* **1990**, *112*, 1130.

[24] O'Driscoll, E.; Simon, J. D. *J. Am. Chem. Soc.* **1990**, *112*, 6580.

[25] Kotz, K. T.; Yang, H.; Snee, P. T.; Payne, C. K.; Harris, C. B. *J. Organometallic. Chem.* **2000**, *596*, 183–192.

[26] Lian, T.; Bromberg, S. E.; Yang, H.; Proulx, G.; Bergman, R. G.; Harris, C. B. *J. Am. Chem. Soc,* **1996**, *118*, 3769.

[27] Jetz, W.; Graham, W. A. G. *Inorg. Chem.* **1971**, *10*, 4–9.

[28] Arndtsen, B. A.; Bergman, R. G.; Mobley, T. A.; Peterson, T. H. *Acc. Chem. Res.* **1995**, *28*, 154.

[29] Bergman, R. G. *Science* **1984**, *223*, 902.

[30] Snee, P. T.; Yang, H.; Kotz, K. T.; Payne, C. K.; Harris, C. B. *J. Phys. Chem. A* **1999**, *103*, 10426–10432.

[31] Hitam, R. B.; Rest, A. J. *Organometallics* **1989**, *8*, 1598.

[32] Rest, A. J. *Organometallics* **1992**, *11*, 3646.

[33] George, M. W.; Haward, M. T.; Hamley, P. A.; Hughes, C.; Johnson, F. P. A.; Popov, V. K.; Poliakoff, M. *J. Am. Chem. Soc.* **1993**, *115*, 2286.

[34] Bengali, A. A.; Bergman, R. G.; Moore, C. B. *J. Am. Chem. Soc.* **1995**, *117*, 3879.

[35] Abugideiri, F.; Keogh, D. W.; Poli, R. *J. Chem. Soc., Chem. Commun.* **1994**, 2317.

[36] Detrich, J. L.; Reinaud, O. M.; Reingold, A. L.; Theopold, K. H. *J. Am. Chem. Soc.* **1995**, *117*, 11745.

[37] Poliakoff, M.; Weitz, E. *Acc. Chem. Res.* **1987**, *20*, 408.

[38] Rawlins, K. A.; Lees, A. J. *Inorg. Chem.* **1989**, *28*, 2154.

[39] Servaas, P. C.; van Dijk, H. K.; Snoeck, T. L.; Stuhkens, D. J.; Oskam, A. *Inorg. Chem.* **1985**, *24*, 4494.

[40] Hehre, W. J.; Ditchfield, R.; Pople, J. A. *J. Chem. Phys.* **1972**, *56*, 2257.

[41] Francl, M. M.; Petro, W. J.; Hehre, W. J.; Binkley, J. S.; Gordon, M. S.; Defrees, D. J.; Pople, J. A. *J. Chem. Phys.* **1982**, *77*, 3654.

[42] Hay, P. J.; Wadt, W. R. *J. Chem. Phys.* **1985**, *82*, 299.

[43] Siegbahn, P. E. M. *J. Am. Chem. Soc.* **1996**, *118*, 1487–1498.

[44] Nakano, H. *J. Chem. Phys* **1993**, *99*, 7983–7992.

[45] Dunning, T. H.; Hay, P. J. *Methods of Electronic Structure Theory*; Plenum: New York, 1977; Vol. 2.

[46] Hay, P. J.; Wadt, W. R. *J. Chem. Phys.* **1985**, *82*, 270.

[47] Hay, P. J.; Wadt, W. R. *J. Chem. Phys.* **1985**, *82*, 284.

[48] Almond, M. J.; Page, E. M.; Rice, D. A.; Hagen, K. *J. Organo. Chem.* **1996**, *511*, 303.

[49] Snee, P. T.; Payne, C. K.; Kotz, K. T.; H., Y.; Harris, C. B. *J. Am. Chem. Soc.* **2001**, *123*, 2255.

[50] Rest, A. J.; Whitwell, I.; Graham, W. A. G.; Hoyano, J. K.; McMaster, A. D. *J. Chem. Soc., Dalton Trans.* **1987**, 1181–1190.

[51] Wasserman, E. P.; Moore, C. B.; Bergman, R. G. *Science* **1992**, *255*, 315–317.

[52] Siegbahn, P. E. M. *J. Am. Chem. Soc.* **1996**, *118*, 1487–1498.

[53] Belt, S. T.; Grevels, F.–W.; Klotzbucher, W. E.; McCamley, A.; Perutz, R. N. *J. Am. Chem. Soc.* **1989**, *111*, 8373–8382.

[54] Poliakoff, M.; Turner, J. J. *J. Chem. Soc. Dalton Trans.* **1974**, 2276–2285.

[55] Poliakoff, M.; Weitz, E. *Acc. Chem. Res.* **1987**, *20*, 408.

[56] Poliakoff, M. *Spectrochim. Acta* **1987**, *43A*, 217.

[57] Ryther, R. J.; Weitz, E. *J. Phys. Chem.* **1991**, *95*, 9841–9852.

[58] LeadBeater, N. *Coord. Chem. Rev.* **1999**, *188*, 35.

[59] Nayak, S. K.; Farrell, G. J.; Burkey, T. J. *Inorg. Chem.* **1994**, *33*, 2236–2242.

[60] Nayak, S. K.; Burkey, T. J. *Inorg. Chem.* **1992**, *31*, 1125.

[61] Trushin, S. A.; Fuss, W.; Kompa, K. L.; Schmid, W. E. *J. Phys. Chem. A* **2000**, *104*, 1997–2006.

[62] Dougherty, T. P.; Heilweil, E. J. *J. Chem. Phys.* **1994**, *100*, 4006.

[63] Poliakoff, M. *Chem. Phys. Lett.* **1981**, *78*, 1–3.

[64] Zhou, M. F.; Chertihin, G. V.; Andrews, L. *J. Chem. Phys.* **1998**, *109*, 10893–10904.

[65] Nayak, S. K.; Burkey, T. J. *J. Am. Chem. Soc.* **1993**, *115*, 6391–6397.

[66] Ziegler, T.; Tschinke, V.; Fan, L.; Becke, A. D. *J. Am. Chem. Soc.* **1989**, *111*, 9177–9185.

[67] Blomberg, M. R. A.; Siegbahn, P. E. M.; Svensson, M. *J. Am. Chem. Soc.* **1992**, *114*, 6095.

[68] Siegbahn, P. E. M.; Svensson, M. J. *J. Am. Chem. Soc.* **1994**, *116*, 10124.

[69] Carroll, J. J.; Weisshaar, J. C.; Haug, K. L.; Blomberg, M. R. A.; Siegbahn, P. E. M.; Svensson, M. *J. Phys. Chem.* **1995**, *99*, 13955.

[70] Ricca, A.; C.W., B. *Theor. Chim. Acta.* **1995**, *92*, 123.

[71] Glukhovtsev, M. N.; Bach, R. D.; Nagel, C. J. *J. Phys. Chem.* **1997**, *101*, 316.

[72] Lengsfield, B. H.; Jafri, J. A.; Phillips, D. H. *J. Chem. Phys.* **1981**, *74*, 6849–6856.

[73] Koseki, S.; Schmidt, M. W.; Gordon, M. S. *J. Phys. Chem. A* **1998**, *102*, 10430–

10435.

[74] Boys, S. F.; Bernardi, F. *Mol. Phys.* **1970**, *19*, 553.

[75] Liu, B.; McLean, A. D. *J. Chem. Phys.* **1973**, *59*, 4557.

[76] Lyne, P. D.; Mingos, D. M. P.; Ziegler, T.; Downs, A. J. *Inorg. Chem.* **1993**, *32*, 4785–4796.

[77] Barnes, L. A.; Rosi, M.; Bauschlicher, C. W. *J. CHem. Phys.* **1990**, *94*, 2031–2039.

[78] Drolet, D. P.; Lees, A. J. *J. Am. Chem. Soc.* **1992**, *114*, 4186.

[79] Chruch, S. P.; Grevels, F. –W.; Hermann, H.; Kelly, J. M.; Klotzbucher, W. E.; Schaffner, K. J. *J. Chem. Soc., Chem. Commun.* **1985**, 594.

[80] Krentz, R.; Pomeroy, R. K. *Inorg. Chem.* **1985**, *24*, 2976.

[81] Asbury, J. B.; Ghosh, H. N.; Yeston, J. S.; Bergman, R. G.; Lian, T. *Organometallics* **1998**, *17*, 3417.

[82] Scott, A. P.; Radom, L. *J. Phys. Chem.* **1996**, *100*, 16502.

[83] Beagley, B.; Schmidling, D. G. *J. Mol. Struct.* **1974**, *22*, 466.

[84] Beagley, B.; Parrott, C. T.; Ubrecht, G. G.; Young, J. *J. Mol. Struct.* **1979**, *52*, 47.

[85] Ladogana, S.; Nayak, S. K.; Smit, J. P.; Dobson, G. R. *Inorg. Chem.* **1997**, *36*, 650.

[86] Burkey, T. J. *J. Am. Chem. Soc.* **1990**, *112*, 8329.

[87] Lewis, J.; Nyholm, R. S.; Sandhu, S. S.; Stiddard, M. H. B. *J. Chem. Soc.* **1964**, 2825.

[88] Prausnitz, J. M.; Reid, R. C. *The Properties of Gases and Liquids*; 4 ed.;

McGraw–Hill: New York, 1987.

[89] Van Tentergem, M.; Van Der Kelen, G. P.; Claeys, E. C. *J. Mol. Struct.* **1982**, *80*, 317.

[90] Reckziel, A.; Bigorgne, M. *J. Organomet. Chem.* **1965**, *3*, 341.

[91] Steinfeld, J. I.; Francisco, J. S.; Hase, W. L. *Chemical Kinetics and Dynamics*; Prentice–Hall, Inc.: Englewood Cliffs, 1989.

[92] Cardaci, G. *Inorg. Chem.* **1974**, *13*, 368.

[93] Angermund, H.; Bandyopadhyay, A. K.; Grevels, F.–W.; Mark, F. *J. Am. Chem. Soc.* **1989**, *111*, 4656.

[94] Crabtree, R. H. *Chem. Rev.* **1985**, *85*, 245.

[95] *Activation and Functionalization of Alkanes*; Wiley: New York, 1989.

[96] Shilov, A. E.; Shul'pin, G. B. *Activation and Catalytic Reactions of Saturated Hydrocarbons in the Presence of Metal Complexes*; Kluwer: Boston, 2000.

[97] Stahl, S. S.; Labinger, J. A.; Bercaw, J. E. *Angew. Chem., Int. Ed. Eng.* **1998**, *37*, 2181.

[98] Shilov, A. E.; Shulpin, G. B. *Chem. Rev.* **1997**, *97*, 2879.

[99] Ghosh, C. K.; Graham, W. A. G. *J. Am. Chem. Soc.* **1987**, *109*, 4726.

[100] Bloyce, P. E.; Mascetti, J.; Rest, A. J. *J. Organomet. Chem.* **1993**, *444*, 223.

[101] Purwoko, A. A.; Lees, A. J. *Inorg. Chem.* **1995**, *34*, 424.

[102] Northcutt, T. O.; Wick, D. D.; Vetter, A. J; Jones, W. D. *J. Am. Chem. Soc.*, **2001**, *123*, 7257.

[103] Bennett, J. L.; Wolczanski, P. T. *J. Am. Chem. Soc.*, **1997**,*119*,10696.

[104] McNamara, B. K.; Yeston, J. S.; Bergman, R. G.; Moore, C. B. *J. Am. Chem.*

Soc. **1999**, *121*, 6437.

[105] Wick, D. D.; Reynolds, K. A.; Jones, W. D. *J. Am. Chem. Soc.* **1999**, *121*, 3974.

[106] Mobley, T. A.; Schade, C.; Bergman, R. G. *Organometallics* **1998**, *17*, 3574.

[107] Gross, C. L.; Girolami, G. S. *J. Am. Chem. Soc.* **1998**, *120*, 6605.

[108] Schafer, D. F.; Wolczanski, P. T. *J. Am. Chem. Soc.* **1998**, *120*, 4881.

[109] Jones, W. D.; Feher, F. J. *J. Am. Chem. Soc.* **1986**, *108*, 4814.

[110] Jones, W. D.; Feher, F. J. *J. Am. Chem. Soc.* **1982**, *104*, 4240.

[111] Jones, W. D.; Feher, F. J. *Acc. Chem. Res.* **1989**, *22*, 91.

[112] Parshall, G. W. *Acc. Chem. Res.* **1970**, *3*, 139.

[113] Muetterties, E. L.; Bleeke, J. R. *Acc. Chem. Res.* **1979**, *12*, 324.

[114] Nubel, P. O.; Brown, T. L. *J. Am. Chem. Soc.* **1984**, *106*, 644.

[115] Stoutland, P. O.; Bergman, R. G. *J. Am. Chem. Soc.* **1985**, 107, 4581.

[116] Zaric, S.; Hall, M. B. *J. Phys. Chem.* **1998**, *102*, 1963.

[117] Asplund, M. C. *In Time–Resolved Infrared Studies of C–H Activation by Organometallics*; University of California at Berkeley, 1998.

[118] Jones, W. D.; Feher, F. J. *Organometallics* **1983**, *2*, 562.

[119] Wenzel, T. T.; Bergman, R. G. *J. Am. Chem. Soc.* **1986**, *108*, 4856.

[120] Bell, T. W.; Haddleton, D. M.; McCamley, A.; Partridge, M. G.; Perutz, R. N.; Willner, H. *J. Am. Chem. Soc.* **1990**, *112*, 9212.

[121] Tellers D. M.; Yung C. M.; Arndtsen B. A.; Adamson D. R.; Bergman R. G. *J. Am. Chem. Soc.* 2002, *124*, 1400.

[122] Dallinger, R. F.; Woodruff, W. H. *J. Am. Chem. Soc.* **1979**, *101*, 4391.

[123] Bradley, P. G.; Kress, N.; Hornberger, B. A.; Dallinger, R. F.; Woodruff, W. H. *J. Am. Chem. Soc.* **1981**, *103*, 7441.

[124] Daul, C.; Baerends, E. J.; Vernooijs, P. *Inorg. Chem.* **1994**, *33*, 2528.

[125] Damrauer, N. H.; Cerullo, G. Yeh, A.; Boussie, T. R.; Shank, C. V.; McCusker, J. K. *Science*. **1997**, 275, 54.

[126] Yeh A. T.; Shank, C. V.; McCusker J. K. *Science*. **2000**, *289*, 935.

[127] Bhasikuttan, A. C.; Suzuki, M.; Nakashima, S.; Okada, T. *J. Am. Chem. Soc.* **2002**, ASAP Article.

[128] Heath, G. A.; Yellowlees, L. J.; Braterman, P. S. *J. Chem. Soc., Chem. Commun.* **1981**, 287.

[129] Moten, A. G.; Hanck, K.; DeArmond, M. K. *Chem. Phys. Lett.* **1991**, *79*, 541.

[130] Braterman, P. S.; Noble, B. C.; Peacock, R. D. *J. Phys. Chem.* **1986**, *90*, 4913.

[131] Noble, B.; Peacock, R. D. *Inorg. Chem.* **1996**, *35*, 1616.

[132] DeArmond, M. K.; Myrick, M. L. *Acc. Chem. Res.* **1989**, *22*, 364.

[133] Webb, M. A.; Knorr, F. J.; McHale, J. L. *J. Raman Spec.* **2001**, *32*, 481.

[134] Buchs, M.; Daul, C. *Chimia.* **1998**, *52*, 163.

[135] Jorgensen, W. L.; Briggs, J. M.; Contreras, M. L. *J. Phys. Chem.* **1990**, *94*, 1683.

[136] Bohm, H. J.; McDonald, I. R.; Madden, P. A. *Mol. Phys.* **1983**, *49*, 347.

[137] Ryckaert, J. P.; Ciccotti, G.; Berendsen, H. J. C. *J. Comput. Phys.* **1977**, *23*, 327.

[138] Del Bene, J. E.; Ditchfield, R.; Pople, J. A. *J. Chem. Phys.* **1971**, *55*, 2236.

[139] Foresman, J. B.; Head–Gordon, M.; Pople, J. A.; Frisch, M. J. *J. Phys. Chem.* **1992**, *96*, 135.

[140] Szabo, A.; Ostlund, N. S. *Modern Quantum Chemistry: Introduction To Advanced Electronic Structure Theory*; Dover, New York, 1998.

[141] Kollman, P. *Chem. Rev.* **1993**, *93*, 2395.

[142] Calzaferri, G.; Rytz, R. *J. Phys. Chem.* **1995**, *99*, 12141.

[143] Kober, E. M.; Meyer, T. J. *Inorg. Chem.* **1982**, *21*, 3967.

[144] Belser, P.; Daul, C.; Von Zelewsky, A. *Chem. Phys. Lett.* **1981**, *79*, 596.

[145] Felix, F.; Ferguson J.; Gudel, H. U.; Ludi, A. *Chem. Phys. Lett.* **1979**, *62*, 153.

[146] Ceulemans, A.; Vanquickenborne, L. G. *J. Am. Chem. Soc.* **1981**, *103*, 2238.

[147] Oh, D.; Boxer, S. G. *J. Am. Chem. Soc.* **1989**, *111*, 1130.

[148] Creutz, C.; Chou, M.; Netzel, T. L.; Okumura, M.; Sutin, N. *J. Am. Chem. Soc.* **1980**, *102*, 1309.

[149] Benko, G.; Kallioinen, J.; Korppi–Tommola, J. E. I.; Yartsev, A. P.; Sundstrom, V. *J. Am. Chem. Soc.* **2002**, *124*, 489.

[150] Heath, G. A.; Yellowlees, L. J.; Braterman, P. S. *Chem. Phys. Lett.* **1982**, *92*, 646.

[151] Yersin, H.; Braun, D. *Coord. Chem. Rev.* **1991**, *111*, 39.

[152] Passino, S. A.; Nagasawa, Y.; Fleming, G. R. *J. Chem. Phys.* **1997**, *107*, 6094.

[153] Kober, E. M.; Sullivan, B. P.; Meyer, T. J. *Inorg. Chem.* **1984**, *23*, 2098.

[154] Sherrill C.D.; Lee M.S.; Head–Gordon M. *Chem. Phys. Lett.* **1999**, *302*, 425.

[155] Kraus, C. A. *J. Am. Chem. Soc.* **1908**, *30*, 1323.

[156] Mingus, A.; Gauduel, Y.; Martin, J. L.; Antonetti, A. *Phys. Rev. Lett.* **1987**, *58*, 1559.

[157] Silva, C.; Walhout, P. K.; Yokoyama, K.; Barbara, P. F. *Phys. Rev. Lett.* **1998**, *80*, 1086.

[158] Kloepfer J. A.; Vilchiz, V. H.; Lenchenkov, V. A.; Bradforth, S.E. *Chem Phys. Lett.* **1998,** *298*, 120.

[159] de Boeij, W. P.; Pshenichnikov, M. S.; Wiersma, D. A. *Ann. Rev. Phys. Chem.* **1998**, *49*, 99.

[160] Martini I. B.; Barthel, E. R.; Schwartz B. J. *Science*, **2001**, *293*, 462.

[161] Tauber, M.; Mathies, R. A. *J. Phys. Chem. A.* **2001**, *105*, 10952.

[162] Fueki, K.; Feng, D.–F.; Kevan, L. *J. Phys. Chem.* **1970**, *74*, 1976.

[163] Jonah, C. D.; Romero, C.; Rahman, A. *Chem. Phys. Lett.* **1986**, *123*, 209.

[164] Schnitker, J.; Motakabbir, K.; Rossky, P. J.; Friesner, R. *Phys. Rev. Lett.* **1988**, *60*, 456.

[165] Rossky, P. J.; Schnitker, J. *J. Phys. Chem.* **1988**, *92*, 4277.

[166] Us. *J. Am. Chem. Soc.* **2002**, .

[167] Bezel, I.; Gaffney, K. J.; Garrett–Roe, S.; Harris, C. B.; Liu, S. H.; Miller, A. D.; Szymanski, P. *Science*. **2002**, In press.

[168] Gahl, C.; Bovensiepen, U.; Frischkorn, C.; Wolf, M. *Phys. Rev. Lett.*, **2002**, in publication.

[169] Zhu, J. J.; Cukier, R. I. *J. Chem. Phys.* **1993**, *98*, 5679.

[170] Feit, M. D.; Fleck, J. A.; Steiger, A. *J. Comp. Phys.* **1982**, *47*, 412.

[171] Feit, M. D.; Fleck, J. A .*J. Chem. Phys.* **1983**, *78*, 301.

[172] Feit, M. D.; Fleck, J. A .*J. Chem. Phys.* **1984**, *78*, 2578.

[173] Turi, L.; Mosyak, A.; Rossky, P. J. *J. Chem. Phys.* **1997**, *107*, 1970.

[174] Turi, L.; Minary, P.; Rossky, P. J. *Chem. Phys. Lett.* **2000**, *316*, 465.

[175] Feynman, R. P. *Phys. Rev.* **1939**, *81*, 385.

[176] Hellman, H. in *Einfuhrung in die Quantunchemie*. Franz Deuticke, Leipzig, 1937.

[177] Ewald, P. *Ann. Phys.* **1921,** *64*, 253.

[178] Foster, K. Raghavan, K. Berkowitz, M. *Chem. Phys. Lett.* **1989**, *162*, 32.

[179] Raghavan, K.; Foster, K.; Berkowitz, M. *Chem. Phys. Lett.* **1991**, *177*, 426.

[180] Haughney, M.; Ferrario, M.; McDonald, I. R. *J. Phys. Chem.* **1987**, *91*, 4934.

[181] Ryckaert, J. P; Ciccotti, J. P; Berendsen, H. J. C. *J. Comput. Phys.* **1977**, *23*, 327.

[182] Sindzingre, P.; Klein, M. L. *J. Chem. Phys.* **1992**, *96*, 4681.

[183] Yeh, I.–C.; Berkowitz, M. L. *J. Chem. Phys.* **1999**, *111*, 3155.

[184] Shelley, J. C.; Patey, G. N. *Mol. Phys.* **1996**, *88*, 385.

[185] Alejandre, J.; Tildesley, D. J.; Chapela, G. A. *J. Chem. Phys.* **1995**, *102*, 4574.

[186] Shelley, J. C.; Patey, G. N.; Berard, D. R.; Torrie, G. M. *J. Chem. Phys.* **1997**, *107*, 2122.

[187] Kevan, L. *Chem. Phys. Lett.* **1979**, *66*, 578.

[188] Kevan, L. *Acc. Chem. Res.* **1981**, *14*, 138.

[189] Chase, W. J.; Hunt, J. W. *J. Phys. Chem.* **1975**, *79*, 2835.

[190] Kevan, L. *J. Chem. Phys.* **1972**, *56*, 838.

[191] Richards, J. T.; Thomas, J. K. *J. Chem. Phys.* **1970**, *53*, 218.

[192] Higashimura, T.; Noda, M.; Warashina, T.; Yoshida, H. *J. Chem. Phys.* **1970**, *53*, 1152.

[193] Hase, H.; Noda, M.; Higashimura, T. *J. Chem. Phys.* **1971**, *54*, 2975.

[194] Hirata, Y.; Mataga, N. *J. Phys. Chem.* **1991**, *95*, 9067.

[195] Fueki, K.; Feng, D.–F.; Kevan, L.; Christoffersen, R. E. *J. Phys. Chem.* **1971**, *75*, 2297.

[196] Pepin, C.; Goulet, T.; Houde, D.; Jay–Gerin, J.–P. *J. Phys. Chem.* **1994**, *98*, 7009.

[197] Pepin, C.; Goulet, T.; Houde, D.; Jay–Gerin, J.–P. *J. Chim. Phys.* **1996**, *93*, 182.

[198] Baxendale, J. H.; Wardman, P. *J. Chem. Soc., Faraday I.*, **1973**, *69*, 584.

[199] Ladogana, S.; Nayak, S. K.; Smit, J. P.; Dobson, G. R. *Organometallics* **1997**, *16*, 3051.

[200] Ladogana, S.; Nayak, S. K.; Smit, J. P.; Dobson, G. R. *Inorg. Chem.* **1997**, *36*, 650.

[201] Creaven, B. S.; George, M. W.; Ginzburg, A. G.; Huges, C.; Kelly, J. M.; Long, C.; McGrath, I. M.; Pryce, M. T. *Organometallics.* **1993**, *12*, 3127.

[202] Breheny, C. J.; Kelly, J. M.; Long, C.; O'Keeffe, S.; Pryce, M. T.; Russell, G.; Walsh, M. M. *Organometallics.* **1998**, *17*, 3690.

[203] Lugovskoy, A.; Paur–Afshari, R.; Schultz, R. H. *J. Phys. Chem. A.* **2000**, *104*, 10587.

[204] Krishnan, R.; Schultz, R. H. *Organometallics.* **2001**, *20*, 3314.

[205] Asplund, M. C.; Snee, P. T.; Yeston, J. S.; Wilkens, M. J.; Payne, C. K.; Yang, H.; Kotz, K. T.; Frei, H.; Bergman, R. G.; Harris, C. B. *J. Am. Chem. Soc.* **2002**, *124*, 10605.

[206] Yang, H. Unpublished data.

[207] Dellago, C.; Bolhuis, P.; Chandler, D. *J. Chem Phys.* **1998**, *108*, 9236.

[208] Dellago, C.; Bolhuis, P.; Csajka, F.; Chandler, D. J. *Chem. Phys.* **1998**, *108*, 1964.

[209] Dellago, C.; Bolhuis, P.; Chandler, D. *J. Chem. Phys.* **1999**, *110*, 6617.

[210] Geissler, P.L. and D. Chandler, *J. Chem. Phys.* **2000**, *113*, 9759.

[211] Bolhuis, P.; Dellago, C.; Chandler, D.; Geissler, P. *Ann. Rev. of Phys. Chem.* **2002**, *59*, 291.

[212] Dellago, C.; Bolhuis, P.; Geissler, P. *Advances in Chemical Physics,* Wiley, 2002.

Appendix.

Section A.1 Radial Distribution Functions for systems with slab periodicity.

In the course of our work on solvated electrons in bulk and at surface interfaces, it became apparent that a method was needed to calculate the pair probability function on an equal basis in all systems. Standard methods may be applied to the bulk calculations, however the problem of evaluating normalized pair potential in quasi–three dimensional systems is not straightforward. The difficulty arises due the need to normalize the number of observed sites within a given spatial element with the average number density of the system. For example, in three dimensions one would average number of sites that exist within a given volume element dV and then normalize by $\rho \cdot dV$, where ρ is the average number density N/V. In two dimensional system calculations one would normalize over a finite area dA. In quasi–three dimensional systems such as a thick slab, nearby sites should be normalized by a scheme based on a finite volume elemental correction, while at long distances the normalization should become more 2D like. We have developed an algorithm that is able to bridge the two extremes and is discussed in detail below.

Our method is an 'on the fly' normalization scheme that is able to account for the local "bulk–like" environment at close distances and the more two–dimensional structure of an extended layer at larger distances. For an example, will illustrate how to calculate the pair potential between a single excess Cl^- atom immersed in an extended layer of methanol. Extension to the excess electron or to neat systems is straightforward. In our

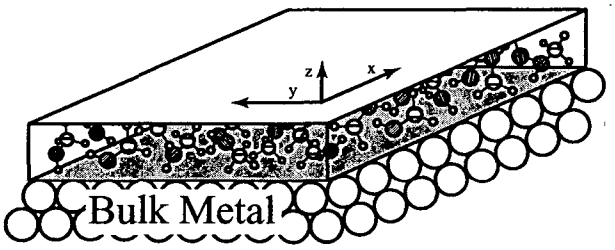

Figure A.1: A system with slab geometry. The coordinate system is periodic in x and y as in the example provided.

example, the x and y will represent the periodically replicated dimensions, while the z direction is finite as presented graphically in Figure A.1. The 'on the fly' normalization scheme is necessary due to the z dependence on the normalization factor. The algorithm is described in step–by–step form below.

Step 1: First, define the following variables. In this example the system is composed of a single Cl^- atom, N_{mol} number of methanol molecules and thus N_{mol} number of H, O, and CH_3 sites. We wish to calculate the radial distribution function over a discrete radial element *dr*, which for example may represent 1% of the x– or y– directional box length. The array Gofr[N_{gofr}], where N_{gofr} is defined as R_c/dr, will be used to store the data as it is calculated. The variable R_c is a long distance radial cutoff, typically half the extended x or y directional length.

Step 2: Since we will start with the H sites in our example, first define the highest and lowest z– position over all of the N_{mol} methanol H sites for a given configuration and store the results into memory. Next, define an 'instantaneous number density' D_H =

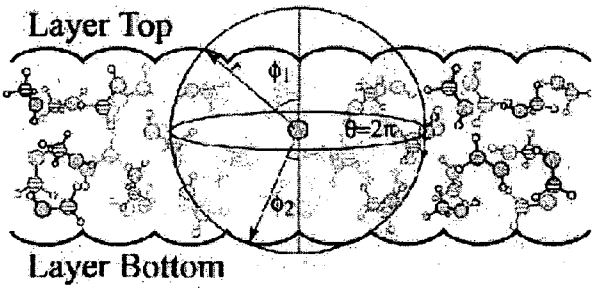

Figure A.2 An example of how to select angles ϕ.

N_{mol}/V, where V is the volume defined by the x and y box lengths and the thickness of the layer as calculated above.

Step 3: The $Cl^- \rightarrow H$ pair probability will be calculated first with the Cl^- atom defined to exist at the origin. Loop over all H sites in the system. Once a H site has been chosen, evaluate the $Cl^- \rightarrow H$ distance via $R_{Cl\rightarrow H} = \sqrt{x^2+y^2+z^2}$. Calculate an integer called Binnumb, which is defined as $N_{gofr} \cdot R_{Cl\rightarrow H} / R_c$.

Step 4: Calculate the z distance of the Cl^- atom to the bottom and top of the H site layer, variables which were saved in the first step.

Step 5: *If* the radial distance $R_{Cl\rightarrow H}$ between the Cl^- and tagged H is shorter than either the two distances determined in the previous step, then calculate a normalizing variable as Norm = $(4/3 \cdot \pi \cdot [R_{Cl\rightarrow H}^3 - (R_{Cl\rightarrow H} - dr)^3] \cdot D_H$. To the present value of Gofr at array element Binnumb, add the value 1.0/Norm. This case represents spherical

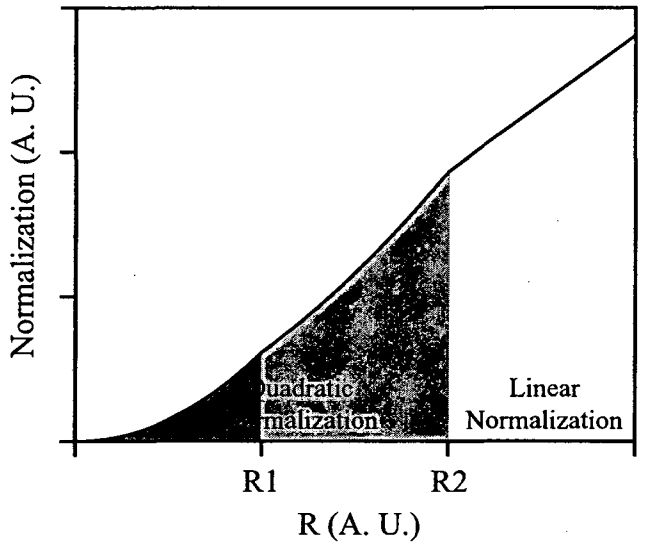

Figure A.3 An example of a normalization curve using the method provided in the text. The distances R1 and R2 represent distances from the tagged site to either the top or the bottom of the layer. After these distances, the normalizing curve is linear.

normalization.

Or if the radial distance between the Cl^- and tagged H is longer than either the two distances calculated in **Step 4**, then a different approach is necessary. First, define an angle ϕ that has a value in the +z direction of 0 and a value of π in the –z direction. Calculate the value of ϕ that exists that describes a vector of length $R_{Cl \rightarrow H}$, the origin of which is at the Cl^- site that touches the top boundary layer of the H sites from **Step 1**. Call this variable ϕ_1. In a similar manner, calculate a value called ϕ_2 that describes a vector that has the Cl^- site at the origin and touches the bottom of the H layer. This process is illustrated in Figure A.2.

The radial volume element will now be calculated via partial integration of a

sphere over a range $r = 0 \rightarrow R_{Cl\rightarrow H}$ $\theta = 0 \rightarrow 2\pi$, $\phi = \phi_1 \rightarrow \phi_2$. Thus, the Norm variable has the value:

$$\text{Norm} = 2/3 \cdot \pi \cdot [R_{Cl\rightarrow H}^3 - (R_{Cl\rightarrow H} - dr)^3] \cdot [\cos(\phi_1) - \cos(\phi_2)] \cdot D_H.$$ To the present value of the array Gofr at element binnumb, add the value 1.0/Norm.

Step 6: Loop over remaining sites, always adding the elements of Gofr to the previous value.

As can be shown in Fig. A.3, the normalization at close distances appears parabolic yet a cross over to a linear regime once a critical distance has been reached. This method is general and may be applied to multiple systems. The method may also be used to calculate pair distribution functions between molecules in different layers with the appropriate choice of ϕ angles and instantaneous number density. Unfortunately, the average number of molecules within a given shell may not be calculated from the distribution function due to the 'on–the–fly' normalization scheme. In these cases, a trajectory needs to be recalculated with an additional function to determine the number of molecules that appear within a radial distance defined from the first simulation.

Section A.2 A closed loop high pressure flow cell.

In order to understand how solvent properties affect a reaction mechanism, we have constructed a high pressure observation cell. The purpose of this cell is to adjust the solvent parameters without changing the basic molecular nature of the fluid. Consequently, this system will allow us to critically examine how the viscosity of a fluid alters the chemical dynamics of a reactive system. Unfortunately, this system was built

during the construction of our ultrafast laser spectrometer, which has not been completed at the time of this writing. Thus, the pressure system has not been used for its original purpose as certain parameters of the system depend on the final design of the spectrometer. However, the construction details and a description of how the system works are provided for the future.

The study of critical fluids in an ultrafast experiment places certain limitations on a high pressure system. First, the examination of a reactive system means that the liquid must flow so that a fresh sample is interrogated by the laser at each pulse. Second, the concentration of analyte may not vary over the course of the experiment. As a result, the fluid must flow in a close loop. This requirement creates a serious difficulty in that pressure pumps require a gradient across the valves in order to reciprocate properly. Thus, the flow pump will not function in a simple closed loop. These issues have been addressed with the use of a back pressure regulator (BPR), and our design has been shown to allow a pressurized fluid to flow in a closed system.

Shown in Figure A.4 are the observation cell and pumping components. The system is loaded by first opening the inlet valve and closing the cell valve (these valves should never be open simultaneously). The liquid or gas to be studied is first drawn into the pressure pump by turning the crank until it has reached its maximum length. The inlet valve is then closed, the cell valve is opened, and the pressure pump injects the gas or fluid into the rest of the system. The pressure equalization valve should be open at this time. This is repeated until the system has reached the set point of the back pressure regulator, after which the equalization valve should be closed. Next, the back pressure regulator set point should be increased by at least ~1 atm and the system should be pressurized only to that extent. This assures that a pressure gradient now exists at the

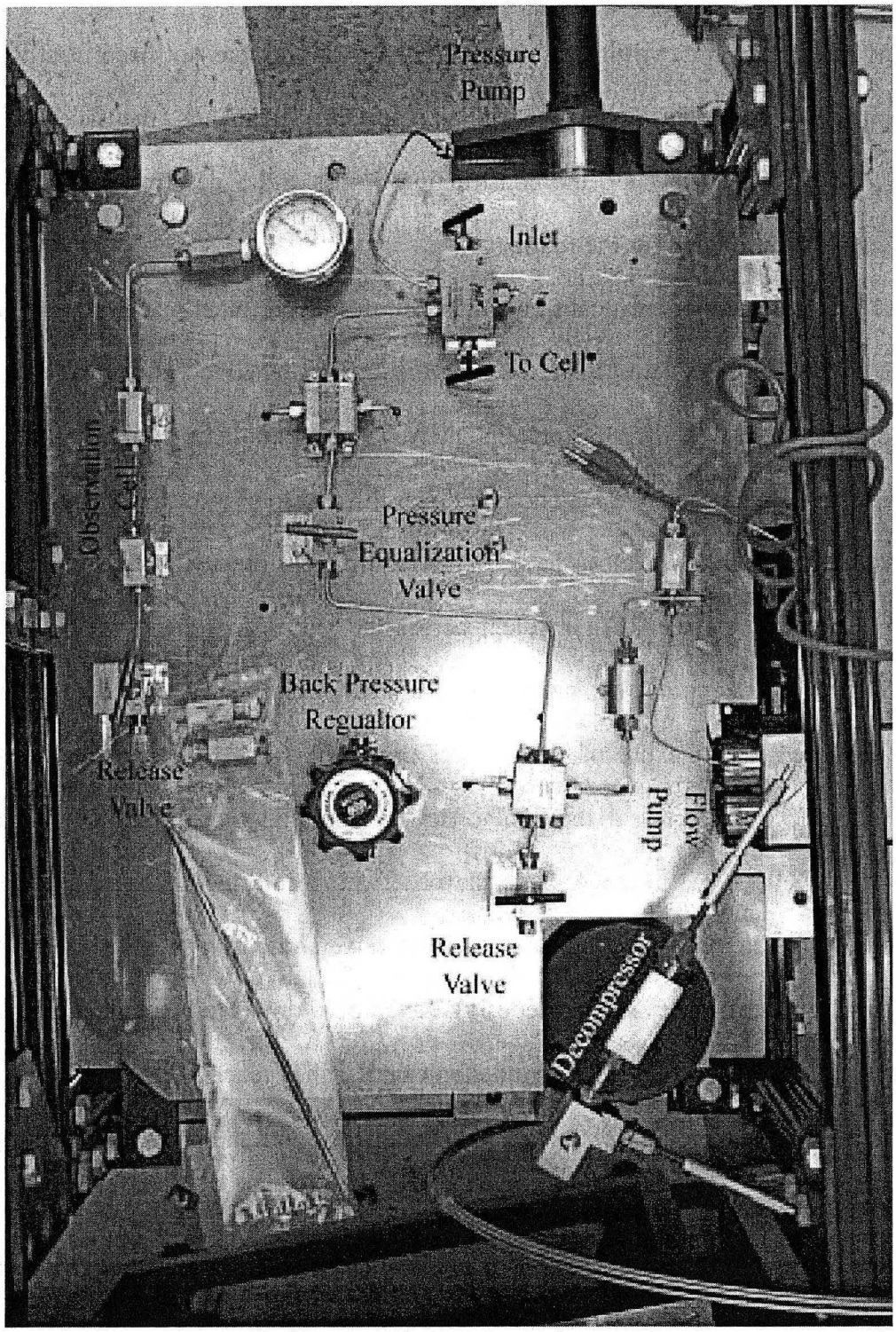

Figure A.4. The high pressure observation cell manifold.

flow pump. Note that if the system is pressurized well over the new BPR setting, the BPR valve will simply remain open and the flow pump will not function.

This design allows high pressure fluids to flow by the following mechanism. Now that the connection after the BPR to the flow pump inlet (low pressure region) is at a lower pressure than the pump outlet to the front of the BPR (high pressure region), the pressure pump will be able to reciprocate properly. When fluid is drawn from the pump inlet and moved into the outlet, the high pressure side is now at a higher pressure. When this higher pressure is greater than the setpoint of the BPR, that valve opens and fluid mass moves from the high pressure to the low pressure region. The valve will close after the pressure at the front of the BPR reaches the setpoint, which assures that the pressure gradient is maintained. This process will continue for the course of the experiment. Our tests using pressurized liquid water were successful in this endeavor.

In order to study liquified gases, an inlet manifold is needed and is described in detail here. The manifold is shown in Figure A.5. The first step is to degas the entire system by closing the inlet valve and opening the vacuum, high pressure pump, and vacuum pressure gauge valves. Once the system has been evacuated, a gas cylinder should be connected to the inlet valve. This has not been completed because every gas will have to use a different connection, so the inlet will have to be tailored to the study. Next, close the vacuum, pressure pump and vacuum gauge valves and open the inlet valve. The system should be able to handle the direct opening to the main cylinder, however a 2500 psi rupture valve has been added. If there are no leaks or other problems, the high pressure pump valve may be opened and the system should be pressurized as described above.

As the spectrometer has not been completed at this time, the observation cell has

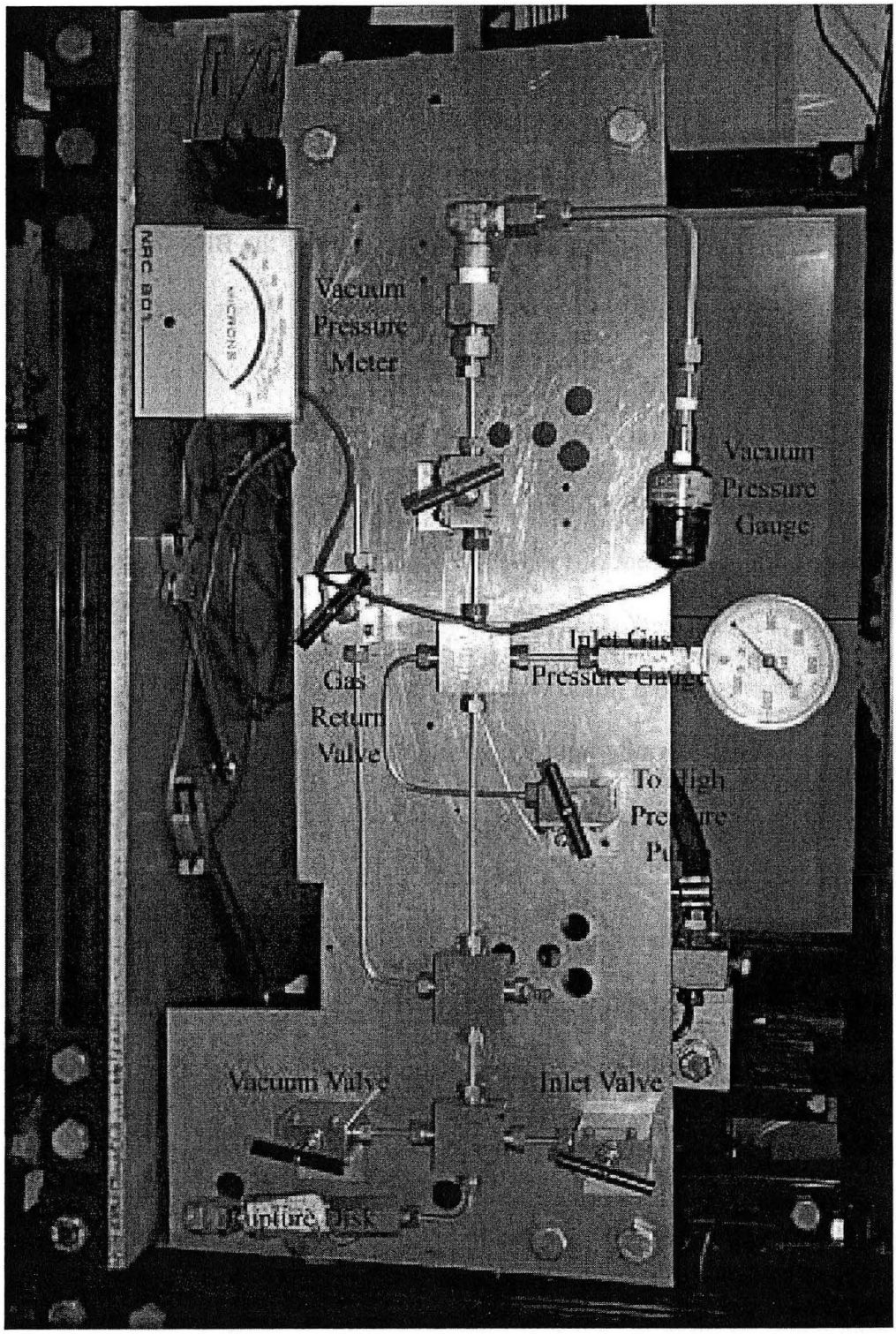

Figure A.5. The gas inlet manifold for supercritical gas solvent studies.

not been added to the system. This can be done by breaking the line marked observation cell in Figure A.4, from which tubing can be added to the location on the laser table where the observation cell should sit and back. Also, the venting lines have not been added as gas venting will have to be treated on a case by case basis. Non–flammable gases may be vented directly into a hood while flammable gases will take more care. Further, it is unlikely that the decompressor is needed. The system may be evacuated directly back into the original gas tank as the pressurizing pump can apply more pressure than exists in most gas cylinders.

Section A.3 The split operator method.

The following is a program to propagate a 1–D wavefunction along a potential energy surface as discussed in Chapter 8. The program can also calculate overlap correlation functions and eigenvectors of the Hamiltonian.

```
#include <stdio.h>
#include <math.h>
#include <stdlib.h>

float wf_real[256];          /* This is the wavefunction itself                    */
float wf_imag[256];          /* It is divided into real and imaginary components */

void fft(short);
void main(void);

void main(void)
{
    int i,x,m,m3,L=256,t,tott=10000;     /* t tot=total simulation time.              *
                                          * L is the number of points of the potential *
                                          *  and w.f., must be 2^Y for fft to work    *
                                          * Adjust L and the fft variable m must be   *
                                          * changes as well                           */

    int eigencal=0;              /* Flag to calculate the eigenfunction defined by the *
                                  * eigenvalue in freq                                 */
    int corrp=1;                 /* Flag to calculate the overlap trajectory in order to
                                  *  calculate eigenenergies                           */
    int wfprint=0;               /* Flag to print the w.f. trajectory                  */

    float wf_real_initial[256], wf_imag_initial[256];
```

```
                                /* Stores the initial w.f. in order to calculate the overlap    *
                                 * trajectory                                                  */

float eigen[256][2];            /* The eigenfuction, if eigencal=1                             */

float mass=1822.88, k=0.04, sigma=0.14, dt=1.5;
                                /* atomic units, mass=mass of the electron, energy in          */
                                 *  Hartrees, time is 2.4e-17sec                               */

float V[256][2],K[256][2];      /* The split operators                                         */

float pi, freq;
float renorm,vcor_r,vcor_i,vcor,length;
float dx,x2,m2,potential;


pi=4.0*atan(1);
dx=0.04;                        /* Length is in units of Bohrs                                 */
length=L*dx;                    /* The total length of my 1-D vector in Bohrs                  */

                        /* INITIALIZE THE WF */
for (x=0; x<L; x++){
   eigen[x][0]=0.0;
   eigen[x][1]=0.0;

   x2=x*dx-length/2.0;
   wf_real[x]=exp(-(x2+0.3)*(x2+0.3)/(2.0*sigma*sigma));
                        /* The wf is off set from the center of the potential                  */
   wf_imag[x]=0.0;
                        /* This initialization is totally arbitrary                            */

   potential=0.5*k*x2*x2;       /* Define the potential surface here                           */
   V[x][0]=cos(dt*potential);
   V[x][1]=sin(dt*potential);

   m3=x;
   if (x>L/2) m3=L-x;           /* this takes into account the odd indexing of the fft */
   m2=m3*2.0*pi/length;         /* the unit increment in fft space                             */
   K[x][0]=cos(dt/4.0/mass*m2*m2);
   K[x][1]=sin(dt/4.0/mass*m2*m2);
   }
                        /* The WF MUST be NORMALIZED */

renorm=0.0;
for (x=0; x<L; x++){
    renorm=renorm+wf_real[x]*wf_real[x]+wf_imag[x]*wf_imag[x];
    }
renorm=sqrt(renorm);

for (x=0; x<L; x++){
    wf_real[x]=wf_real[x]/(renorm);
    wf_imag[x]=wf_imag[x]/(renorm);

    wf_real_initial[x]=wf_real[x];
    wf_imag_initial[x]=wf_imag[x];
    if (wfprint==1) printf("%f %f\n",wf_real[x],wf_imag[x]);
```

```
        }

                        /* The initial w.f. must be saved to calc correlation functions
                         * later.                                                    */

for (t=0; t<tott; t++){

                        /* FOURIER TRANSFORM TO P */
    fft(1);

                        /* Calc Free Particle Operators */

    for (m=0; m<L; m++){

      wf_real[m]=wf_real[m]*K[m][0]+wf_imag[m]*K[m][1];
      wf_imag[m]=wf_imag[m]*K[m][0]-wf_real[m]*K[m][1];
      }

                        /* TRANSFORM BACK */
   fft(0);

                        /* NOW E^-iV ACTS UPON THE WF  */
    for (x=0; x<L; x++){
      wf_real[x]=wf_real[x]*V[x][0]+wf_imag[x]*V[x][1];
      wf_imag[x]=wf_imag[x]*V[x][0]-wf_real[x]*V[x][1];
      }
                        /* TRANSFORM TO P SPACE AGAIN */

   fft(1);

                        /* Calc Free Particle Operators */
    for (m=0; m<L; m++){
      wf_real[m]=wf_real[m]*K[m][0]+wf_imag[m]*K[m][1];
      wf_imag[m]=wf_imag[m]*K[m][0]-wf_real[m]*K[m][1];
      }

                        /* TRANSFORM BACK */

   fft(0);

                        /* RENORMALIZE */
   renorm=0.0;
   for (x=0; x<L; x++){
      renorm=renorm+wf_real[x]*wf_real[x]+wf_imag[x]*wf_imag[x];
      }
   renorm=sqrt(renorm);

   for (x=0; x<L; x++){
      wf_real[x]=wf_real[x]/(renorm);
      wf_imag[x]=wf_imag[x]/(renorm);
      }

   if(wfprint==1)
      for (x=0; x<L; x++){
         printf("%f %f\n",wf_real[x],wf_imag[x]);
         }
```

```
                    /* Calc the overlap                                    *
                     * Ultimately use this to calc eigenvals and then      *
                     *  eigenfunctions                                     */
    if(corrp==1){
        vcor_r=0.0;
        vcor_i=0.0;
        for (x=0; x<L; x++){
            vcor_r=vcor_r+wf_real_initial[x]*wf_real[x]+wf_imag_initial[x]*wf_imag[x];
            vcor_i=vcor_i+wf_real_initial[x]*wf_imag[x]-wf_imag_initial[x]*wf_real[x];
          }
        vcor=vcor_r*vcor_r+vcor_i*vcor_i;
        printf("%f %f %f\n",vcor_r,vcor_i,sqrt(vcor_r*vcor_r+vcor_i*vcor_i));
        }

                    /* The next part calculates eigenfunctions */
    if(eigencal==1)
        for (x=0; x<L; x++){
            eigen[x][0]=eigen[x][0]+(cos(t*dt*freq)*wf_real[x]-
                        sin(t*dt*freq)*wf_imag[x]);
            eigen[x][1]=eigen[x][1]+(cos(t*dt*freq)*wf_imag[x]+
                        sin(t*dt*freq)*wf_real[x]);
            }

    }                   /* End of Time loop                                */

  if(eigencal==1) for (x=0; x<L; x++)
      printf("%f %f\n",eigen[x][0],eigen[x][1]);
  }


void fft(short dir){

  long m,n,i,i1,j,k,i2,l,l1,l2;
  double c1,c2,tx,ty,t1,t2,u1,u2,z;

  m=8;
  /* Calculate the number of points */
  n = 1;
  for (i=0;i<m;i++)
    n *= 2;

  /* Do the bit reversal */
  i2 = n >> 1;
  j = 0;
  for (i=0;i<n-1;i++) {
    if (i < j) {
      tx = wf_real[i];
      ty = wf_imag[i];
      wf_real[i] = wf_real[j];
      wf_imag[i] = wf_imag[j];
      wf_real[j] = tx;
      wf_imag[j] = ty;
    }
    k = i2;
    while (k <= j) {
```

```
      j -= k;
      k >>= 1;
    }
    j += k;
  }

  /* Compute the FFT */
  c1 = -1.0;
  c2 = 0.0;
  l2 = 1;
  for (l=0;l<m;l++) {
    l1 = l2;
    l2 <<= 1;
    u1 = 1.0;
    u2 = 0.0;
    for (j=0;j<l1;j++) {
      for (i=j;i<n;i+=l2) {
        i1 = i + l1;
        t1 = u1 * wf_real[i1] - u2 * wf_imag[i1];
        t2 = u1 * wf_imag[i1] + u2 * wf_real[i1];
        wf_real[i1] = wf_real[i] - t1;
        wf_imag[i1] = wf_imag[i] - t2;
        wf_real[i] += t1;
        wf_imag[i] += t2;
      }
      z =  u1 * c1 - u2 * c2;
      u2 = u1 * c2 + u2 * c1;
      u1 = z;
    }
    c2 = sqrt((1.0 - c1) / 2.0);
    if (dir == 1)
      c2 = -c2;
    c1 = sqrt((1.0 + c1) / 2.0);
  }

  /* Scaling for forward transform */
  if (dir == 1) {
    for (i=0;i<n;i++) {
      wf_real[i] /= n;
      wf_imag[i] /= n;
    }
  }
}
```

Ernest Orlando Lawrence Berkeley National Laboratory
One Cyclotron Road | Berkeley, California 94720

Prepared for the U.S. Department of Energy under Contract No. DE-AC03-76SF00098